Optimization of Lead Halide Perovskite Thin Films by Chemical Vapour Deposition

Stephen Charles Klue

A thesis submitted in fulfilment of the requirement
for the degree of Master of Science in the Department of
Physics and Astronomy, University of the Western Cape (UWC).

Supervisor: Prof. C. J. Arendse (UWC)
Co-supervisor: Dr. Chris Mtshali (iThemba LABS)

August 5, 2021

UNIVERSITY *of the*
WESTERN CAPE

Acknowledgements

Declaration

I declare that, "Optimization of Lead Halide Perovskite Thin Films by Chemical Vapour Deposition" is my own work, that it has not been submitted for any degree or examination in any other university, and that all the sources used or quoted have been indicated and acknowledged with complete references. All images have also been created for this thesis except where referenced.

Full name: *Stephen Charles Klue*   Date: 5 Aug 2021

Signed:

Abstract

Perovskite solar cells have gained tremendous attention within the past decade, due to its rapid improvement in power conversion efficiency (PCE), with the current record cell at 25%. The aim of this study is to create a repeatable and scalable chemical vapour deposition technique that can be used to construct perovskite solar cells with a high PCE while maintaining long-term stability. The technique requires the formation of a uniform and compact lead halide layer, either PbI_2 or $PbCl_2$ that is sequentially converted into the perovskite structure with the exposure of Methylammonium iodide (MAI) vapour. The use of CVD with a 5 cm diameter quartz tube was successfully used to deposit uniform thin films of both PbI2 and $PbCl_2$ over an area of 6 cm^2 with a thickness deviation of 5%. Thickness control was obtained by varying the amount of source material which allows for repeatable control within 5% error, without the need for a crystal thickness monitor. Both lead halides can sequentially be converted to perovskite with a maximum conversion area of 40 cm^2, limited by the tube diameter and furnace dimensions. The lower uniformity of the lead halide CVD deposition is due to most of the vapour concentrating along the centre of the tube, resulting in a decrease of thickness towards the tube walls. The most important parameter during the conversion of perovskite was determined to be the substrate temperature which controls the rate of MAI diffusion into the lead halide structure. Temperature below 120°C quickly lead to over saturations and higher temperature prevent the formation of perovskite. The perovskite solar cells produced a maximum PCE of 9.2%, however there was a large deviation in performance with samples with the same architecture providing an average PCE of $6 \pm 2\%$. The cells also exhibit large hysteresis and were unable to maintain a steady PCE under a constant load with a significant decrease in current density. One of the major concerns is the high relative humidity in the labs in excess of 75% which not only affected the stability of the perovskite, but also the Spiro-Ometad hole transporting layer.

Contents

General Abbreviations

CCD Charge-Coupled Device

CV Coefficient of Variation

CVD Chemical Vapour Deposition

ETL Electron Transport Layer

HJ-IBC heterojunction interdigitated back contact

HTL Hole Transport Layer

PERC passivated emitter rear cell

PVD Physical Vapour Deposition

RBS Rutherford backscatter spectrometry

SNR Signal-to-Noise Ratio
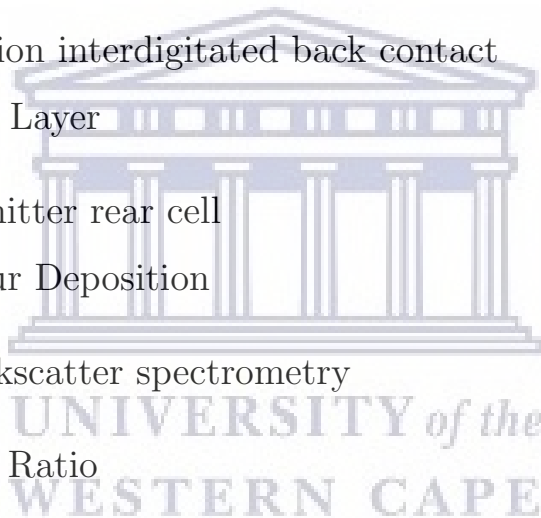
Abbreviations of Materials

2ME 2-Methoxyethanol

a-Si amorphous silicon

ACN Acetonenitrile

c-Si crystalline silicon

c-TiO$_2$ Compact Titanium dioxide

CB Chlorobenzene

CdTe cadmium telluride

CIGS copper indium gallium selenide

CoTFSI tris(2-(1H-pyrazol-1-yl)-4-tert-butylpyridine)cobalt(III) tri[bis(trifluoromethane)sulfonimide]

DM N2,N2',N7,N7'-tetrakis(9,9-dimethyl-9H-fluoren-2-yl)-N2,N 2',N 7,N 7' -tetrakis(4-methoxyphenyl)-9,9' - spirobi[fluorene]-2,2', 7'7'-tetraamine

DMF N,N-Dimethylformamide

DMSO Dimethyl sulfoxide

GBL γ-Butyrolactone

IBN Isobutyronitrile

IPA Isopropyl alcohol or 2-Propanol

LiTFSI Bis(trifluoromethane)sulfonimide lithium salt

m-LBSO Mesoporous Lanthanum doped Barium Stannate (BaSnO$_3$)

m-TiO$_2$ Mesoporous Titanium dioxide

MA Methylammonium

MDA Methylenediammonium

PEAI Phenethylammonium Iodide (C$_8$H$_{12}$IN)

PEI Polyethylenimine

PTAA Poly(triaryl amine)

PTC Particle

Spiro-OMeTAD 2,2',7,7'-Tetrakis[N,N-di(4-methoxyphenyl)amino]-9,9'-spirobifluorene

tBP 4-tert-Butylpyridine

TiIA Titanium diisopropoxide bis(acetylacetonate)

List of Symbols

D_g Diffusion Constant

EQE External Quantum Efficiency

FF Fill Factor

J Current Density

J_0 Saturation Current

J_{ph} Photocurrent

R_s Series Resistance

R_{sh} Shunt Resistance

V_T Thermal Voltage

k_B Boltzmann Constant ($1.380649 \times 10\text{-}23$ J.K^{-1})

n Ideality Factor

q Elementary Charge ($1.602176634 \times 10^{19}$ C)

α Absorption Coefficient

λ Wavelength

E_g Energy Gap or Bandgap

c Speed of light (2.99792458×10^8 m/s)

h Planck Constant ($4.135667696 \times 10^{-15}$ eV.s)

ν Frequency (Hz)

List of Figures

List of Tables

Chapter 1

Introduction

For centuries most countries have relied predominately on fossil fuels to meet their ever-growing energy demands which lead to the imminent threat of climate change. Climate change is a disruption of the energy equilibrium of the earth, resulting in catastrophic weather events and rising sea levels.[4]. Nearly all nations have pledged to reduce their CO_2 emissions and increase the adoption of renewable energy as part of the Paris agreement, signed in 2016. One of the most readily available renewable energy sources is solar energy, which is predominately harvested by utilizing crystalline silicon solar cells. In this study the use of an alternative absorber material will be investigated, $MAPbI_3$ Methylammonium Lead Iodide, which has the perovskite crystal structure.

The aim of all solar cells is to harness as much energy from the sun, which at its maximum can provide 1 kW of power per square meter on the earth's surface. The available energy of the sun as a function of wavelength can be seen in fig. 1.1, where the power is integrated from the shorter wavelengths (higher energy) to the longer wavelengths.

The aim of this study is to investigate the role that the perovskite material has in the future of solar cell technology using a scalable CVD technique. The power conversion efficiency will be primarily evaluated, which is the fraction of usable energy that can by extracted from the sun. The other factors that influence the commercialization of the perovskite material is cost, long-term stability and environmental impact.
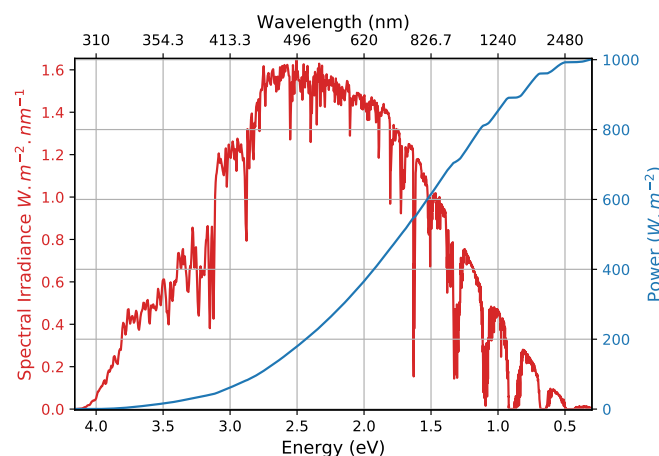
Figure 1.1: Solar Irradiance ASTM-G173 Standard AM1.5G

1.1 Solar Cell Theory

The perovskite material is merely one component within a working solar cell which converts the energy from incoming photons to usable electrical energy via the photovoltaic effect. From the theory of quantum mechanics, electrons must occupy discrete energy levels within an atom, with the highest occupied level referred to as the valence energy level. Solid materials consist of many atoms on the order 10^{23} within a crystal or amorphous structure. The discrete energy levels of each atom forms within the solid energy bands, with an occupied valence band and an unoccupied conduction band. The gap between the valence band maximum (VBM) and conduction band minimum (CBM), which electrons can't occupy are dictated by the structure and type of atoms within a solid and referred to as the energy gap or band gap (Eg). A solid is classified as either a conductor, insulator or semiconductor, dependent on the size of the energy gap. Conductors have an overlapping valence and conduction, with an energy gap of 0 eV thus resulting in high conductivity. Insulators have energy gaps exceeding 9 eV, with semiconductors falling between an insulator and a conductor. [5].
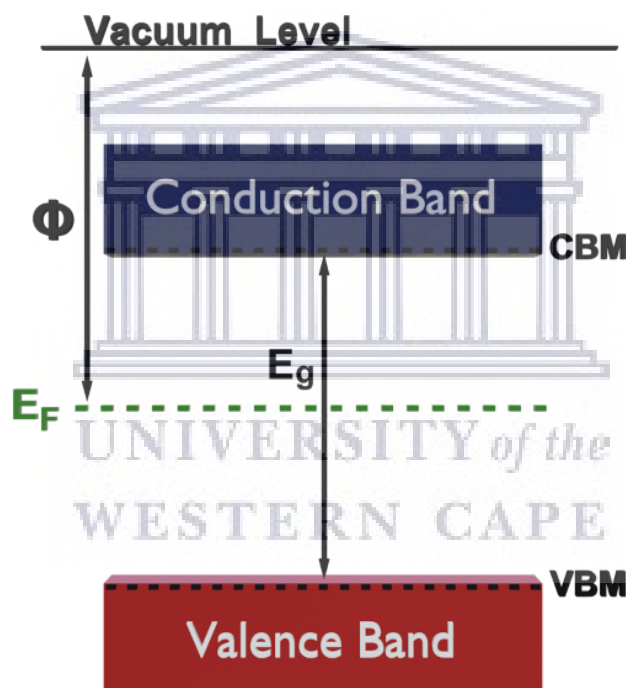
Figure 1.2: Band Structure

Perovskite solar cells are most commonly constructed with the n-i-p or p-i-n (inverted) architecture with the intrinsic perovskite material in between the n-type and p-type semiconductors also referred to as the electron (ETL) and hole transporting layer (HTL). The solar cell is constructed on top of a transparent conductive oxide (TCO) which is a layer of glass coated with a thin film of highly doped metal oxide. The two most used are indium tin oxide (ITO) and the more thermally stable fluorine-doped tin oxide (FTO). The last component is the metal back contact which must form an ohmic contact with the layer beneath it by having the appropriate work function (Φ). The n-type/metal connection requires that $\Phi_S > \Phi_M$ and for the p-type/metal connection $\Phi_S < \Phi_M$. One of the

main disadvantages of the n-i-p architecture is that it requires a metal with a large work function thus expensive gold ($\Phi_M = 5.1$ eV) is widely used also due to its high chemical stability. The p-i-n architecture can therefore utilise an inexpensive thin film of aluminium ($\Phi_M = 4.1$ eV).[6]

The basic working principle of the solar cell is that an incoming photon travels through the TCO and either the ETL or HTL which needs to have the highest possible transparency. If the photon has an energy greater or equal to the band gap of the perovskite an electron-hole pair is generated. The thicker the perovskite material the more photons can be absorbed. However, the thickness must be less than its diffusion length to prevent recombination of the electron-hole pair. Excited electrons migrate towards the ETL and holes to the HTL where it is either conducted by the TCO or metal. For optimum performance band gap alignment is essential as seen in fig. 1.3(b) The CBM of the ETL must be lower than that of the perovskite to prevent the formation of a potential barrier that would not allow electrons to be freely conducted. Optimum performance also requires the energy offset between the two CBM to be kept to a minimum. The VBM of the ETL must also be lower than that of the perovskite in order to block migrating holes. The CBM and VBM of the HTL must be higher than that of the perovskite to allow the migration of holes and blocking of electrons. Since the perovskite solar cells are constructed with a metal back contact, any light that is not absorbed by the perovskite can be reflected back providing a higher probability of absorption. Thin (<10 nm) wide bandgap materials are often used as interface layers which aid in the reduction of recombination between layers typically used at the perovskite interfaces and between the ETL and metal in the p-i-n architecture.[7]
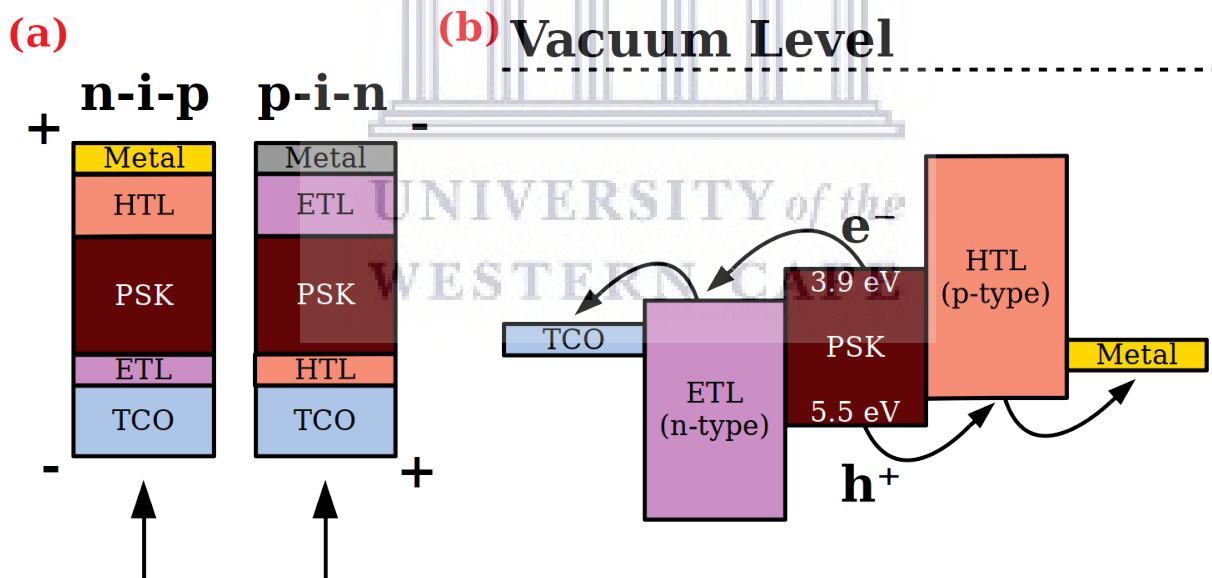
Figure 1.3: (a) Solar Cell Architectures and (b) Band Diagram

The performance of a solar cell is evaluated by an IV-curve by evaluating the current generated as a function of voltage. As convention the current density (J) is used in terms of mA/cm^2 to compare the performance of solar cells of different areas, J is also multiplied by -1 to allow generated current to be plotted in the first quadrant. Fig. 1.4 illustrates the single diode model equivalent circuit which is used for modelling the solar cell JV-curve, which includes resistive power loss due to low shunt resistance (R_{sh}) and high series resistance (R_s). The equivalent circuit is expressed by eq. 1.1b where J_0 is the saturation current density, J_{ph} is the photo-generated current density and n is the ideality factor which compensates for a solar cell that deviates from the mathematical ideal diode typically with values between 1 and 2.V_T is the thermal voltage which depends on the absolute temperature (T) of the solar cell as well as the Boltzmann constant (k_B) and the elementary charge (q). The solar cell model can be improved by adding an additional diode parallel to the first to compensate for recombination with different J_0 and n values. Since J can't be determined directly when $R_s \neq 0$, eq. 1.1b can be written in terms of the Lambert W function (eq. 1.2d).
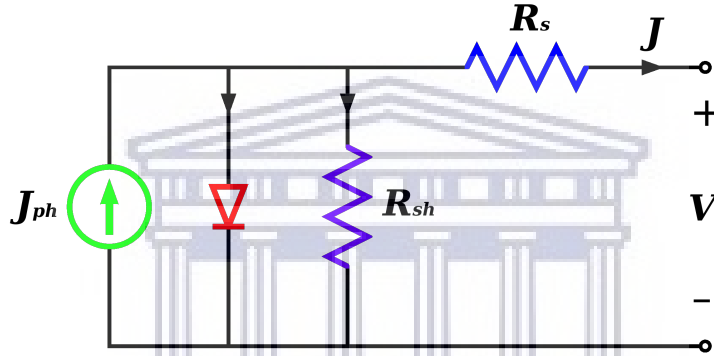
Figure 1.4: Circuit Diagram of Single Diode Model

$$V_T = \frac{k_B T}{q} \tag{1.1a}$$

$$J = J_0 \left(\exp\left[\frac{V - JR_s}{nV_T} \right] - 1 \right) + \frac{V - JR_s}{R_{sh}} - J_{ph} \tag{1.1b}$$

$$t_1 = \frac{J_0 R_s}{nV_T(1 + R_s/R_{sh})} \tag{1.2a}$$

$$t_2 = \frac{V}{nV_t}\left(1 - \frac{R_s}{R_s + R_{sh}} \right) + \frac{(J_{ph} + J_o)R_s}{nV_t(1 + R_s/R_{sh})} \tag{1.2b}$$

$$t_3 = \frac{J_{ph} + J_0 - V/R_{sh}}{1 + R_s/R_{sh}} \tag{1.2c}$$

$$J = \frac{nV_T}{R_s} W(t_1 \exp[t_2]) - t_3 \tag{1.2d}$$

The PCE is determined from the maximum point (mp), which is the largest amount of power that can be extracted from the solar cell. As seen fig. 1.1 solar cells are tested according to the ASTM-G173 standard of AM1.5G which equates to a input power (P_{in}) of 1000 W/m^2. Another common parameter is the fill factor (FF) eq. 1.3b, which is the fraction of output power compared to the product of the J_{SC} and V_{OC}. Fig. 1.5 illustrates the impact of shunt and series resistance on two solar cells with the same J_0, J_{ph} and n. Solar cell (a) is an example of a typical JV-curve of a perovskite cell in literature with a high PCE of nearly 18%. Solar cell (b) has a reduced R_{sh} which affects the linear region between the J_{sc} and mp. The increase in R_s affects the linear region between the mp and V_{OC}. Changes in R_{sh} and R_s affects mostly the mp, with only a minor difference in the J_{SC} and V_{OC}, thus most power loss results in a reduction in the FF.
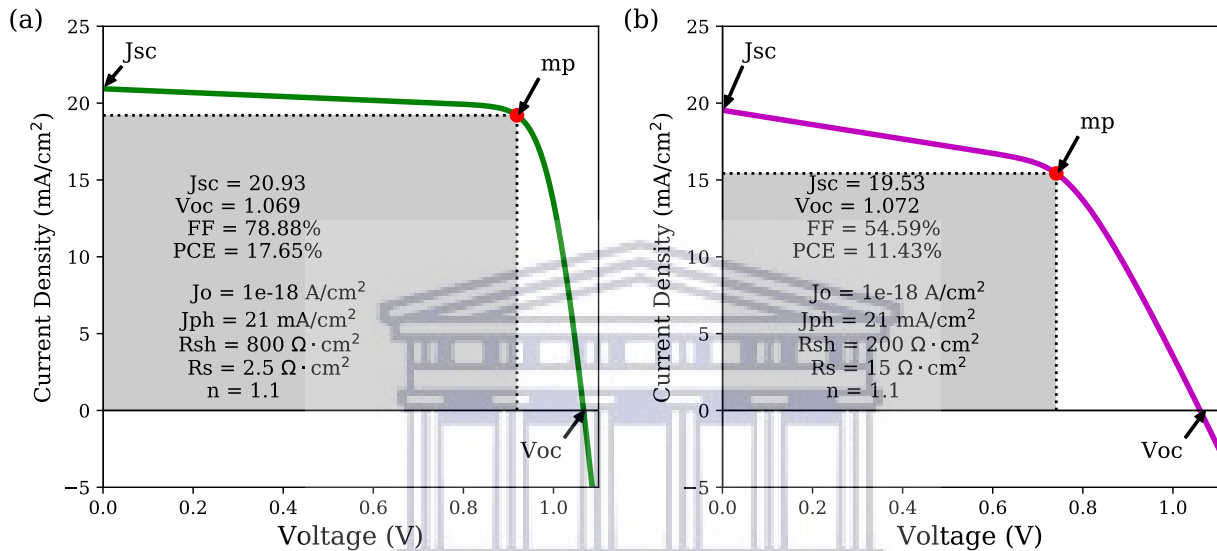
Figure 1.5: JV Curve

The J_{SC} and V_{OC} of a single junction solar cell is directly related to the bandgap (E_g) of the absorber material. The J_{SC} is determined by eq. 1.3c were the spectral flux ($\Phi_{AM1.5G}$) and external quantum efficiency (EQE) is integrated over the range of incident photons with a wavelength greater or equal to the E_g of the absorber material, therefore the J_{sc} is inversely proportional to the bandgap of the absorber material. The EQE is the ratio of collected photons to incident photons as a function of wavelength. Therefore in the example of the n-i-p perovskite solar cell the less light that travels through the glass, TCO and ETL and is absorbed by the perovskite the lower the EQE.

The V_{OC} (eq. 1.3d) can be derived from eq. 1.1b when $J = 0$, approximating that J_{SC} = J_{ph} and that the contribution of R_{sh} is negligible. Since V_{OC} is dependent on both J_0 and n an accurate value is not easily determined. However the maximum possible V_{OC} is limited to the bandgap of the absorber material, the energy of a photon that exceeds the bandgap results in the generation of phonons which are vibrations in the lattice and results in the loss of energy in the form of heat in the the process known as thermalization.[8] Due to recombination the V_{OC} will be slightly less than the bandgap. The GaAs Solar cell developed by Alta Devices has the highest PCE (single junction) of 29.1% with a V_{OC} of 1.127 V 79% of it's bandgap.[9] According to the well-known Shockley-Queisser limit, the maximum energy that can be extracted by a single-junction solar cell based on AM1.5G is

33.7% for an E_g of 1.34 eV. There is also a broad range between 1.0 and 1.6 eV that can provide in excess of 30% efficiency.[10]

$$PCE = \frac{P_{out}}{P_{in}} = \frac{V_{mp}J_{mp}}{P_{in}} \tag{1.3a}$$

$$FF = \frac{V_{mp}J_{mp}}{V_{OC}J_{SC}} \tag{1.3b}$$

$$J_{sc} = q \int_{E_g}^{\infty} \Phi_{AM1.5G}(E) \ EQE(E) \ dE \tag{1.3c}$$

$$V_{OC} = nV_T \ln\left(\frac{J_{SC}}{J_0} + 1\right) \tag{1.3d}$$

1.1.1   Hysteresis and Stabilized Efficiency

The PCE of a perovskite solar cell typically varies depending on the scan direction this difference is known as hysteresis. The hysteresis index (HI) is determined in various ways, the simplest method is to compare the forward and reverse PCE as seen in eq. 1.4, since these values are commonly provided in literature, this method will be used to compare results from this work. A more in-depth method is to integrate the JV-curve comparing the area under the curve from the forward and reverse scan.[11] [12]

$$HI = \frac{PCE_{rev} - PCE_{fwd}}{PCE_{rev}} \tag{1.4}$$

The PCE can also be affected by the scan speed, with the PCE typically deceasing with slower scan rates, which ideally should not be greater than 10 mV/s. Maximum power point tracking (mppt) is used as a more objective means of evaluating the PCE of perovskite cells, by tracking the maximum point of the JV-curve for at least one minute establishing a stabilised PCE measurement. [13] [14]

1.2   Perovskite Materials

Perovskite refers to all materials with the ABX_3 crystal structure similar to calcium titanate ($CaTiO_3$) as seen in fig. 1.6. A and B are both cations and X is the negatively charged anion. There are a wide variety of useful compounds with the perovskite structure of which the lead halides has gain tremendous attention in the past decade for solar cell application. Due to its low cost and simplicity of manufacturing, there has been thousands of published articles with several research groups achieving certified efficiencies in excess of 20%. (see tab. 1.1)
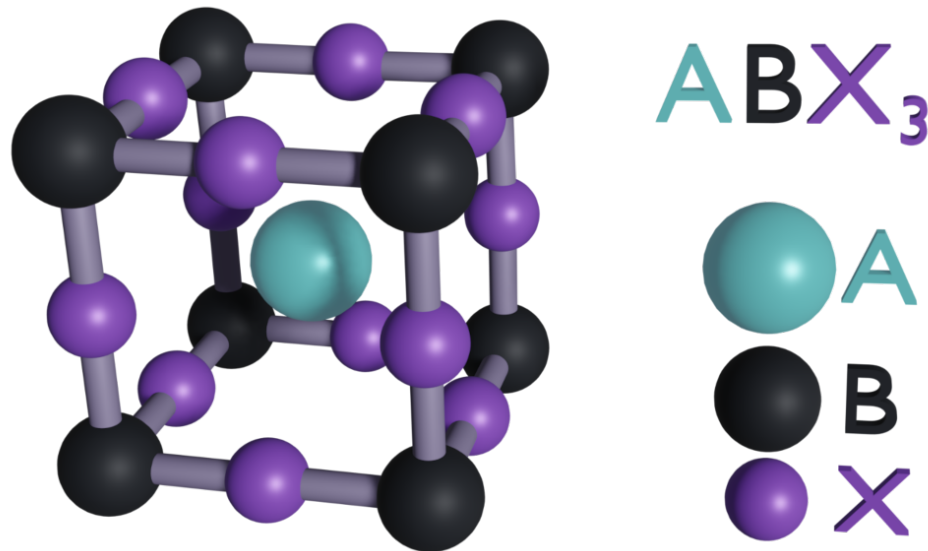
Figure 1.6: Perovskite Structure

There are many different lead halide perovskites. However, its stability is greatly dependent on the ionic radii of its constituent ions commonly described by the Goldschmidt's tolerance factor (t) [15] and octahedral factor (μ)[16]:

$$t = \frac{r_A + r_x}{\sqrt{2}(r_B + r_x)} \tag{1.5a}$$

$$\mu = \frac{r_A}{r_x} \tag{1.5b}$$

where r_A and r_B are the ionic radii of the cations and r_x is the ionic radius of the anion. Ideally to form the most stable cubic perovskite structure t must be between 0.89 and 1 and $\mu > 0.41$ [17] Within the lead halide perovskite field there are 3 main A cations, the organic formamidinium (FA) and methylammonium (MA) and the inorganic Caesium (Cs) with ionic radii of 253, 217 and 181 pm.[18] Since the organic A cations are molecules the effective radii (r_{Aeff}) must be determined as follows:

$$r_{Aeff} = r_{mass} + r_{ion} \tag{1.6}$$

where r_{mass} is the distance between the centre of mass of the molecule and the atom furthest from the centre, excluding hydrogen atoms and r_mass is the ionic radius of the furthest atom. A more precise determination has been done by Becker et al. (2017) with the use of first-principle calculations providing ionic radii of 277 and 238 pm for FA and MA respectively.[19]

The most commonly used ionic radii for iodide and the divalent lead cation with 6 fold coordination based on Shannon (1976)[20] is 220 and 119 pm respectively. However, the Shannon ionic radius of lead is based on oxides, it has been studied that the ionic radii of lead depends upon the halide, for iodide, bromide and chloride the radii of lead are 103, 98 and 99 pm respectively.[21]

The tolerance factor based on the revised radii provide values of 1.09, 1.00 and 0.88 for FAPbI$_3$, MAPbI$_3$ and CsPbI$_3$ perovskites with μ of 0.47. Although the Goldschmidt's tolerance factor is a simplistic method to evaluate stability it accurately predicts that MAPbI$_3$ is the most stable having a tetragonal phase at room temperature and cubic at 57 °C . Both FAPbI$_3$ and CsPbI$_3$ are most stable at room temperature in its non-perovskite (yellow) δ-phase. However, with the appropriate dopant a stable α-phase perovskite can be formed.[22]

The bandgap of the perovskite is inversely proportional to the atomic number of the halide as seen in fig. 1.7 which contains experimental energy levels obtained by ultraviolet photoelectron spectroscopy (UPS). As described in chapter 1.1 the ideal band gap range for a single junction solar cell is between 1 and 1.6 eV, therefore the optimum materials are FAPbI$_3$ and MAPbI$_3$.

All perovskites in the band diagram below were produced and studied by the same research group. It is of great importance to note that the iodide based perovskites are p-type, since the Fermi level is above the centre of the bandgap, close to the conduction band minimum (CBM). The CBM and VBM values of MAPbI$_3$ also differ from the most commonly quoted values in literature of 3.9 and 5.5 $\pm$ 0.1 eV.[23]

MAPbI$_3$ can either be an n-type, p-type or intrinsic semiconductor depending on the Pb to MA ratio. N-doping occurs when Pb/MA > 1 which results in MA vacancies and when Pb/MA < 1 the material becomes p-doped due to Pb vacancies.[24] A study by Cui et al (2019) used this property to form a homojunction consisting of a 480 nm thick n-type and 60 nm thick p-type MAPbI$_3$ layer. The solar cells consisting of the homojunction layer between TiO$_2$ (ETL) and Spiro-Omatad (HTL) produced an average PCE of 20.0 $\pm$ 0.4 % compared to 15.9 $\pm$ 1.1% obtained with an intrinsic MAPbI$_3$ layer as measured from 45 cells. The increased performance is due to a smaller energy difference between the Fermi level of the transport layers and that of the perovskite, which improves charge extraction. [25]
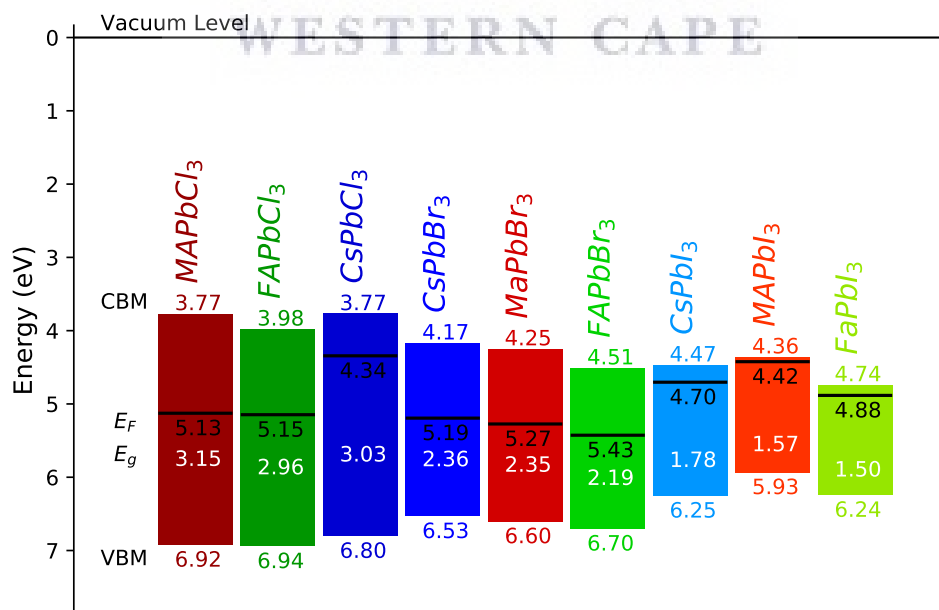
Figure 1.7: Lead Perovskite Band Diagrams (adapted from ref. [1])

For the purpose of visualization, the different molecules discussed in this thesis were constructed in Avogadro software with geometry optimization using Universal force fields (UFF).[26] All molecules are depicted on the same scale as seen in fig. 1.8 in addition to atoms drawn using Van der Waals radii.
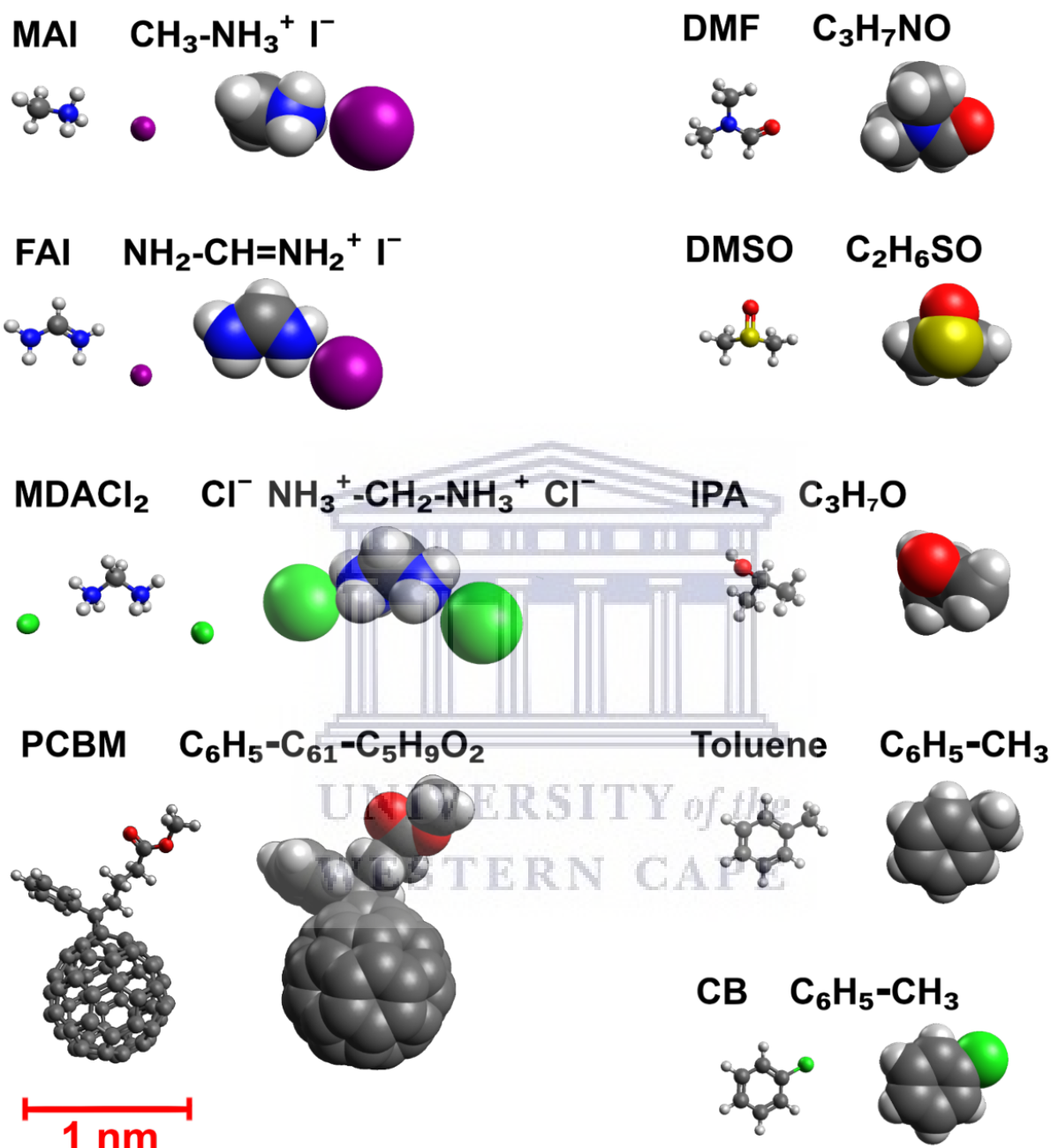
Figure 1.8: Organic Molecules

1.3 Progression of Solar Cell Record Efficiency

The perovskite materials were first used in dye sensitized solar cells with the use of meso-porous titanium particles and a liquid electrolyte as early as 2006 which provided a modest PCE of 2%.[27] In 2012 the perovskite solar cells transitioned to solid-state solar cells with the use of the organic HTL, Spiro-OMeTAD. The solar cell provided an increased PCE of 9.7% and an improved in stability over the dye sensitized solar cells.[28] The n-i-p architecture (tab.1.2 no. 4) consisted of FTO coated glass as the TCO, a thin compact layer of TiO_2 as the ETL, then a mixture of a mesoporous TiO_2 and $MAPbI_3$ perovskite as the absorber material, Spiro-OMeTAD HTL and 60 nm thin film of gold as the cathode electrode. This design laid the foundation of all further perovskite solar cells, with even the highest published PCE solar at the end of 2019 of 23.7% being a variation of the 2012 architecture.[29]

The last decade has seen a tremendous improvement in the PCE of the perovskite solar cells, fig. 1.9 is a collection of all the record efficiencies with extracted JV-curves to visualize the improvement in performance. Each record efficiency is labelled from 1 to 16 in order of date published with performance parameters listed in table 1.1 and a detailed comparison of architectures in table 1.2.
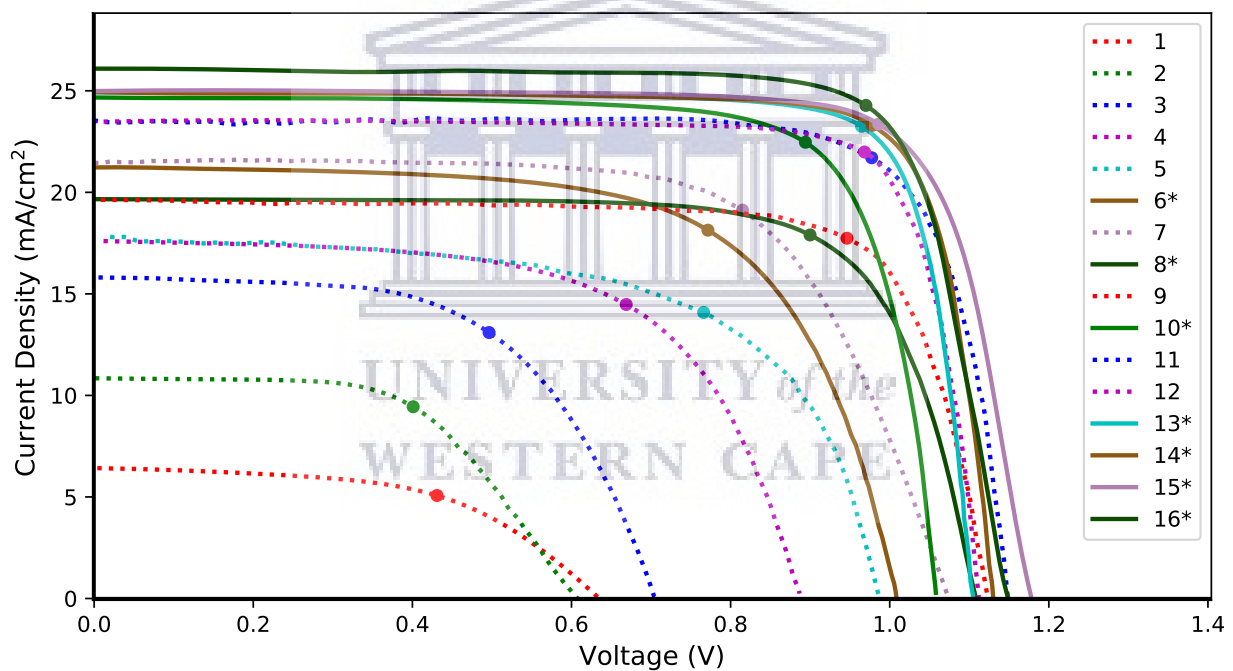
Figure 1.9: Record Efficiency JV-Curves (* certified)

Table 1.1: Efficiency Progression Performance

#	Published	J_{sc} (mA/cm^2)	V_{oc} (V)	FF (%)	PCE (%)	HI(%)	Inst.	Ref.
1	Oct. 2006	6.44	0.64	53	2.19		a, b	[27]
2	Apr. 2009	11.0	0.61	57	3.81		c, b	[30]
3	Sept. 2011	15.82	0.706	58.6	6.54		d	[31]
4	Aug. 2012	17.6	0.888	62	9.7		d, e	[28]
5	Nov. 2012	17.8	0.98	63	10.9		f, b	[32]
6*	July 2013	21.27	1.007	65.7	14.14		e	[33]
7	Sept 2013	21.5	1.07	67	15.4		f	[34]
8*	July 2014	19.64	1.11	74.2	16.15	0.63	g, d	[35]
9	Aug 2014	22.75	1.13	75	19.3	22.1	h	[36]
10*	June 2015	24.65	1.059	77	20.11	0.58	g, d	[37]
11	March 2016	23.51	1.147	78.5	21.17	4.02	e	[38]
12	April 2017	23.4	1.12	81.3	21.3	32.71	g, i	[39]
13*	June 2017	24.95	1.105	80.3	22.13	1.77	j, g	[40]
14*	July 2018	24.92	1.127	80.5	22.60	3.02	g, d, j	[41]
15*	April 2019	25.23	1.179	78.4	23.32	1.74	k	[42]
16*	Nov. 2019	26.09	1.150	79.1	23.73	4.89	j	[29]

*Certified JV Characterization
[a]Tokyo Polytechnic University, Japan
[b]Toin University of Yokohama, Japan [Tsutomu Miyasaka]
[c]University of Tokyo, Japan
[d]Sungkyunkwan University, South Korea [Nam-Gyu Park]
[e]Ecole Polytechnique Fédérale de Lausanne, Switzerland [Michael Grätzel]
[f]University of Oxford, UK [Henry J. Snaith]
[g]Korea Research Institute of Chemical Technology (KRICT), South Korea [Sang Il Seok]
[h]University of California (UCLA), USA [Yang Yang]
[i]Massachusetts Institute of Technology (MIT), USA
[j]Ulsan National Institute of Science and Technology (UNIST), South Korea [Sang Il Seok]
[k]University of the Chinese Academy of Sciences (UCAS), China [Jingbi You]

Table 1.1 consists of only a fraction of all the research institutions that have contributed to the rapid progression in PCE. One of the main reasons for the large amount of contributions is the accessibility of the solution based spin-coating technique for rapid prototyping. Another key role has been solvent engineering which leads to reductions in defects within the perovskite material. Solvent engineering involves the addition of DMSO to the perovskite precursor solution, which when spin-coated leads to the formation of an intermediate DMSO complex in order to prevent the rapid crystallization of the perovskite material, secondly a non-polar anti-solvent for example toluene dropped onto the spinning sample near the end of the spin-coating which results in larger grains with less defects, by more effectively removing the solvent and improving crystal nucleation. Samples are then annealed typically at 100°C to remove the DMSO and from the perovskite thin film.[43]

The lead halide perovskites are also sensitive to moisture especially during the spin-coating process, where an increase in relative humidity (RH) leads to poor film morphology, which results in a PCE below 5%. Thus a glovebox is essential for obtaining high and repeatable efficiencies. Solvent engineering has been used to reduce the moisture sensitivity during spin-coating, with the use of acetyl acetate as an anti-solvent, which resulted in a PCE of 15% at a RH of 75%.[44]

Table 1.2: Efficiency Progression Architecture

#	TCO	ETL	Perovskite	HTL	Electrode
1	FTO	m-TiO$_2$ (Titania Paste) Squeeze Method Annealing at 400°C 1h	MAPbBr$_3$*	Electrolite 0.2M LiI, 0.1M I$_2$ ACN†, IBN†	Pt coated Glass
2	FTO	TiCl4 Treated 8 μm m-TiO$_2$ 480 °C 1h	MAPbI$_3$* GBL†	50 μm Electrolite 150mM LiI, 75mM I2 Methoxy-ACN†	Pt coated FTO glass
3	FTO TEC-8	c-TiO$_2$* 500°C 15min. 0.1M TiIA, Butanol† 3.6μm m-TiO$_2$ 20nm PTC 550°C	MAPbI$_3$* 1.29M MAI, 1.29M PbI$_2$ GBL† 100°C 30min.	25μm Electrolite 0.9M LiI, 0.45M I$_2$, 0.5M tBP, 0.05M Urea Ethyl Acetate†	Pt coated FTO glass
4	FTO TEC-8	c-TiO$_2$*, 0.3M TiIA Butanol† 0.6 μm m-TiO$_2$ 550°C 1h	MAPbI$_3$* 1.24M MAI, 1.24M PbI$_2$ GBL† 100°C 30 min.	580nm Spiro-OMeTAD* 170mM Spiro, 64mM LiTFSI, 198mM tBP CB†:ACN†, 1:0.1	60nm Au§
5	FTO TEC-15	50nm c-TiO$_2$¶ TiIA, Ethanol† 0.5μm m-Al$_2$O$_3$* Ethanol† 550°C 30min.	MAPbI$_2$Cl* 0.9M MAI, 0.3PbCl$_2$ DMF† 100°C 30min.	250nm Spiro-OMeTAD* 68mM Spiro, 9mM LiTFSI, 55mM tBP, CB† 12h Oxidation in Air	200nm Ag§
6	FTO TEC-15	30nm c-TiO$_2$¶ TiIA, Ethanol† 450°C 350nm m-TiO$_2$* 20nm PTC, 550°C 30min.	MAPbI$_3$** 1M PbI$_2$*, DMF† 63mM MAI, IPA† dipped 20sec. 70°C 30min.	100nm Spiro-OMeTAD* 59mM Spiro, 31.7mM LiTFSI 197mM tBP, 5.79mM CoTFSI CB†:ACN† 1:0.047	80nm Au§
7	FTO TEC-7	50nm c-TiO$_2$* TiIA, Ethanol† 500°C 30min.	330nm MAPbI$_{3-x}$Cl$_x$ § Co-Evaporation MAI:PbI$_2$, 4:1 Post Annealing 100°C 45min.	450nm Spiro-OMeTAD* 61mM Spiro, 26mM LiTFSI 55mM tBP, CB† 12h Oxidation in Desiccator	80nm Ag§
8	FTO TEC-8	70nm c-TiO$_2$¶ TiIA 450°C 200nm m-TiO$_2$* 50nm PTC, 500°C 1h	150nm 0.8M MAPbI$_{2.75}$Br$_{0.15}$* GBL:DMSO 7:3 Drop Toluene‡ last 5sec. 100°C 10min.	100nm PTAA* 0.57mM PTAA, 5.9mM LiTFSI 34mM tBP Toluene†:ACN†, 1:0.01	100nm Au§
9	150nm ITO PEI Treated* 0.1wt% PEI 100°C 10min.	40nm Y doped c-TiO$_2$* 60mM Y-TiO$_2$, 30mM TiIA, Ethanol† 150°C 30min.	350nm MAPbI$_{3-x}$Cl$_x$* 2.2M MAI, 0.73M PbCl$_2$ DMF†, 90°C 1h 100°C 25min.	200nm Spiro-OMeTAD* 73mM Spiro, 27mM LiTFSI 68mM tBP, 5mM CoTFSI CB†:ACN†, 1:0.12	100nm Au§
10	FTO TEC-8	60nm c-TiO$_2$¶ TiIA 450°C 150nm m-TiO$_2$* 500°C 1h	500nm (FAPbI$_3$)$_{0.95}$(MAPbBr$_3$)$_{0.05}$** 1.3M PbI2(DMSO) 465mM FAI, 126mM MABr, IPA† 150°C 20min.	60nm PTAA* 0.57mM PTAA, 4.4mM LiTFSI 27mM tBP Toluene†:ACN†, 1:0.0075	100nm Au§
11	FTO Nippon 10 Ω/sq	30nm c-TiO$_2$¶ TiIA 450°C 150nm m-TiO$_2$* 30nm PTC, 450°C 30 min LiTFSI Treated	FA$_{0.79}$MA$_{0.16}$Cs$_{0.05}$Pb(I$_{0.83}$Br$_{0.17}$)$_3$* 500nm, 1.1M PbI$_2$, 0.2M PbBr$_2$ 1M FAI, 0.2M MABr, 63mM CsI DMF†:DMSO† 4:1, CB‡ 100°C 30min.	200nm Spiro-OMeTAD* 70mM Spiro, 35mM LiTFSI 231mM tBP, 2.1mM CoTFSI CB†	80nm Au§
12	FTO TEC-8	70nm c-TiO$_2$¶ 20mM TiIA, 450°C 120nm m-LBSO*, 2ME† 19nm PTC, 500°C 1h	380nm MAPbI$_3$* 0.8M PbI$_2$, 0.8M MAI 2ME†:GBL†:DMSO† 7:4:3, Toluene‡ 100°C 10min.	80nm PTAA* 0.56mM PTAA, 5.9mM LiTFSI 34mM tBP Toluene†:ACN†, 1:0.015	80nm Au§
13	FTO TEC-8	60nm c-TiO$_2$¶ TiIA, 450°C 150nm m-TiO$_2$*, 2ME† 500°C 1h	500nm (FAPbI$_3$)$_{1-x}$(MAPbBr$_3$)$_x$** (1.3M PbI$_2$, 33mM PbBr$_2$, DMF†:DMSO† 4:1) (0.465M FAI, 89.3mM MABr, 3mM I$_3$, IPA†), 150°C 30min.	50nm PTAA* 0.57mM PTAA, 4.4mM LiTFSI 27.3mM tBP Toluene†:ACN†, 1:0.0075	100nm Au§
14	FTO TEC-8	30nm c-TiO$_2$¶ 20mM TiIA, 450°C 150nm m-TiO$_2$* 500°C 1h	520nm (FAPbI$_3$)$_{0.95}$(MAPbBr$_3$)$_{0.05}$* 1.4M FAPbI$_3$, 69mM MAPbBr$_3$, 489mM MACl, DMF†:DMSO† (8:1) Ether‡, 150°C 10min.	160nm DM* 18mM DM, 17mM LiTFSI 98mM tBP CB†:ACN† (1:0.014)	80nm Au§
15	ITO	40nm c-SnO$_2$* 2.73 wt% colloidal SnO$_2$, H$_2$O† 150°C 30min.	800nm FA$_{(1-x)}$MA$_x$PbI$_3$** 1.5M PbI$_2$, DMF†:DMSO† (9:1) (523mM FAI, 40mM MAI, 133mM MACl, IPA†), PEAI treated, 150°C 15min.	250nm Spiro-OMeTAD* 59mM spiro, 31.7mM LiTFSI 205mM tBP CB†:ACN† (1:0.035)	80nm Au§
16	FTO Asahi 13 Ω/sq	60nm c-TiO$_2$¶ 20mM TiIA, 450°C 100nm m-TiO$_2$* 500°C 1h	500nm FAPbI$_3$* FAPbI$_3$, 3.8 mol% MDACl$_2$ DMF†:DMSO† (8:1) Iodide treated, 150°C 15min.	200nm Spiro-OMeTAD* 73mM Spiro, 42mM LiTFSI, 2.5mM CoTFSI 270mM tBP CB†:ACN†, 1:0.033	70nm Au§

*Spincoated, **Sequential Spincoated, ¶Spray pyrolysis, §, †Solvent, ‡Anti-solvent

The current efficiency record for a perovskite single junction solar cells is 25.5% produced by UNIST.[45] Unfortunately, no information is available in regards to cell design. The highest PCE in a published article is also by UNIST.[29]. The high PCE of 23.73% is primary due to the novel use of $MDACl_2$ (fig. 1.8) as a dopant to stabilise the perovskite phase of $FAPbI_3$ which had a bandgap of 1.47 eV. This reduction in bandgap compared to typical dopants that achieve a bandgap greater than 1.5 eV, resulted in the highest obtained current density. The record cell did not obtain the highest fill factor, probably due to the use of the most common perovskite architecture. Therefore, with further design optimisation this absorber layer could achieve even greater efficiencies.

The performance of a solar cell is dependent on its entire architecture. A major source of instability and cause of large hysteresis has been due to the compact TiO_2 (c-TiO_2) ETL. Many research groups have used a mesoporous TiO_2 (m-TiO_2) layer typically consisting of 20 nm nanoparticles between the perovskite and c-TiO_2 layers. The other alternative has been to replace the TiO_2 completely with SnO_2 with the highest PCE seen with cell design 15 in the tables 1.1 and 1.2.

1.4 Commercialization of Perovskite Solar Cells

In order for perovskite material to have any impact in the solar PV industry it will need to either outperform the existing technology in terms of cost ($/W_p$) potentially in the flexible panel market or Building Integrated Photovoltaics (BIPV). Perovskites can also be used to improve the efficiency of existing PV technology in a tandem cell configuration due to its property to change its band gap depending on its composition.

The last decade has seen a large decrease in the cost of crystalline silicon (c-Si) solar panels which ensured its dominance in the solar PV market with a 95% share in 2019 with costs ranging between 0.3 and 0.4 $/W_p$.[46] The annual production of thin film panels in 2019 was 7.5 GW compared to 129.3 GW of c-Si. In recent years there had been a transition from poly- to monocrystalline silicon panels due to its higher PCE and cost reduction as seen in fig.1.10. Currently 66% of PV panels are manufactured in China with the global leading companies being Jinko Solar, JA Solar and Trina Solar that have shipped 14.2, 10.3 and 9.7 GW of solar panel capacity in 2019. [47]
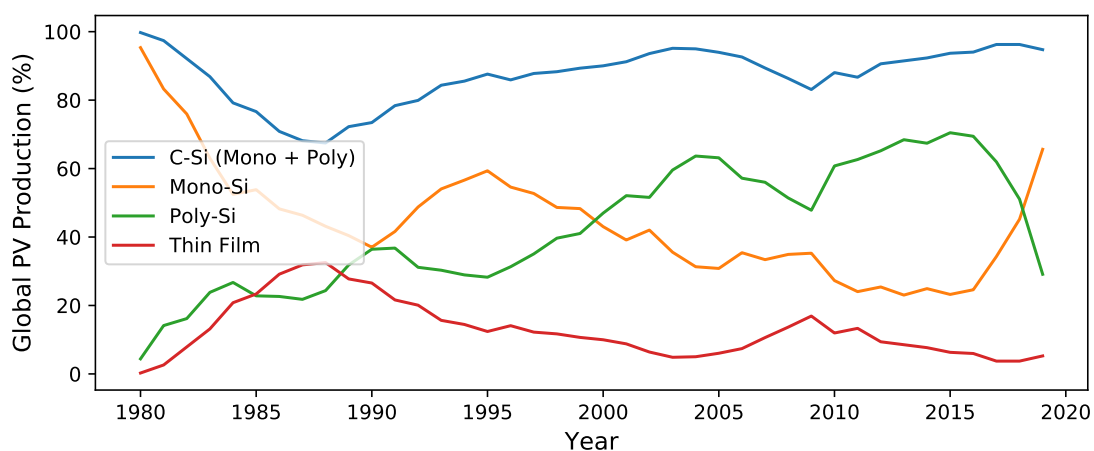
Figure 1.10: Global PV Production Comparison by Technology [2]

The record PCE for a monocrystalline Si laboratory cell is 26.7% (79 cm^2) set in 2017 with a module efficiency of 24.4 % (1.31 m^2) achieved by Kaneka, a Japanese chemical manufacturing company which has a 140 MW amorphous silicon (a-Si) factory. The record cell uses a heterojunction interdigitated back contact (HJ-IBC) design with the use of doped a-Si charge transport layers, instead of the more commonly used passivated emitter rear cell (PERC) design. The record PCE of 23.8% (246cm^2) for a polycrystalline cell was set in 2020 by Canadian Solar the fifth largest manufacturer in 2019 with 8.5 GW. The record module efficiency is 20.4% (1.48 m^2) by Hanwa Q in 2019 (6th largest 7.3 GW).[9] [47]

There are three main types of thin film absorber materials, cadmium telluride (CdTe), copper indium gallium selenide (CIGS) and a-Si. The vast majority of thin film panels are produced by one company, First Solar (USA) with sole focus on utility scale (>1 MW) installations of CdTe panels, which shipped a total of 5.5 GW in 2019 (8th largest), which accounted for 73% of the thin film market. First Solar has set a cell PCE record at 22.1% (0.4 cm^2) in 2015 and a record module PCE of 19.0% (2.36 m^2). The leading company in CIGS technology is Solar Frontier (Japan) with a 1.05 GW manufacturing capacity. Solar Frontier has achieved a cell record efficiency of 23.4 % (1 cm^2) in 2018, with a module PCE of 19.2% (0.084 m^2). Solar Frontier have commercial panels (SFK195-S) with a maximum power rating up to 17.5 % (1.23 m^2), which is slightly less than First Solar's series 6 panels at 18.3% (2.52 m^2).[9][48][49]

Decades of research has been devoted to develop the ideal thin film absorber material that can achieve high efficiency which can be sourced from natural abundant compounds and that has low toxicity. Due to the scarcity of tellurium and indium as well as the toxicity of cadmium both CdTe and CIGS could be limited in their future development. Kesterites has been proposed as a suitable solution, unfortunately its record PCE has stagnated at 12.6% (0.42 cm^2) with the use of a $Cu_2ZnSnS_{4-y}Se_y$ since 2013.[9]

Recent years has seen an increase in focus towards improving the module efficiency of perovskite solar cells. The Japanese organization, New Energy and Industrial Technology Development (NEDO) partnered with Toshiba to produce a 703 cm^2 module with a PCE of 11.3% in 2018. NEDO also collaborated with Panasonic which uses a one-step ink printing technique of the perovskite layer to produce a 804 cm^2 module with a PCE of 17.9% in 2019. [9]

There are currently two promising perovskite start-up companies that have both received funding in excess of $50 million in order to setup 100 MW production lines within the next few years. The first is Oxford PV, which aims to create a c-Si/perovskite tandem cell with a PCE exceeding 30%. In December 2020 Oxford PV regained the record cell PCE with 29.52% (1.1 cm^2), slightly more than the 29.15% (1.1 cm^2) that was set by Helmholtz-Zentrum Berlin (HZB) in January 2020. The second is the Chinese company Microquanta, which aims to produce a low-cost perovskite single junction solar panel. Their current record mini-module of 19.3 cm^2 has PCE of 18.04% (2019). Both companies are yet to produce large modules (> 1 m^2). Even though Oxford PV has showcased several 244 cm^2 monocrystalline silicon wafers created into a tandem cell no module PCE values have been published.[50] [51]

As companies begin to manufacture perovskite solar modules, much of this ground-breaking research will only be published in patents. Since the aim of patents is only to protect intellectual property, patents only disclose the most necessary information and a broad range of parameters and materials instead of specific information. For example Microquanta

has pulished several patents on various scalable techniques. A US patent has been granted in 2019 specifically on the use of CVD, alluding to the viability CVD perovskite research.[52] Unfortunately since their deposition parameters are too broad their experiments can't be replicated.

In terms of PCE, perovskite cells clearly show great potential. First Solar with there 18.3 % modules retain 83% of their record cell PCE. If perovskite modules can retain a similar fraction of its current record PCE (25.5%) then modules with a PCE in excess of 20% could be reality in the near future. It has been speculated that perovskite panels would cost approximately \$30 per m^2 with a module PCE of 20% this would amount to 0.15 \$/W_p.[53] However this would mean that gold can't be used as a back contact, since with a gold price of \$60 per gram the material cost of a modest 50 nm contact layer would amount to 0.29 \$/w_p (module PCE of 20%) which is nearly the cost of commercial c-Si panel. Therefore any perovskite research using a gold back contact for improved efficiency and stability is not a true representation of a commercial product's performance.

Even if module efficiency targets are met, the long-term stability is still a large concern. The c-Si/perovskite tandem cells are designed upon excising technology and will need to compete with the common c-Si manufacturing warranties. Solar panels typically have a product and performance warrantee. The first covers any manufacturing defects up to 10 to 12 years. The second stipulates a maximum linear degradation rate, typically panels must not degrade to less than 80% of its initial power rating after 25 years. Flexible c-Si panels are more expensive than rigid panels and some manufactures only offer a 5-year performance warranty, providing a opportunity for low cost perovskite solar modules to succeed in this market, if they can exceed the PCE of CIGS and CdTe. [54]

Commercial solar panels must under-go several stability certification tests. Two of the most difficult tests are part of the IEC-61215 which includes a 1000-hour stability test at 85 °C at a relative humidity (RH) of 85 %. The other test consists of 200 thermal cycles between -40 and 85 °C. In order to pass the IEC-61215 certification the cells must retain 95 % of its initial PCE. There is also the IEC-61646 certification that applies to thin-film solar panels that were specifically designed for a-Si, which is mostly identically to IEC-61215. With adequate encapsulation the perovskite solar panels would be protected from moisture, which could rapidly degrade the perovskite. Lead halide perovskite is most sensitive to moisture, since water molecules can penetrate within the structure forming a mono- or dihydrate perovskite as well as causing degradation forming HI and PbI_2.[55] The pure $MAPbI_3$ perovskite is also known to be thermally unstable at 85 % making it unsuitable for commercialisation, unless it can be stabilised with FA and Cs substitution.[56]

The lead toxicity is also a concern, that researches have attempted at addressing with the use of tin based perovskite, which has lower performance and much greater instability.[57] Even though elemental tin is a less of an environmental concern than lead, researchers have conducted studies that reveal tin based perovskite is more harmful to aquatic bio-diversity, due to its higher moisture instability leading to rapid degradation of acidic HI which lowers water pH, the lead based perovskite was more prone to form a Pb(OH)I precipitate with less HI. [58] When considering a typical thickness of 500 nm $MAPbI_3$ based perovskite it contains only 0.7 g of elemental lead per m^2 which is less than the lead used for "heat-resistant" soldering of commercial c-Si solar panels. The Restriction of Hazardous Substances (RoHS) does have several lead based industrial restriction, however solar panel manufacturers are exempted. [59] The tin based perovskite does have applications in full

perovskite tandem cells, since substituting a fraction of tin into the perovskite structure can lower the band-gap below 1.2 eV. [60]

The future of solar PV not only relies on technological improvements, but on its demand. One of the leading nations in large scale adoption of solar PV has been Germany. As seen in fig. 1.11 Germany rapidly began increasing its PV capacity after 2008 as the costs began to decrease and by 2020 just over 10% for its total generated electricity was produced from solar PV.[61] In 2011 The German government set a 52 GW PV capacity limit on feed-in-tariffs, which slowed the rate of solar installations. Fortunately in 2020 as Germany began to reach this limit plans were set to renegotiate future feed-in-tariffs to ensure that Germany can meet their 2030 target of having a total PV capacity of 100 GW.[62] Thus the politics of a nation has a large influence in the adoption of solar PV.
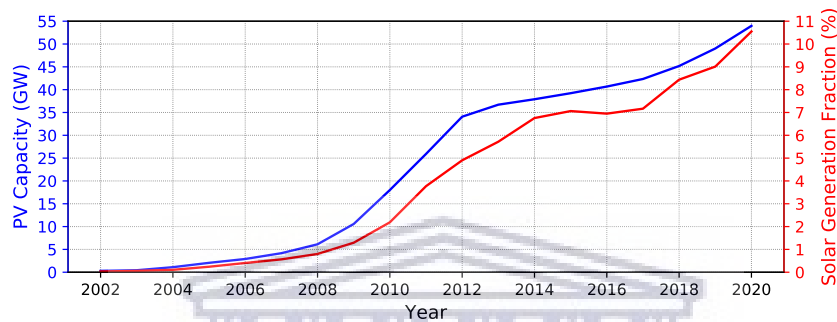
Figure 1.11: Solar PV Capacity and Generation Fraction of Germany

The total annual electrical load in Germany has not seen much change in the last decade with values fluctuating between 508 and 542 TWh, with not a great difference between 2010 with 489 TWh and 2019 with 484 TWh total load. In order to incorporate an increasing amount renewable energy into the German electrical grid, several coal and nuclear power stations were shut down. The fraction of annual energy generated by source during 2002 and 2020 is compared in fig.1.12. Shutting down existing coal and nuclear power stations could result in a large economical loss, if the stations are far from the end of their lifespans. This could slow down the development of new solar installations in the future due to a lack of demand. There was also an increase in natural gas, since it can be used for dispatchable energy generation to overcome some of the intermittency of wind and solar energy.[63] Therefore nations that are currently relying more on natural gas could more easily transition to renewable energy.
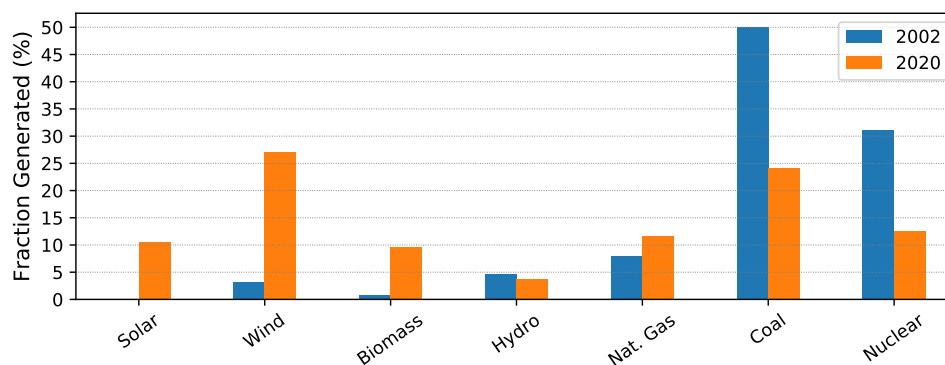
Figure 1.12: Germany Energy Mix

A main concern with solar PV is that it only generates energy between sunrise and sunset peaking at noon, which does not match the electrical grid load. This means that typical base load power stations need to be reduced in order to compensate for a large solar peak. This is commonly referred to as the duck curve. Thus the future of solar PV demand, relies on energy storage. Currently the most cost effective is pump-storage hydropower with capital costs varying between $106 and $200 per kWh of storage and between $1700 and $3200 per kW of power capacity. Unfortunately, pump-storage has specific geological requirements that can't be installed in any location, hence the increasing manufacturing of utility scale Li-ion battery storage facilities with a total project cost ranging between $393 and $581 per kWh of storage and between $1570 and $2322 per kW of power capacity. In terms of power capacity Li-ion battery storage is already more cost effective than hydro pump-storage and since it is only recently been used at the utility-scale cost could dramatically decrease in the future while cost of pump-storage will remain relatively the same. The cost of utility-scale Li-ion battery storage is expected to decrease by 23% in 2025. The cost analysis is from a 2019 study through the HydroWIRES initiative by the US Department of Energy National Laboratories. [64] Currently the largest Li-ion storage facility is Moss Landing (USA) with 1.2 GWh completed in Des. 2020 with a planned phase 2 expansion which will be completed by the end of 2021 creating a total storage capacity of 1.6 GWh. To put this in perspective, as of 2020 South Africa has a total of 2036 MW of PV solar farm capacity which on average generated 10.8 GWh of energy per day in 2020 (excluding Des.) meaning the 1.6 GWh storage facility would be able to store nearly 15% of the daily generated solar energy.[65]

Another important development that could offer a large amount of future solar PV energy storage is vehicle-to-grid (V2G). The system uses a portion of the energy stored in electrical vehicles (EV) to provide energy during peak load similar to using utility-scale battery storage facility, but with a network of potentially millions of cars in the future each with a battery capacity on the order of 50 kWh. [66]

Perovskite solar cell research is beginning to transition from academia to industry showing promise for commercialization with its largest obstacle being to create cells that can rival the stability of existing c-Si modules. The most likely deposition technique of perovskite will be solution based in either blade/slot-die coating or inkjet printing in a one step process. [51] However, CVD could potentially form part of the manufacturing technique, if it has a potential to improve the stability of solar modules. The next decade will see a large increase in solar PV demand, which perovskite would need to capitalise on. As more renewable energy is installed the requirement for energy storage will increase, which could negatively affect the demand for solar PV. Fortunately, Li-ion technology in the form of utility-scale storage and V2G could provide the needed storage with costs continuously decreasing.

1.5 Outline and Objectives

The aim of this thesis is to develop a scalable CVD technique of the MAPbI$_3$ perovskite material and to establish the ideal solar cell architecture to ensure a high PCE and long-term stability. The outline and objectives of each chapter will be discussed within this section.

The thesis is divided into three main chapters. Chapter two covers the background information needed to understand the various characterization techniques that were used, also including the calibration of certain techniques. Chapter three focuses on the optimization of the lead halide and perovskite depositions, as well as the characterization of these materials. Chapter four is an overview of the solar cell construction and the evaluation of its performance with alterations in design.

Chapter three deals with the method in which the lead halide layers using CVD is optimised for thickness and uniformity. This is to ensure repeatability in experimental results. This is also important, since the perovskite formation uses a sequential intercalation process to convert the lead halide layer into the desired perovskite absorber material for solar cell construction. The key focus is to determine the essential CVD parameters to ensure a stable perovskite conversion from the lead halide layers. The thin film materials are analysed using profilometry, UV-Vis spectroscopy, electron microscopy, X-ray diffraction and Rutherford backscatter spectrometry (RBS). This allows the characterization of morphology, crystal structure and elemental composition. The objective of chapter three is to develop a scalable perovskite deposition technique with the use of CVD, with focus on thickness uniformity and stability of the converted perovskite material.

The fourth chapter concentrates on the basic n-i-p solar cell design and the layout of the individual cells of a solar cell sample. The performance in terms of PCE and stability is characterised using IV characterization, where alterations within the various different layers can drastically impact the solar cell performance. The results from this work is also compared to similar solar cell designs in literature, which focusses on explaining the reasons for reduced performance in perovskite solar cells. The objective of chapter four is to determine the ideal solar cell architecture to maximize PCE and stability using the CVD perovskite.

The last chapter is a summary of the findings from this thesis and a brief outlook of how future research in this field can be improved.

Chapter 2

Characterization Techniques

This chapter focusses on the various characterization techniques used to determine the quality of the perovskite absorber layer and transport layers. The scientific background will be discussed as well as the calibration of equipment and measurements. An overview of the solar cell characterization software that was written for IV data acquisition and analysis of samples is also provided.

2.1 Profilometry

A Veeco Dektak 6M profilometer was used for thickness and roughness measurements of thin films. The profilometer uses a stylus with a 5 μm tip that can apply a variable force between 1 and 15 mg that scans over the surface, measuring fluctuations in height with a 1 Å minimum resolution. Thickness is measured by the height difference between the substrate and the surface of the thin film and is most accurate closest to the step. For thickness and roughness measurements 15 and 5 mg of force is used respectively, which provide the most accurate results. The roughness is calculated from the root mean square (rms) (eq. 2.1), where x_i is the individual height up to a total of n measurements. Since the stylus is significantly larger than that of an atomic force microscope (AFM) which has a tip radius of a few nanometres, the Dektak produces under estimations of the roughness.[67]

$$\text{rms} = \sqrt{\frac{1}{n}\sum_{i=1}^{n} x_i^2} \qquad (2.1)$$

2.2 UV-Vis Spectroscopy

2.2.1 Background

Light or electromagnetic radiation is the propagation of an oscillating electric and a perpendicular magnetic field of quantized packets of energy known as photons. Light has a particle-wave duality and can be described by classical and quantum physics. The energy of a photon is related to the frequency of the oscillating electric field and is described by

the Planck equation:[68]

$$E = \mathrm{h}\nu = \frac{\mathrm{hc}}{\lambda} \tag{2.2}$$

One of the main uses of UV-Vis spectroscopy is to study the energy gap (E_g) of a semiconductor. Most often in literature the Tauc method is used, which relates the energy gap to the absorption coefficient (α) of a material as follows:

$$(\alpha h\nu)^{1/\gamma} = B(h\nu - E_g) \tag{2.3}$$

where B is a proportionality constant and γ is a factor that depends on the type of electronic transition, for direct allowed transitions $\gamma = 0.5$ and indirect allowed transition $\gamma = 2$, there is also less dominant forbidden transitions where γ equals 1.5 and 3 for direct and indirect transitions respectively. The Kubelka-Munk function is used to transform diffuse reflectance spectra to absorption spectra as follows:[69]

$$F(R_\infty) = \frac{(1 - R_\infty)^2}{2R_\infty} \tag{2.4}$$

where $R_\infty = \frac{R_{sample}}{R_{standard}}$ the fraction of the reflectance of a sample to a standard. α in eq. 2.3 can be substituted by $F(R_\infty)$.

In order to approximate α from specular reflection (R_{meas}) and transmission measurements T_{meas} eq. 2.5 is used also taking into account the thickness (d) of the thin film.[70]

$$\alpha = -(1/d)ln[T_{meas}/((1 - R_{meas})^2 + R_{meas}T_{meas})], \tag{2.5}$$

By plotting $(\alpha h\nu)^{1/\gamma}$ versus $h\nu$ a Tauc plot is made which can be used to determine E_g by finding the x-intercept of the linear region of the plotted curve.[71]

A major concern with the use of this method is that it was originally developed for amorphous materials with thicknesses greater then 40nm. [72] Surface roughness can also increase the amount of diffuse scattering of light, which make specular reflection and transmission measurements less accurate at determining α.

2.2.2 Setup and Calibration

The electromagnetic spectrum is subdivided into several regions depending on its wavelength with visible light between 400 and 700nm, UV (ultra-violet) 10 and 400nm and Infrared 700nm to 1mm. ref. The wavelength range that can be studied depends upon the light source and spectrometer. The spectrometer that was used in this study is the ocean optics USB4000 with a detectable wavelength range between 200 to 1050nm. The spectrometer thus covers the entire visible range and also a portion of UV and NIR (Near Infrared).
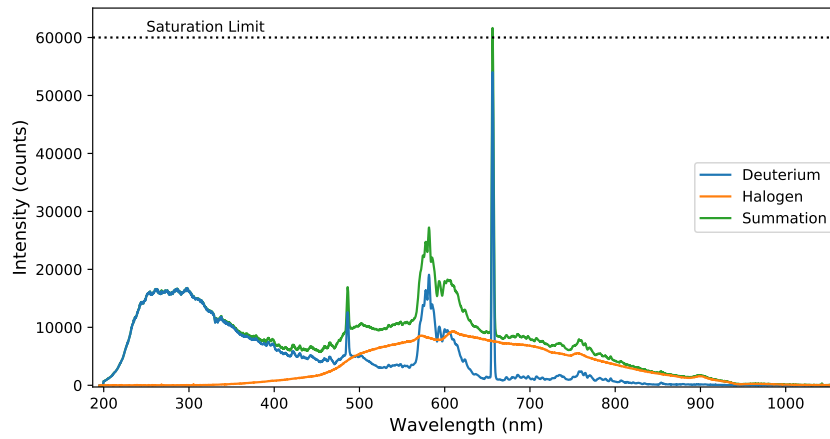
Figure 2.1: Spectrometer Light Sources

Light is transported by fibre optics cables from the light source to the sample and either the transmission or reflection cable is connected to the spectrometer for analysis. The spectrometer consists of several components as seen in fig. 2.2. Light of several wavelengths enter the spectrometer at the SMA connector (1) and the beam size is control by the slit (2) which is a rectangular aperture between 5 and $200\mu m$. The beam then passes through a filter (3) which restricts light to the desired wavelength range. Light then reflects off the collimating mirror, which reduces the spreading of the beam as it travels to the diffraction grating (5), which has 500 lines/mm, to separate light of different wavelengths. The separated light is then reflected off the focusing mirror (6) onto the collection lens (7), which reduces the height of the beam to better match the dimensions of the detector (8) to improve efficiency. The detector is a 16bit Toshiba TCD1304AP linear array with 3648 pixels ($8 \times 200\mu m$ pixel size) with each pixel covering a detectable range of 0.25nm. The OFLV filters (9) block second and third order diffracted light from reaching the detector and UV4 (10) is a replacement of a quartz window to the detector to increase light intensity below 340nm. (9) and (10) are optional upgrades to the spectrometer that is not part of this study.

1 SMA Connector
2 Slit
3 Filter
4 Collimating Mirror
5 Diffraction Grating
6 Focusing Mirror
7 L4 Detector Collection Lens
8 Detector
9 OFLV Filters
10 UV4 Detector Upgrade
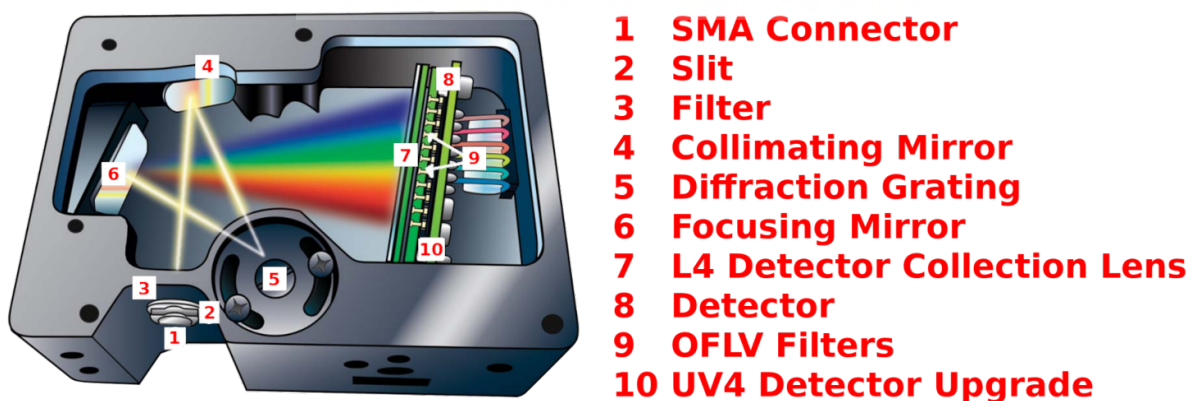
Figure 2.2: Ocean Optics USB4000 Spectrometer [3]

The optical setup was modified as seen in fig. 2.3 to enable the measurement of reflection and transmission of light on the same position of a sample. Since samples have thickness

and roughness variations the ability to conduct both measurements on the same position improves the accuracy of the absorbance calculation of the sample. The setup consists of a bottom probe that consists of 7 optical fibres as seen in fig. 2.4, a central fibre that collects reflected light from the sample and 6 surrounding fibres for illumination. The fibres are separated by two cables where the fibres for illumination is connected to the light source and the reflection cable connects to the spectrometer. The top probe is for transmission measurements which has a lens to focus light into its optical fibre, since the beam diverges as it travels to the probe. The setup also includes a shutter which is held in place by a clamp stand, this prevents transmitted light from reflecting off the transmission probe lens. The shutter is only necessary when working with semi-transparent samples on a glass substrate.
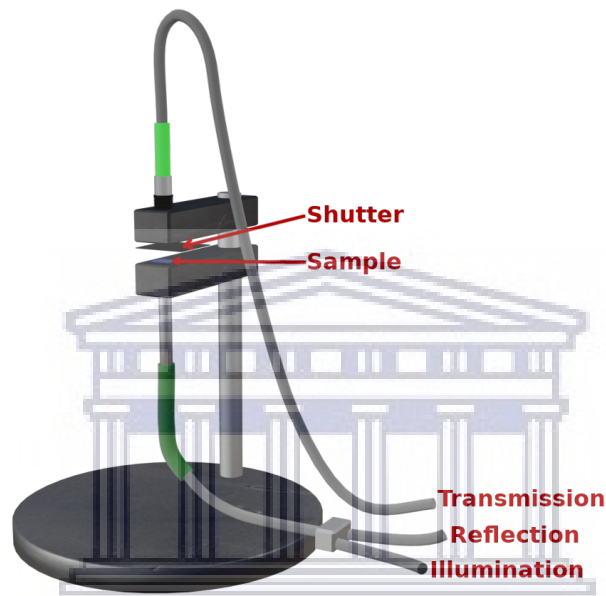
Figure 2.3: UV-Vis Setup

Before starting the measuring procedure the appropriate integration times are determined to gather the maximum number of counts without exceeding the limit of the the detector to maximize the Signal-to-Noise (SNR), for both the reflection and transmission measurements. Since the samples in this study had low reflectance, a bare silicon waver was used as the reflective standard to better match the reflectance of the samples, which allows for an improved SNR. The number of scans that are averaged are adjusted depending on the integration time, having a measurement duration of approximately 1 second. The box width is adjusted to 5 which groups channels to achieve a smoother spectrum.

The measurement procedure is as follows: a pre-calibrated reflective standard is placed face down above the reflection probe, with the shutter blocking the transmission probe. The integration time (30 to 70ms) and number of averaged scans are adjusted, once the adjustments have been made the standard is replaced with the sample making sure not to adjust the optical fibre cables which would change the measured light intensity. The sample's reflectance spectrum is then stored.

To conduct the transmission measurement, the shutter is removed without moving the sample and the reflection probe connection is replaced with the transmission probe connection. The integration time (10 to 30ms) and number of averaged scans are adjusted then the

sample's transmission spectrum is stored. The sample is removed and the transmission spectrum of air is stored.

A Python script was written that uses the four saved spectra to determine the reflectance (R) and transmission (T) of light from the sample with a value between 0 and 1 for each wavelength. The script also determines an approximate absorbance (A) as follows:

$$A = 1 - (T + R) \tag{2.6}$$
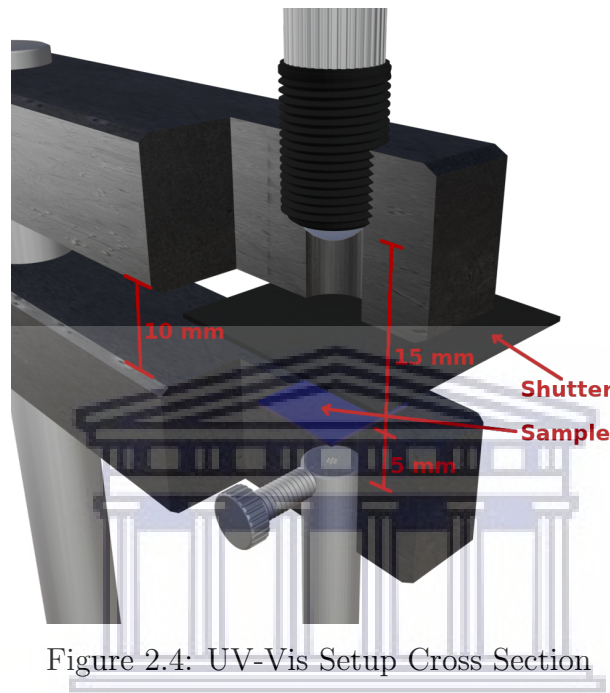
Figure 2.4: UV-Vis Setup Cross Section

Thin film interference can be used to easily determine the uniformity of a thin film, since interference fringes depend upon the thickness of the thin film and its refractive index as a function of wavelength. [73] Fig. 2.5(a) is an image of a spin-coated lead iodide, (b) is an image of white light projected trough the sample onto a white surface and (c) is an image of white light reflected from the surface of the thin film onto a white surface. This is to demonstrate the visual difference of constructive and destructive interference, where the UV-Vis measurements at the two different locations can be seen in fig. 2.6. The thicknesses at position S1 and S2 were 136 and 148nm respectively, which demonstrates the ease of which a person can determine the difference above 10 nm by simple visual inspection. This is only true for thin films with a low surface roughness. Samples with surface roughness above 20 nm are simply yellow in appearance due to a lack of thin film interference of visible light.
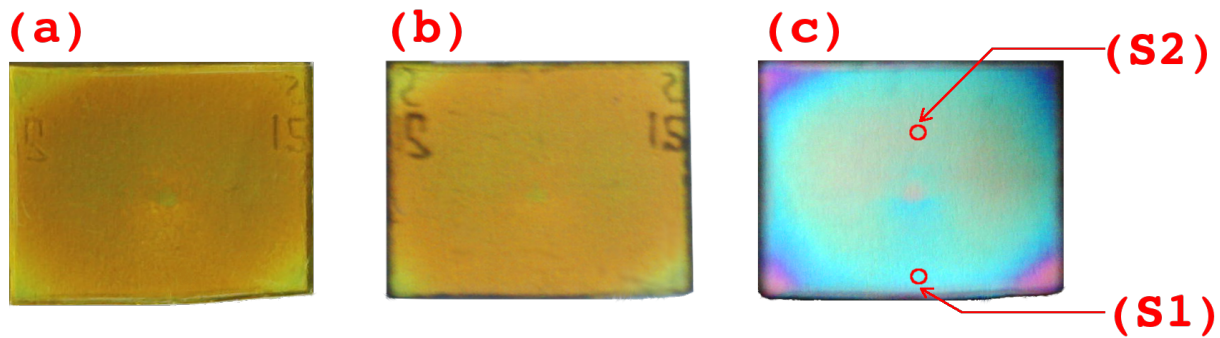
Figure 2.5: Spin-coated PbI$_2$ (a) Optical Image, (b) Projected Transmission, (c) Projected Reflection
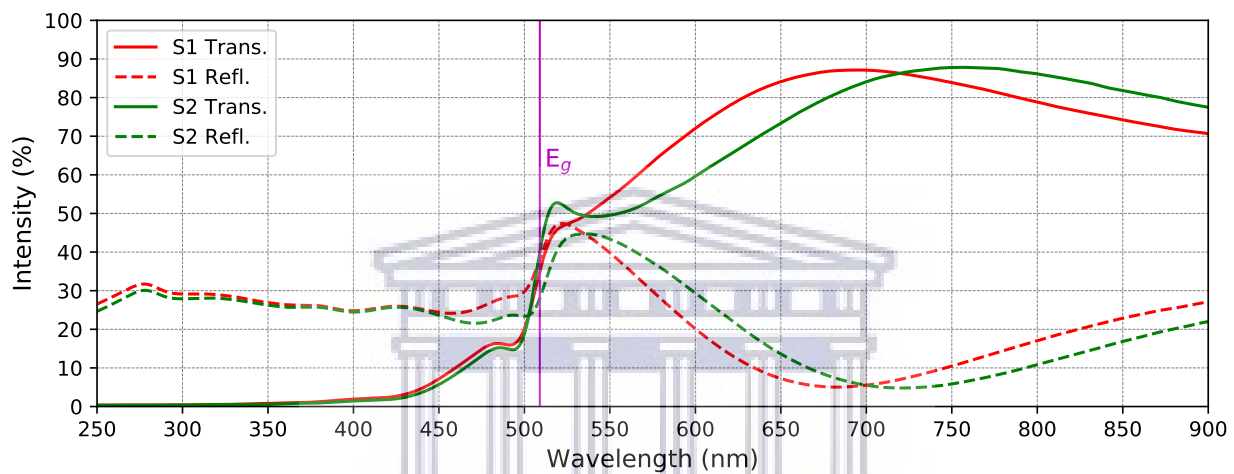
Figure 2.6: Specular Transmission and Reflection at position S1 and S2

2.3 Electron Microscopy

A widely used method to determine average grain size, is the Heyn linear intercept procedure. According to the ASTM E112-13 standard random lines with different orientations are used that intercepts at least 50 grains. The grain size is determined by dividing the length of the line by the number of intercepts and adding $\frac{1}{2}$ for the end points. The average is taken for several lines from 3 to 5 different regions on a sample.

Since the Heyn's procedure does not provide a distribution of grain sizes, a Python script (appendix D.1) was written that calculates the area of each grain and approximates the grain size with the diameter of a circle of equal area.

A commonly used software ImageJ can be used to automate the identification of grains. However, the perovskite grains are mostly smaller than one micron making it difficult to distinguish individual grains and the software is also best suited to identify loosely packed nanoparticles. An SEM image is simple a 2D matrix of data points with each point having a greyscale value between 0 for black and 255 for white, the higher the number the brighter the colour. The greyscale image is first converted to RGB, resulting in black pixels assigned an array value of (x, x, x) where x is the original intensity ranging from 0 to 255. The Python script is used to only identify pixels of either red (255, 0, 0), green (0, 255, 0) or blue

(0, 0, 255). The grains are therefore manually identified by tracing the grain boundaries in an image editing software with red, then identify each grain with a single pixel roughly in the centre of the grain with blue, similarly voids are also identified with green. The scale bar is used to calibrate the number of pixels per nanometre. Once the grains have been identified of sufficiently large area the Python script can be used to automatically calculate the grain size of each grain and also provide a distribution of grain sizes as well as the percentage of the area that contains voids.

To demonstrate the method a small section of an image is shown in fig. 2.7. Each grain is identified by the blue central pixel which provides an origin point. The grain boundary associated with the selected grain is identified by calculating the closest red pixel within a predefined arc (pink lines) and by rotating the arc region anti-clockwise an array of points are created (yellow pixels). The smaller the size of the arc the more pixels are identified. However, the size must not be set too small or pixels from further grains will be selected since there may not be any data points that lie within the small arc of the selected grain. The process is repeated for all grains and voids. The array of points for each grain form a polygon of which the area can be calculated with the shoelace formula equation 2.7 using the x and y coordinate of each pixel.[74]
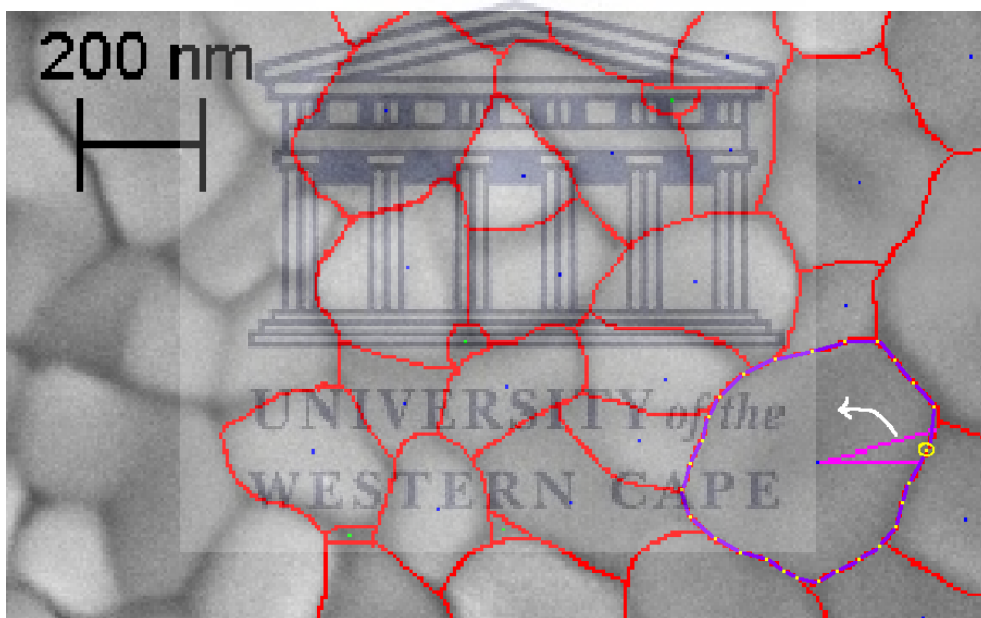
Figure 2.7: Area of Grains using Shoelace Method

$$area = \frac{1}{2} \sum_{i=1}^{n} \det \begin{pmatrix} x_i & x_{i+1} \\ y_i & y_{i+1} \end{pmatrix} \tag{2.7}$$

where $x_{n+1} = x_1$ and $y_{n+1} = y_1$

The shoelace formula can be written in a different form as seen in eq. 2.8 for implementation in Python. The absolute value is only necessary if the order of the array is clockwise which will result in a negative area. Since Python is a interpreted coding language it is important to minimize the use of for loops and instead do computations using the NumPy library which contains optimised algorithms written in C to increase computational speed. Eq.

2.8 is written below in Python code with the use of the NumPy dot product function (np.dot()).[75]

$$area = \frac{1}{2}\left|\sum_{i=1}^{n-1} x_i y_{i+1} + x_n y_1 - \sum_{i=1}^{n-1} y_i x_{i+1} - y_n x_1\right| \tag{2.8}$$

area = 0.5*(np.dot(x[:-1], y[1:]) + x[-1] * y[0] - np.dot(y[:-1], x[1:]) - y[-1] * x[0])

The thickness and roughness of a thin film can be determined from the cross-section SEM of a sample that has been broken in half exposing the internal structure of the thin film. The top surface of the thin film is traced as seen in fig. 2.8 ensuring that the substrate is aligned horizontally. Using the scale bar, the trace-line can be digitised to evaluate the average thickness and the roughness from the standard deviation in the height above the substrate.
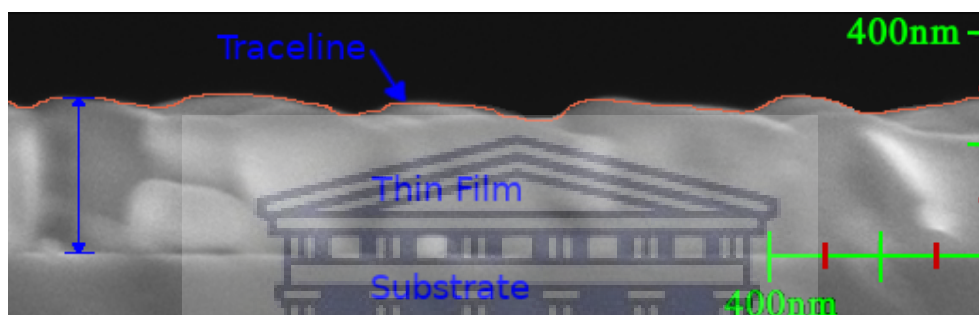
Figure 2.8: Thickness Calculation of a Thin Film from Cross-section SEM

2.4 Crystallography

Crystallography is the study of a solid material's structure, by determining the periodic arrangement of atoms that form a crystalline material. Solids can also be amorphous, with atoms randomly arranged within a material for example, glass. The most common technique will be used, X-ray diffraction analysis (XRD). A beam of X-rays with various wavelengths (λ) are generated by bombarding electrons into a target. The most intense being the characteristic x-rays, which form when the electrons within the target that were excited from the bombardment transition to a lower energy level. The target material used in this study is copper, which generate characteristic x-rays named $K\alpha_1$ and $K\alpha_2$ corresponding to wavelengths of 1.5405 and 1.5443Å respectively with $K\alpha_1$ being approximately twice as intense as $K\alpha_2$. When conducting a XRD measurement a beam of x-rays diffract from the atoms within a sample's crystal structure as seen in fig. 2.9. At certain angles (θ) that follow Bragg's law (eq. 2.9) the incoming beam will diffract from atoms within diffraction planes with spacing d, such that the diffracted x-rays constructively interfere forming an intense detectable signal. By precisely varying the angle between the beam and detector, a diffraction spectrum is recorded, which can be analysed to determine a sample's crystal structure.[76]

$$2d\sin\theta = n\lambda \quad (n = 1, 2, 3, ...) \tag{2.9}$$
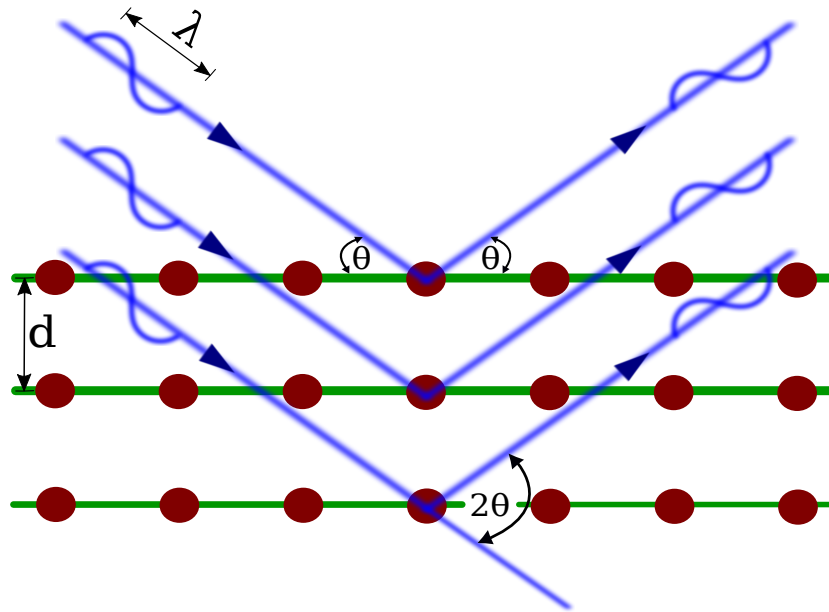
Figure 2.9: Bragg's Law Diagram

Since the x-ray beam consists predominately of two wavelengths, $K\alpha_1$ and $K\alpha_2$ which independently interference, the XRD spectrum is therefore a summation of diffraction peaks from each wavelength. At small diffraction angles (2θ) these two peaks will be nearly indistinguishable. However as the angle increases, the spacing between peaks also increases as described by eq. 2.10 derived from Bragg's law and seen in fig. 2.10.

$$\theta_2 = \sin^{-1}\left(\frac{\lambda_2}{\lambda_1}\sin\theta_1\right) \tag{2.10}$$
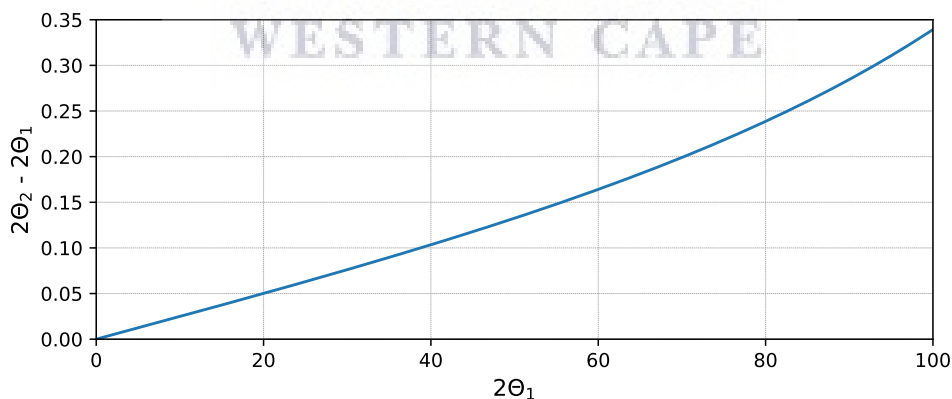
Figure 2.10: Peak Offset in Degrees

The periodic arrangement of atoms within a crystal is defined by a unit cell. The size and shape of the unit cell is described by three base vectors $\vec{a}$, $\vec{b}$ and $\vec{c}$, where the lengths (a, b and c) and angles (α, β, and γ) of these vectors form the lattice constants of a unit cell as seen in fig. 2.11. In order to completely define a crystal structure a space group must be

assigned as well as the position of the atoms within the unit cell. The position of an atom is described by a fractional coordinate (x, y and z) in respect to the vectors $\vec{a}$, $\vec{b}$ and $\vec{c}$. There is a total of 230 different space groups in three dimensions, which are grouped into seven different crystal systems: triclinic, monoclinic, orthorhombic, tetragonal, trigonal, hexagonal, and cubic. Each space group consists of a list of symmetry operations which transforms an atoms coordinates x, y and z to a symmetrically equivalent coordinate $\tilde{x}$, $\tilde{y}$ and $\tilde{z}$, where each unique coordinate describes the position of each atom with the crystal. Periodicity must also be taken into account for coordinates where x, y or z equals zero. Thus an atom at position $(0, 0, 0)$ infers a total of 8 atoms one at each corner of the unit cell. The symmetry operation consists of a rotational (W) and translational (w) component, written in matrix notation (eq. 2.11) which is combined into a single augmented matrix as seen in eq. 2.12. [77]
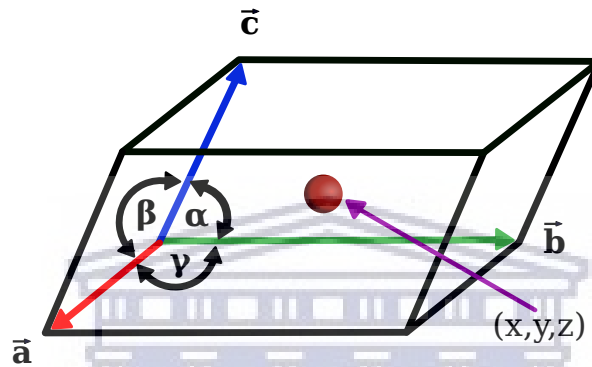
Figure 2.11: Crystal Unit Cell

$$\begin{bmatrix} \tilde{x} \\ \tilde{y} \\ \tilde{z} \end{bmatrix} = \begin{bmatrix} W_{11} & W_{12} & W_{13} \\ W_{21} & W_{22} & W_{23} \\ W_{31} & W_{32} & W_{33} \end{bmatrix} \begin{bmatrix} x \\ y \\ z \end{bmatrix} + \begin{bmatrix} w_1 \\ w_2 \\ w_3 \end{bmatrix} \tag{2.11}$$

$$\begin{bmatrix} \tilde{x} \\ \tilde{y} \\ \tilde{z} \\ 1 \end{bmatrix} = \begin{bmatrix} W_{11} & W_{12} & W_{13} & w_1 \\ W_{21} & W_{22} & W_{23} & w_2 \\ W_{31} & W_{32} & W_{33} & w_3 \\ 0 & 0 & 0 & 1 \end{bmatrix} \begin{bmatrix} x \\ y \\ z \\ 1 \end{bmatrix} \tag{2.12}$$

The symmetrically equivalent coordinates are generally listed in terms of x, y and z which can be written in terms of a augmented symmetry operation matrix for computation. For example, $\tilde{x}, \tilde{y}, \tilde{z} = x + \frac{1}{2}, -z, y - \frac{1}{4}$ is written as follows:

$$\begin{bmatrix} 1 & 0 & 0 & \frac{1}{2} \\ 0 & 0 & -1 & 0 \\ 0 & 1 & 0 & \frac{1}{4} \\ 0 & 0 & 0 & 1 \end{bmatrix}$$

As previously mentioned the diffraction peaks of an XRD spectrum depends upon the distance between parallel planes of atoms within a crystal structure known as the d-spacing. The orientation of these planes is defined by a set of Miller indices denoted (hkl) and are

determined from the reciprocal of the distance which a plane intercepts the base vectors of a unit cell, written as integers. All crystal structures in this work is either cubic, tetragonal, trigonal or orthorhombic. The d-spacing (d) is related to the Miller indices of a plane and the dimensions of the unit cell (a, b, c) as seen in equations 2.13a to 2.13d for the various crystal systems. The volume of each crystal system based on its lattice constants are also listed in equations 2.14a to 2.14d. By using the calculated volume of a crystal and the mass of the atoms within its unit cell the mass density (ρ) of a material can be estimated. [76]

$$\text{Cubic}: \quad \frac{1}{d^2} = \frac{h^2 + k^2 + l^2}{a^2} \tag{2.13a}$$

$$\text{Tetragonal}: \quad \frac{1}{d^2} = \frac{h^2 + k^2}{a^2} + \left(\frac{l}{c}\right)^2 \tag{2.13b}$$

$$\text{Trigonal}: \quad \frac{1}{d^2} = \frac{4}{3}\frac{h^2 + hk + k^2}{a^2} + \left(\frac{l}{c}\right)^2 \tag{2.13c}$$

$$\text{Orthorhombic}: \quad \frac{1}{d^2} = \left(\frac{h}{a}\right)^2 + \left(\frac{k}{b}\right)^2 + \left(\frac{l}{c}\right)^2 \tag{2.13d}$$
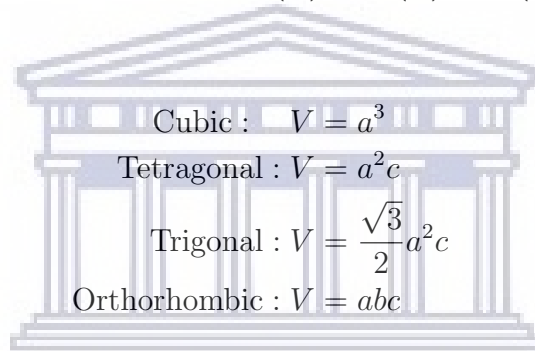
$$\text{Cubic}: \quad V = a^3 \tag{2.14a}$$

$$\text{Tetragonal}: V = a^2 c \tag{2.14b}$$

$$\text{Trigonal}: V = \frac{\sqrt{3}}{2}a^2 c \tag{2.14c}$$

$$\text{Orthorhombic}: V = abc \tag{2.14d}$$

A powder diffraction XRD system is used for all crystallography analysis in this work, which poses a problem when characterising thin films. Powder samples are made from large number of crystals that are randomly orientated, hence all theoretical peaks are detected. This is not always the case for thin films which can have a preferred orientation. For example, as seen in fig. 2.12 which demonstrated the unit cell of a lead iodide crystal (P-3m1 space group) in two different orientations with its first four diffraction planes (001), (100), (002) and (101). Lead Iodide crystals has a strong tendency to orientate parallel to a substrate forming alternating layers of lead and iodide as seen in the first image of fig. 2.12. Therefore powder diffraction of lead iodide typically only have peaks due to the (00l) planes.[78]

All images of crystal structures except fig. 1.6 was created using the Visualization for Electronic and STructrual Analysis (VESTA) software. This also includes the diffraction planes. [79] The arrows to the left of a crystal structure indicates the orientation of the unit cell. Crystal structures are obtained from the Crystallography Open Database (COD) using a crystallographic information file (CIF).[80]
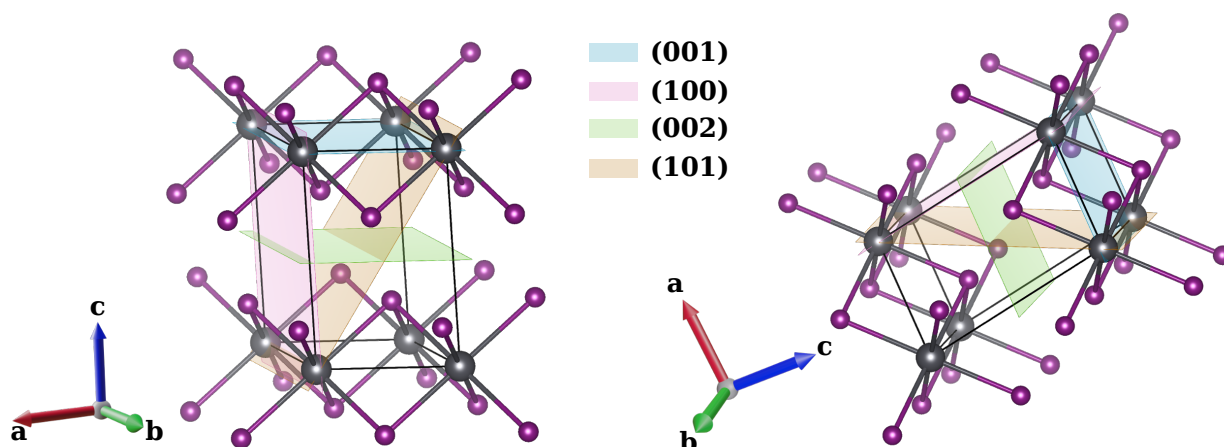
Figure 2.12: PbI$_2$ Unit Cell in Different Orientations

In order to more accurately determine the crystal structures within this study, the Rietveld refinement software GSAS-II is used. Rietveld refinement uses a known crystal structure for a material using a CIF to create a theoretical XRD spectrum. By using least square fitting of various parameters for example, the lattice parameters, crystal size, strain and instrumental broadening, the theoretical spectrum is adjusted to most closely match the experimental spectrum. [81]

A critical part of Rietveld refinement is insuring that the CIF is correct and closely matches a desired structure. Often different space groups can be used to describe the same crystal structure, with one being more accurate that the other depending on the specific crystalline material being studied. It is also important to use visualization software for example, VESTA to determine if there are any errors in a CIF for example, if the organic molecule in the perovskite structure was excluded. Certain space groups can have multiple origins of choice, which does not change the overall crystal structure, but only redefines the unit cell. GSAS-II requires the use of the second origin of choice which provides greater computational speed in calculating an XRD spectrum.[82] For example, the unit cell of silicon using space group 227, Fd-3m, can be constructed from a single atom's position and the symmetry operations of the space group. However the position of the silicon atom using origin 1 is (0, 0, 0) and origin 2 is (0.125, 0.125, 0.125).
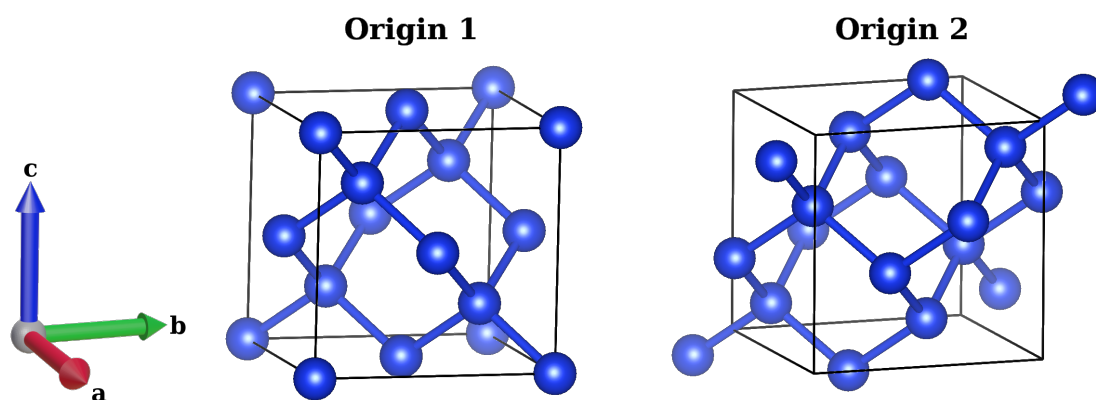
Figure 2.13: Different Origin of Choice of Silicon Fd-3m

The crystal size is a commonly calculated parameter in crystallography, with larger crystal sizes being preferred, which results in less defects within a material. For a solar cell absorber material having less defects relates to fewer recombination sites, thus providing a higher PCE. A common technique is using the Scherrer equation (eq. 2.15), which relates the full with at half maximum (FWHM or β) of a diffraction peak to its crystal size (τ) where K is a dimensionless shape factor typically having a value 0.9 and θ is the Bragg diffraction angle. The width of a diffraction peak is thus inversely proportional to crystal size. However this technique is only suited for small crystal sizes ($< 1 \ \mu m$). [76]

$$\tau = \frac{K\lambda}{\beta\cos\theta} \tag{2.15}$$

In order to simulate individual diffraction peaks the GSAS-II software uses a Pseudo-Voigt function which is a linear combination of the Gaussian, G(x) and Lorentzian, L(x) functions as seen in fig. 2.14, where the position of the peak (μ) equals zero and the width of the two peaks are adjusted by the σ and Γ values which in this case is set to $\sqrt{\frac{1}{2\pi}}$ and $\frac{2}{\pi}$ respectively to have a maximum value of one. [81][83]

$$G(x) = \frac{1}{\sigma\sqrt{2\pi}}e^{-\frac{1}{2}((x-\mu)/\sigma)^2} \tag{2.16a}$$

$$L(x) = \frac{1}{2\pi}\frac{\Gamma}{(x-\mu)^2 + (\frac{1}{2}\Gamma)^2} \tag{2.16b}$$
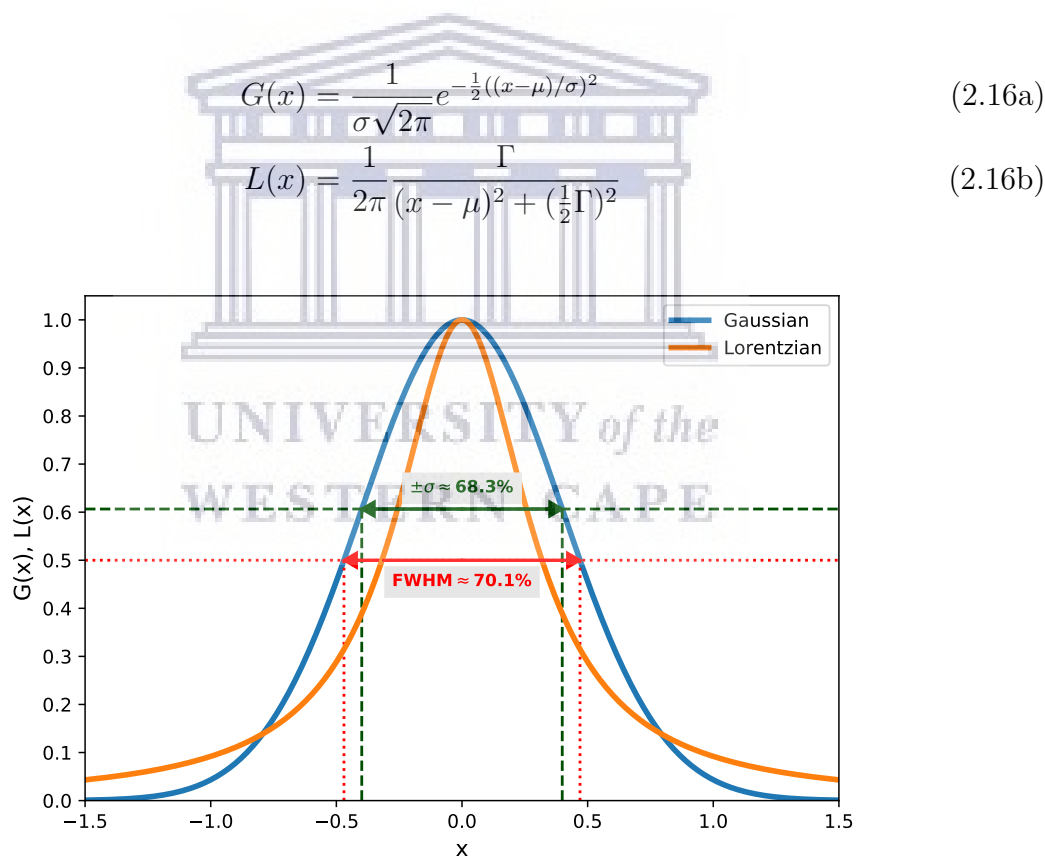
Figure 2.14: Diffraction Peak Distribution

The crystals within a material can be under different forms of strain (ϵ) which will have a different effect on the XRD peaks. Uniform strain results in a shift in the diffraction peak with tensile strain causing the diffraction peak to occur at a smaller 2θ and compression strain will have the opposite affect. When the crystal has a non-uniform strain where certain regions are under tension and others compression, this results in several diffraction

peaks and an overall broadening of the measured diffraction peak. Strain is described as $\epsilon = \frac{\Delta D}{D}$ and commonly expressed in terms of microstrain, due to the small change in the d-spacing.[76] The strain within the perovskite structure can be caused by defects for example, iodide vacancies due to incomplete perovskite formation resulting in recombination centres.[84]
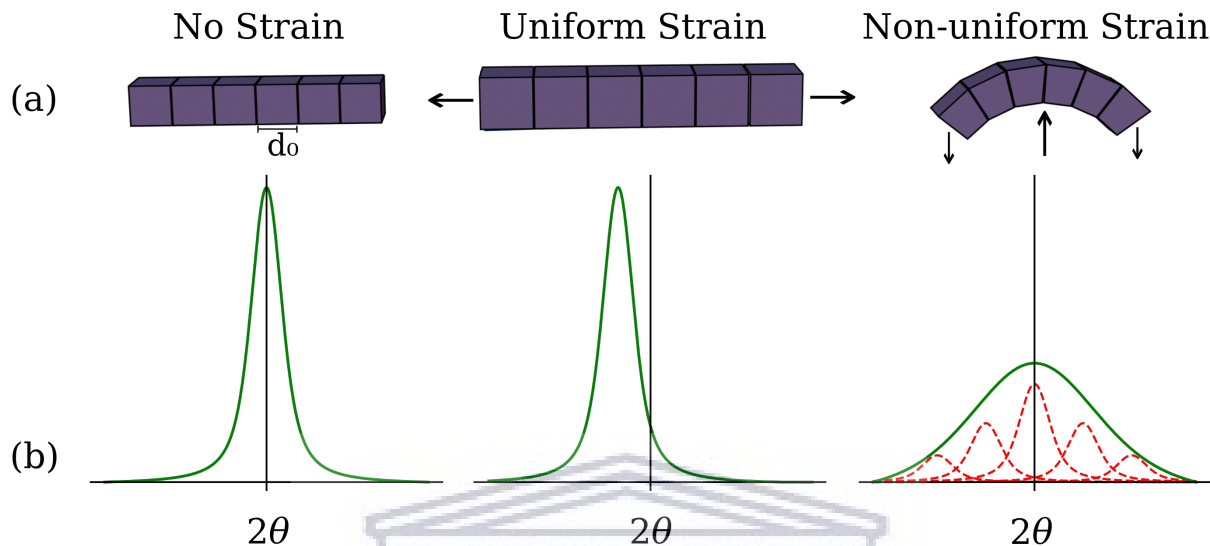
Figure 2.15: Effect of (a) Crystal Lattice Strain on (b) Diffraction Peak

The GSAS-II software can also provide information on the amount of preferred orientation within a measured sample using either the March-Dollase or spherical harmonics function. For all Rietveld refinement in this study the spherical harmonics function with a harmonic order of 10 was used which provides a texture index. The larger the texture index the greater degree of preferred orientation there is within a material with the lowest value of one indicating a material with no preferred orientation.[82]

Each XRD powder diffraction system requires calibration in order to determine the amount of instrumental broadening and if there is any sample displacement which causes a shift in the diffraction peaks. Several different compounds can be used for calibration including the 640d silicon powder standard, which has a lattice constant, a of 5.43123 *pm* 0.00008 Å and an average particle size of 4 μm, created from milling a pure silicon crystal. [85] To closely mimic this standard a (100) silicon wafer was crushed into a powder. The best Rietveld fit as seen in fig. 2.16 had an Rw value of 9.45% and a goodness of fit (GOF) of 1.87 using the same lattice constant as the 640d standard. The background refinement used the Chebyschev-1 function which is also used in all other refinements in this study to remove the background of the XRD spectra. The calibration provided the following instrumental parameters: U = -37.2, V = -11.1, W = 4.23, X = 2.81, Y = 2.59 which are used to adjust the default shape of the simulated diffraction peaks. The sample displacement was -38 μm which caused the (111) peak to shift 0.02 degrees to the right as seen in fig. 2.17 which also includes a simulated (111) peak without sample displacement, instrumental broadening and a higher resolution with the individual $K\alpha_1$ and $K\alpha_2$ peaks.
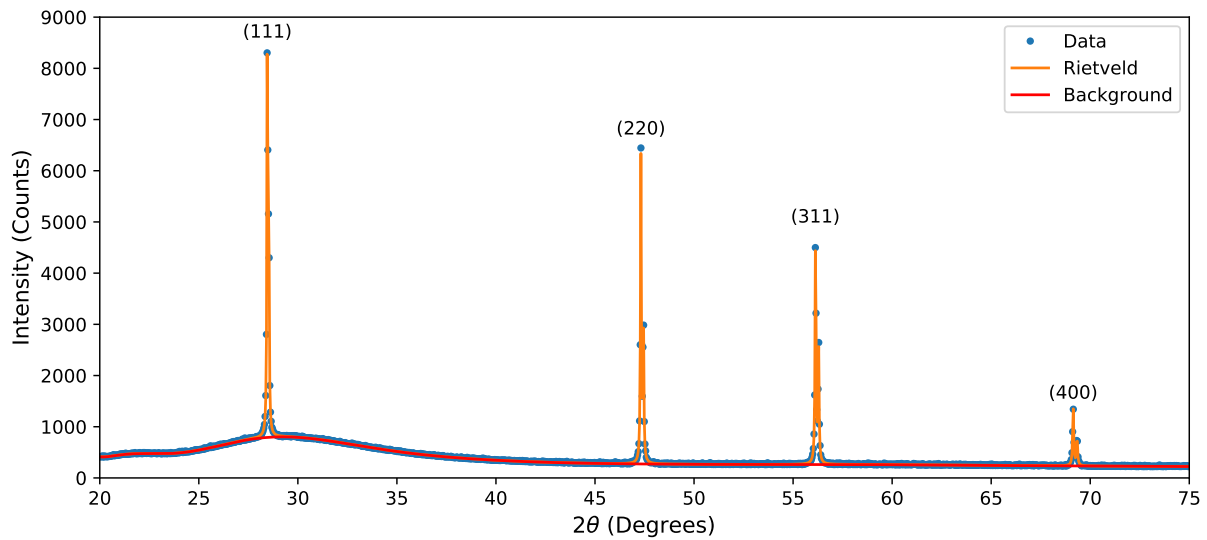
Figure 2.16: XRD Analysis of Si Powder
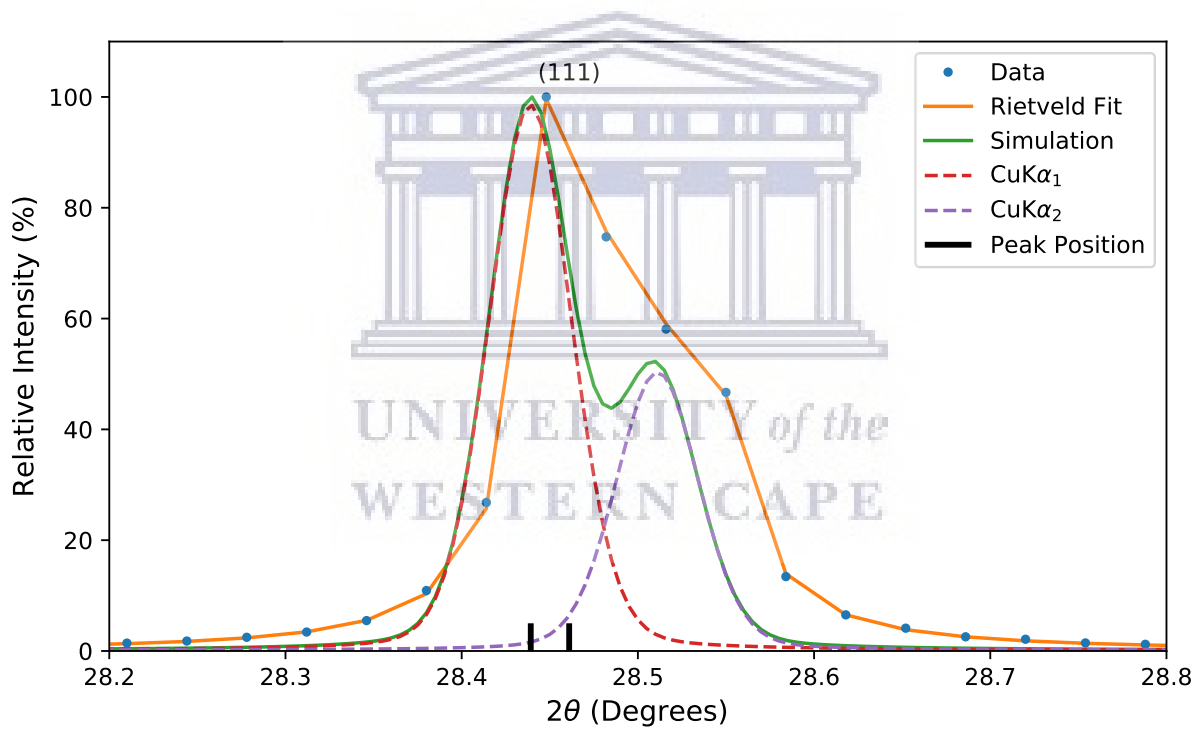
Figure 2.17: XRD analysis of Si (111) Peak

33

2.5 Rutherford Backscatter Spectrometry

Rutherford backscattering spectrometry (RBS) is an analytical technique used to determine the depth profile, stoichiometry, elemental area density and impurities of a sample. The technique is limited to a maximum thickness of a few microns with the use of He ions, thus only suitable for near surface analysis of bulk samples or thin films.[86]

RBS analysis uses accelerated ions (^{4}He$^+$ in this study) to probe the elemental composition as function of depth within a thin film, by evaluating the energy of the recoiled ions that reach a detector at a specific scattering angle. The initial kinetic energy of the ions (E_0) are precisely calibrated to allow a steady beam of incident ions with known energy. The incident ion can elastically scatter when colliding with the stationary target nuclei of the thin film. Since each isotope has a different mass M_2 the collision of the ion (mass = M_1) with the stationary target atom will result in a transfer of specific amount of energy as the particle is scattered at a certain angle (θ). The reduced energy (E_1) of the ion is due to an elastic collision and by conservation of momentum and energy the kinematic factor (K)is as follows [86]:

$$K = \frac{E_1}{E_0} = \left[\frac{(M_2^2 - M_1^2 \sin^2 \theta)^{1/2} + M_1 \cos \theta}{M_2 + M_1} \right]^2 \tag{2.17}$$

The probability of a collision depends on the differential cross-section as follows where Z_1 and Z_2 are the atomic number of the incident and target nuclei:

$$\frac{d\sigma}{d\Omega} = \left(\frac{Z_1 Z_2 q^2}{4E} \right)^2 \frac{4}{\sin^4 \theta} \frac{((1 - ((M_1/M_2) \sin \theta)^2)^{0.5} + \cos \theta)^2}{(1 - ((M_1/M_2) \sin \theta)^2)^{0.5}} \tag{2.18}$$

The incident positively charged ion loses energy as it travels through the thin film which results in an energy-loss rate dE/dx dependent on nuclear (n) and electronic (e) collisions:

$$\frac{dE}{dx} = \frac{dE}{dx}\bigg|_n + \frac{dE}{dx}\bigg|_e \tag{2.19}$$

The detector in the RBS set-up is placed at a fixed angle thus the highest detected energy will be E_1 of the scattered particle with the surface of the target material. The thickness of a sample is extracted by the width of the peak as the energy of the particle decreases as it travels through the target material until it scatters from a collision with a target nucleus. The amount of energy loss through the thin film depends on the composition of the target layer, the distance travelled and kinetic energy of the incident ion. [86]

The experimental results of thickness by RBS is determined as the number of atoms per cm^2 (# atoms) known as the areal density, in order to convert to standard metric units of thickness the molar mass (m_i) and fraction (f_i) of the constituent elements of the compound as well as the density (ρ) of the compound must be known to determine the linear thickness as follows:

$$\text{thickness} = \frac{\#atoms \times \sum_i m_i f_i}{N_A \times \rho} \tag{2.20}$$

Samples are analysed using the Simnra software by simulating a RBS spectrum based on input elemental composition and the areal density (10^{15} atoms/cm^2). The more information

that is known prior to analysis the closer the initial estimation can be to the correct composition and areal density, which can be further optimised by least square fitting to closely match an experimental spectrum. [87] Depth profiling is performed by separating a thin film into multiple layers where the areal densities can be varied for each layer. Using multiple layers are only necessary when there is a non-uniform elemental composition within a thin film.

Before analysing experimental data, the simulation setup must be calibrated with a known standard. The standard used for calibration consisted of 3 layers, a silicon substrate, SiO_2 oxide layer and a thin film consisting of a mixture of gold and cobalt (fig. 2.18). The $^4He^+$ ion beam intensity was reduced from the conventional 100 nA to 10 nA to minimize damage to the perovskite thin films with a total collected charge for each sample of 20 μC and beam energy of 3045 keV. The samples were positioned with a 5° tilt and the detector (30 keV resolution) was positioned to provide a scattering angle of 150°.

The energy calibration was determined to be E = $-10^{-4}x^2 + 3.0876x + 127.1$ were x is the channel number and the particle number was $3.83\text{x}10^{10}$. The initial energy calibration is done by using the kinematic factor of each element of the standard then further fitting is done to determine the composition and areal density Since the silicon is a substrate an arbitrary large areal density of 100 000 was used, the SiO_2 layer was 2065 with a composition of 33.8% silicon and 66.2% oxygen with a calculated thickness of 300 nm (2.3g/cm³). The top layer consisted of 77.5% cobalt and 22.5% gold with a areal density of 9.4 which equates to a thickness between 1 and 2 nm depending on its density. The kinematic factor and natural abundance[88] of each isotope of the elements that was studied with RBS can be seen in table 2.1.
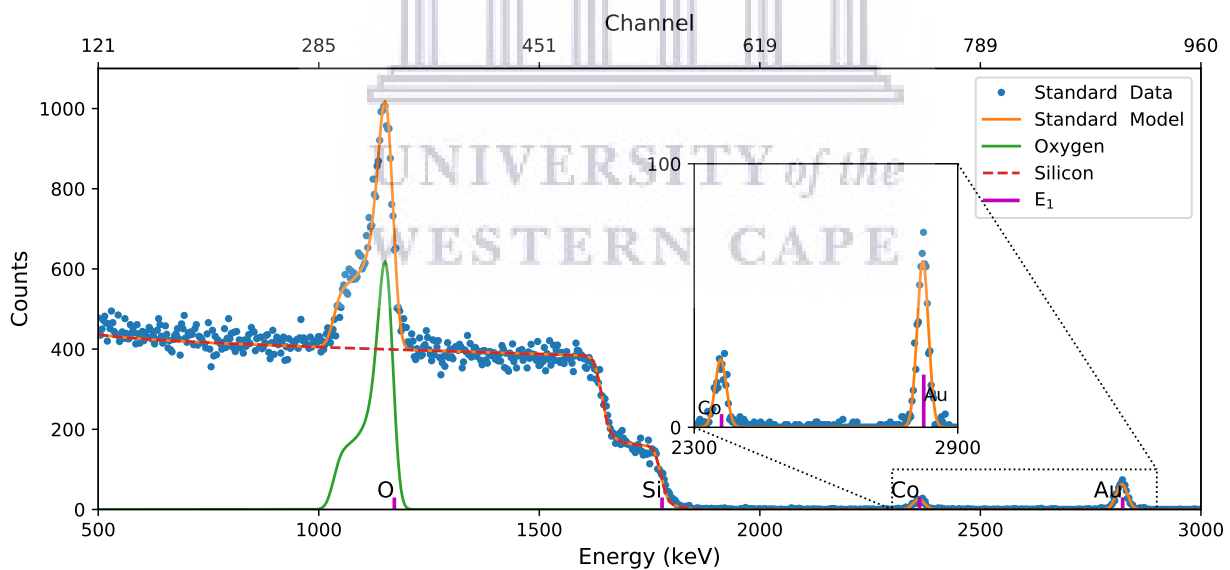
Figure 2.18: RBS Standard for Energy Calibration

Table 2.1: RBS Isotopes

Isotope	K	E1 (keV)	Abundance (%)
208Pb	0.9307	2834	52.4
207Pb	0.9304	2833	22.1
206Pb	0.9300	2832	24.1
204Pb	0.9294	2830	1.4
197Au	0.9270	2823	100
127I	0.8889	2707	100
59Co	0.7758	2362	100
37Cl	0.6665	2029	24.22
35Cl	0.6511	1982	75.78
30Si	0.6056	1844	3.09
29Si	0.5951	1812	4.68
28Si	0.5840	1778	92.23
18O	0.4296	1308	0.21
17O	0.4080	1242	0.04
16O	0.3847	1171	99.76
15N	0.3599	1096	0.37
14N	0.3332	1014	99.63
13C	0.3044	927	1.07
12C	0.2733	832	98.93

2.6   Solar Cell Characterization

Solar cell characterization primarily requires four components, an AM1.5 solar simulator, a light meter or reference cell, source measure unit (SMU) and an apparatus to connect the solar cell to the SMU. For more details on the measuring apparatus and solar cell design see chapter 4.1.

The solar simulator that was used is the Sciencetech sf150-27049 xenon lamp with a AM1.5 filter. A concern with the light source is that it was prone to fluctuate in intensity. To evaluate the variation in intensity the UV-Vis spectrometer was used to measure the intensity for one minute with the output power of the simulator set to 50, 100 and 150 watts. An integration time of 5 ms was used and the height of the probe was adjusted to ensure that each power setting resulted in the same maximum counts of 50 000. The spectrum between 200 and 1050 nm was integrated for each 5 ms integration measurement. The fractional intensity seen in fig. 2.19 is the fraction of intensity to the average intensity, the light source of the UV-VIS system labelled "Deuterium + Halogen" had also been included as a comparison. There was a significant amount of fluctuations at 50W with a periodic flicker of the light source between 90 and 120% of the average intensity, which would result in the current density of solar cell measurements to fluctuate by a similar amount. From table 2.2 the coefficient of variation (CV) is proportional to the power. The most stable setting of the simulator was at its maximum current of 150W which had a CV of similar magnitude of the UV-Vis light source.
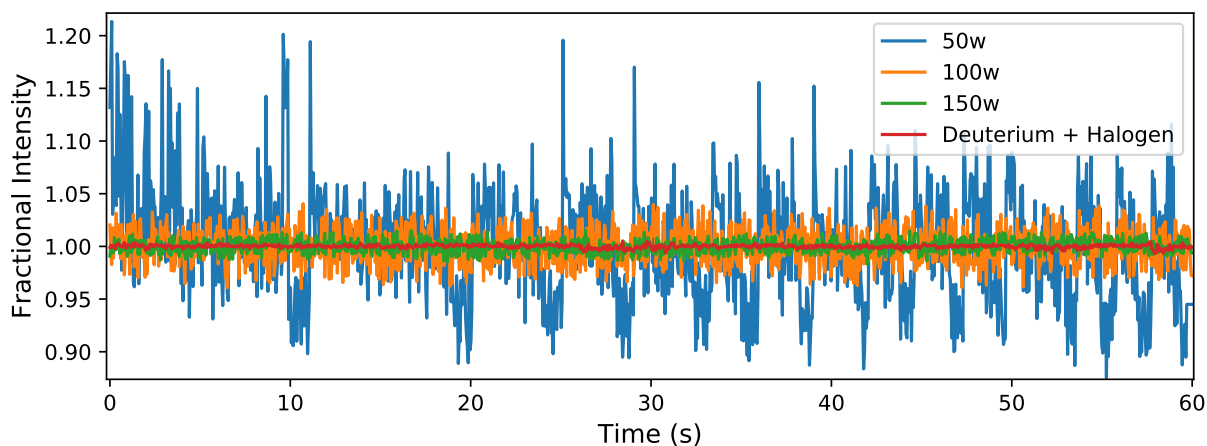
Figure 2.19: Fractional Light Intensity over Time

Table 2.2: Efficiency Progression Performance

Light Source	SNR	CV
50W Xenon	18.8	0.0532
100W Xenon	57.5	0.0174
150W Xenon	156	0.00643
Deuterium + Halogen	653	0.00153

A Daystar solar meter was used, with a precision of 1 W/m^2. The detector area was larger than the solar simulator which would result in large over estimations of the light intensity, therefore 75% of the area of the detector was masked. Thus the measured intensity is multiplied by four to provide more accurate measurements with some reduction in precision.

The SMU used was the Keithley 2420, which only had rudimentary data acquisition and analysis software for solar cells, therefore as part of this MSc. specialised software was written to allow fast data acquisition and automated data analysis, with single diode model fitting. The software relies on Qt5 for the graphical user interface (GUI) with all code written in Python 3. The Standard Commands for Programmable Instruments (SCPI) are used to communicate with the SMU via Virtual Instrument Software Architecture (VISA).[89]

The primary purpose of the SMU is to test the solar cell under a variable load by sweeping between a range of voltages, to produce a JV-curve. The script to perform the voltage sweep can be seen in appendix D.2.

The solar cell software GUI can be seen in fig. 2.20 (a), (b), (d) and (e) are the four tabs in the main interface and (c) and (f) are data plots in separate windows utilising the Matplotlib library. Each solar cell sample consists of several individual cells, the software stores all data in one folder which is created when the settings are saved which creates a csv file of all the settings. Data that has already been acquired can easily be loaded into the software to re-evaluate results. The setting include the voltage range with number of data points, whether hysteresis must be performed. Since the Keithley 2420 had 4-wire sensing this option had also been added. Another important factor for perovskite solar cells is the scan rate which can be adjusted by the number of power line cycles (NPLC) and delay in ms

between individual data point. The NPLC ranges between 0.01 and 10 with higher values equating to longer noise integration time for more accurate and precise measurements.[89] Before performing a individual measurement the SMU will apply a constant voltage for the duration of the delay before performing the measurement. The scan rate can be determined by pressing the "Scan Rate" button one the NPLC and Delay has been set. The software can also perform multiple measurements per cell with a pause between measurements, each individual measurement is automatically stored. However, the average is used for analysis with the standard deviation for each data point plotted with error bars in the JV-curve.

Window (b) allows the measurements of individual cells. All data is automatically stored in a separate folder for each intensity with the dark intensity set as default when starting the measurements. Any intensity value can be entered and added to the drop-down box which displays the current intensity. To perform a measurement the red button is pressed which sends the SCPI command to the SMU, once the measurement is completed the button's colour changes to green and window (c) opens displaying the JV-curve with the maximum point automatically calculated and plotted on the curve. The basic results are also plotted for the current cell. By checking the box for "Bias Voltage" a constant voltage is applied for a desired voltage for an example, a value of zero can be used to perform a stabilised measurement of the Jsc or the maximum point voltage can be used to acquire a stabilized PCE. The "Find Voc" option applies a bias current of zero amps which allows the determination of the stabilised Voc, which is more accurate then sweeping either in the forward or reverse direction and calculating the Voc from the intercept of the curve. Both the "Bias voltage" and "Find Voc" measurements can be adjusted by setting the interval between measurements, the duration to complete all measurements and also the NPLC.

Window (d) displays the full list of results of each cell, where the intensity and scan direction can be selected from the drop-down boxes. For a complete description of each results parameter see chapter 1.1.

Window (e) is used to perform single diode model fitting with the use of non-linear least square fitting using equation 1.2d. Five parameters are adjusted to optimize the fit which are J_0, J_{ph}, R_s, R_{sh} and n. Each parameter is bounded by an adjustable minimum and maximum value. The voltage region can also be adjusted to improve fitting in the region of interest. The data points and fit are viewed in window (f) which also displays the χ^2 value. The data and analysis seen in fig. 2.20 has been generated from eq. 1.2d.

(a)

(b)

(c)

(d)

(e)

(f)
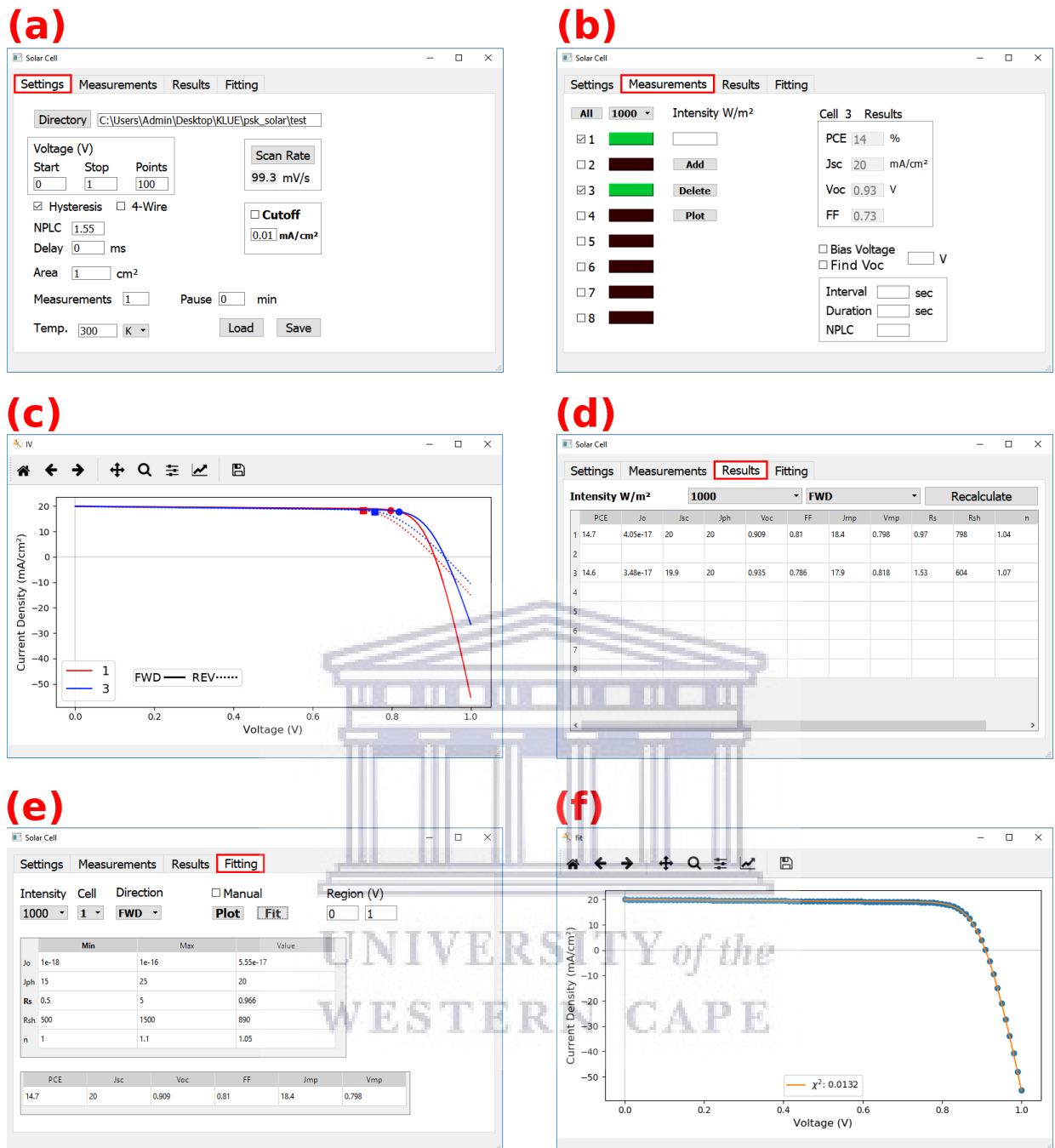
Figure 2.20: Solar Cell Software

Chapter 3

Optimization of CVD Perovskite

The procedure to obtain the ideal parameters for CVD deposition will be discussed in this chapter. The first section consists of the experimental setup, with all the necessary components and the general procedure of performing a CVD experiment, which includes the temperature profiling of the furnace. The second section focuses on the optimization of the lead halide deposition to ensure uniform and repeatable samples. The final section examines the conversion process by evaluating different lead halide precursor thin films.

3.1   Experimental Setup

The main component of the CVD setup is the tube furnace (Brother XD-1600MT) that consists of 3 heating zones with a length of 20 cm, as seen in fig. 3.1(b) The tubes used for all experiments were 6 cm in diameter. However, the furnace can be used with a 7 cm tube as seen in fig. 3.1 (a). The furnace has an external thermocouple for each zone for temperature control which is 1.5 cm from the tube wall. Additionally, three k-type thermocouples were used as internal temperature sensors that can be used under vacuum and used interchangeably with the external probes for higher accuracy.

The CVD setup also includes a pressurised N_2 gas supply with a mass flow controller (MKS type 1179) to regulate the flow between 10 and 1000 SCCM. The system can also be operated under vacuum with the use of a rotary vane pump (Leroy-Somer) that can reach a base pressure of 10^{-2} mbar. The pressure can also be regulated between 0.1 and 1013 mbar (1 Atm) with the use of a MKS 600 pressure controller.

The basic experimental setup can be seen in fig.3.2, the zone on the left is used to heat the source to a desired evaporation temperature, which is a powder placed in a ceramic crucible with surface area of 7 cm^2. The tube is pumped to base pressure to remove most oxygen and purged with a high flow of N_2. The working pressure is proportional to the flow rate of the N_2 carrier gas thus is kept constant throughout the experiment, except for the purging at the start and end of experiments. The N_2 carrier gas is inert and allows the evaporated source to be flowed downstream. Experiments can be performed without a carrier gas, since thermodynamic the gas will move from the hot to colder regions of the tube where it can be deposited, which leads to a fairly equal amount of source to be deposited on both ends of the tube, if the source is placed in the centre of the furnace.

The other zone is used to control the substrate temperature, which is separated by 4 cm

of insulation from the source. To improve thickness uniformity the samples must be tilted to a specific angle, since the thickness decreases downstream.[90] The samples are placed onto a custom made aluminium substrate holder that can provide a variable tilt angle. The aluminium holder is not ideal and only suitable for substrate temperatures below 200°C. The internal thermocouple is attached to the bottom of the holder directly below the samples. The samples attached to a glass sheet with Kapton tape, as well as two strips of glass to mask the edges of the TCO electrodes. Kapton tape is not placed on the surface since the silicone adhesive can evaporate contaminating samples.
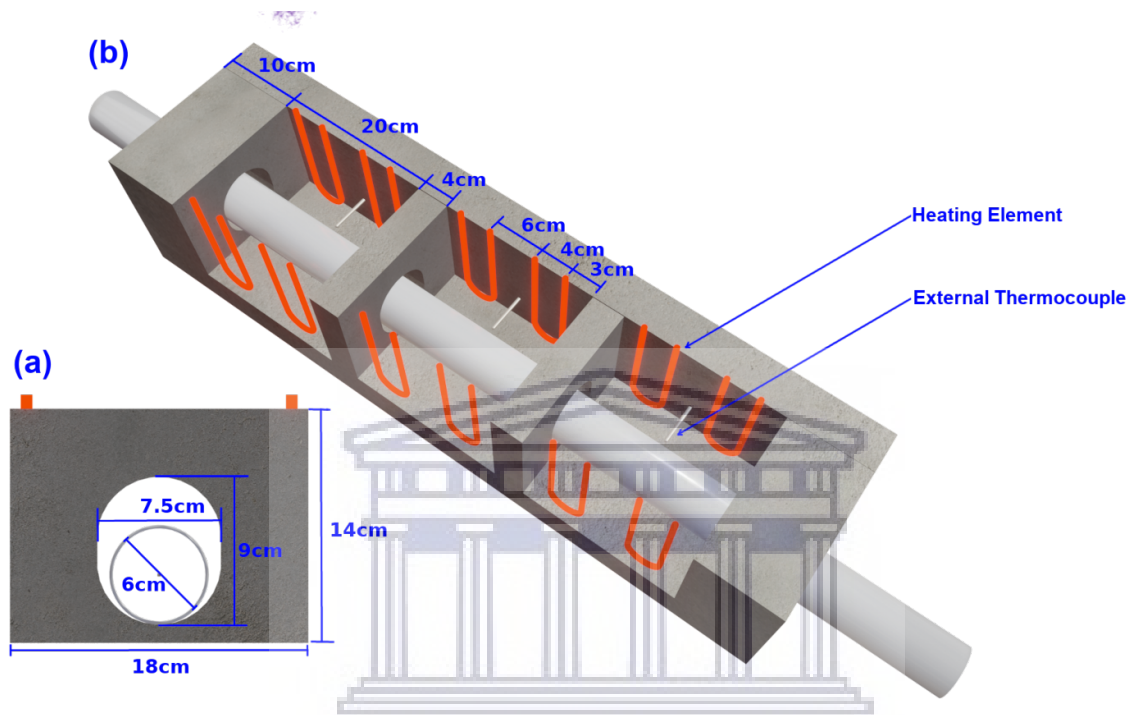
Figure 3.1: CVD Tube Furnace

Figure 3.2: CVD Experimental Setup

The temperature profile of the furnace forms an integral part in the CVD process, which is primarily dictated by the design of the furnace. Each 20cm zone of the furnace is separated

by 4 cm of insulation indicated in fig. 3.3 by the shaded area. The profiling was done by two k-type thermocouples simultaneously, separated by 10 cm to minimize the measuring duration, since the temperature increases over time. The position at 0 cm refers to middle of the zone that is heated, while the two adjacent zones are not heated. The aim was to identify the minimum temperature at various position from the source. A quartz tube with a 60 cm diameter and 2 mm wall thickness was used at atmospheric pressure with the ends of the tube covered, while still allowing the thermocouples to be adjusted. The furnace was heated at a rate of 10°C/min. to the desired temperature of 200, 300 and 400°C with the first thermocouple at -4 cm and the second at 10 cm. The thermocouples were shifted each minute by 1 cm until the centre of the adjacent zone at 24 cm was reached. The furnace was programmed to dwell at the desired temperature for 20 minutes before continuing to increase the temperature. Fig. 3.3 demonstrates the percentage of the set temperature as a function of position. Each set temperature had a similar profile, with a large reduction in temperature at the insulation as expected.

The temperature profile is merely a guide, since the profiling could not have been done under vacuum. However, the temperatures are in good agreement with experiments at low pressure (1-4 mbar). With the source at 400°C and no heating at the substrate during lead halide depositions the centre of the adjacent zone with the thermocouple attached to the sample holder first reaches a temperature between 85 and 90°C then increases to a maximum of 140°C after 20 minutes, with the rate of temperature increase gradually decreasing over time.
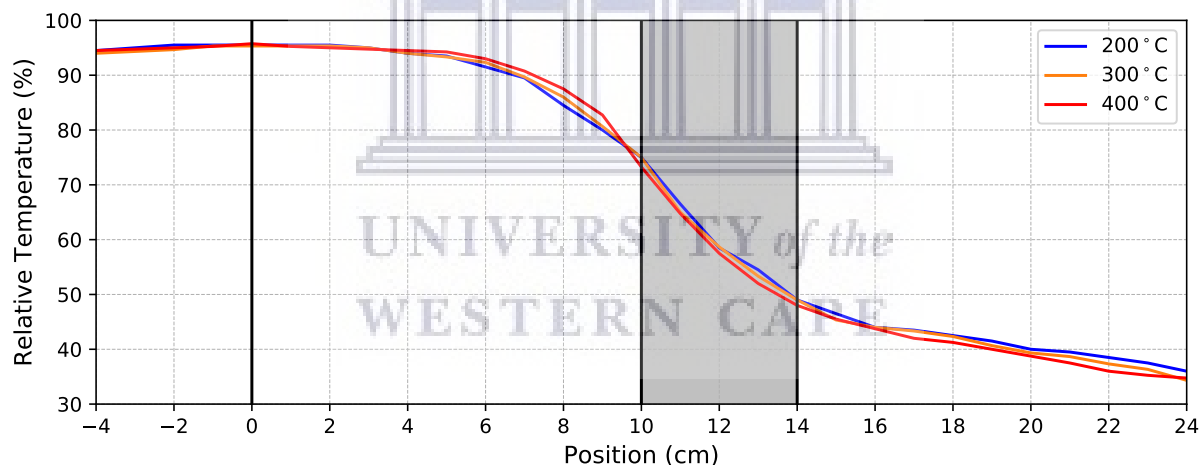
Figure 3.3: Temperature Profile of Tube Furnace

3.2 Vapour Deposition Optimization

The perovskite can be formed by simultaneously combining the lead halide with MAI, which is referred to as co-evaporation, typically performed in a PVD system in order to accurately heat both source materials independently and control the stoichiometry of the thin film with separate sensors. A sequential deposition is better suited for CVD since it allows significantly easier control, where a known thickness lead halide thin film can be exposed to MAI vapour, gradually forming the perovskite structure. In the sequential method the lead halide layer is generally deposited by either spin-coating or PVD.[91]

One of the aims of the study was to use the same tube furnace to deposit the lead halide as well as perform the perovskite conversion. Since the CVD system does not have a thickness monitor the optimization of a repeatable deposition method proved to be time-consuming. The major reason is that each parameter can't be adjusted independently, for example if the source temperature is increased to have a higher evaporation rate then the substrate temperature will also increase, affecting the quality of the thin film. Another concern is that an increase in flow rate results in an increased pressure which reduces the evaporation rate.

Most of the initial optimization was done with the substrates placed vertically in the tube 12 cm from the source, in order to obtain the highest yield and largest uniform area. This yielded good uniformity over an area of 4 cm^2 with thickness variations below 5%. However, due to the high yield thickness control was poor, since a small fluctuation in the amount of source used (< 1 mg) leads to thickness differences greater than 10 nm. Since the substrate is also close to the source the substrate temperature varies depending on the type of tube used and its wall thickness, meaning results were not repeatable for different tubes.

As seen in fig. 3.4, the thickness of PbI$_2$ decreases downstream, with alternating orange and green bands of similar thickness, due to thin film interference. Increasing the flow rate leads to thicker and more uniform samples. By placing the samples at the centre of the adjacent zone in the furnace repeatability of experiments could be improved. The flow rate was increased to 500 SCCM to ensure an adequate yield and more uniform thickness.

The optimum tilt angle was obtained by varying the angle from 20° to 35° in increments of 5°, with the most uniform samples obtained at 30°. The most repeatable results are obtained by controlling a deposition with a fixed amount of source material. Even though the thickness does vary with position the required tilt angle for uniform samples also vary with position since the change in thicknesses is not linear. Therefore, the closer the samples are to the source the steeper the required angle, limiting the usable area which is restricted by the tube diameter.
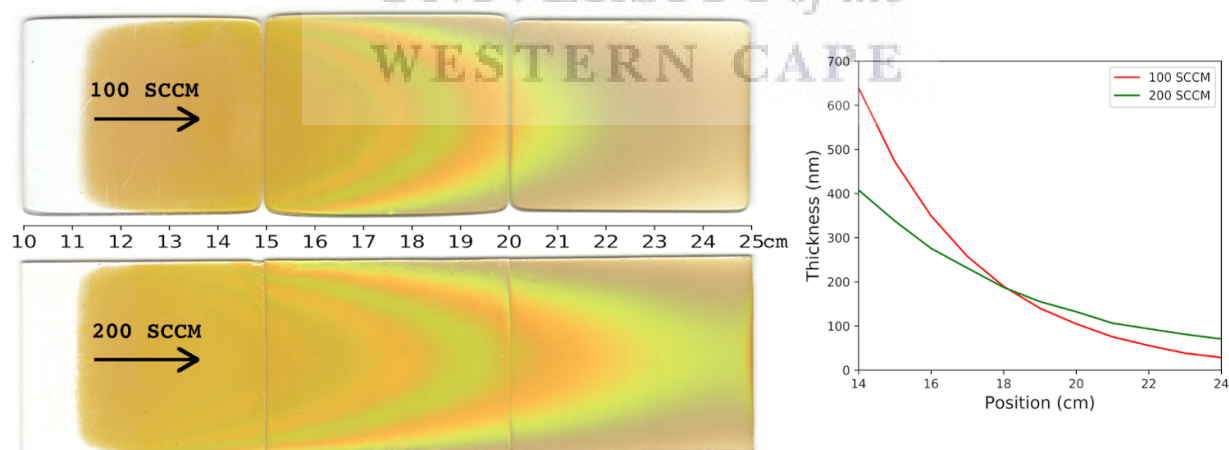
Figure 3.4: Thickness of CVD Lead Iodide with Different Flow Rates

Once the ideal parameters was identified the uniformity and repeatability of the CVD depositions were evaluated by repeating the same deposition on a 4x6 cm glass substrate as seen in figure 3.5. The source is heated to 380°C at 10°C/min then kept at 380°C for 15 min. to evaporated all 35 mg of PbI$_2$ powder. The N$_2$ flow rate is kept constant at

500 SCCM also during ramping providing a working pressure of 4 mbar. The substrate is placed in the centre of the second zone 24 cm from the source with a 30° tilt. The fractional thickness was measured of each sample along the width and length in relation to the thickness at the position marked in fig. 3.5 which for the three samples were 139, 142 and 146 nm. The average of the three experiments can be seen in figures 3.6 and 3.7 indicating a 5.1 cm^2 area that has a thickness variation of 5% which were obtained by polynomial interpolation of the measurements.
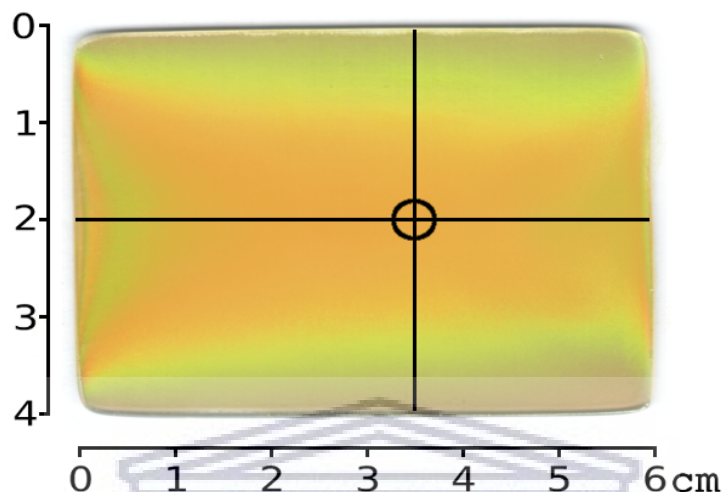
Figure 3.5: Optical Image of CVD lead Iodide Deposition
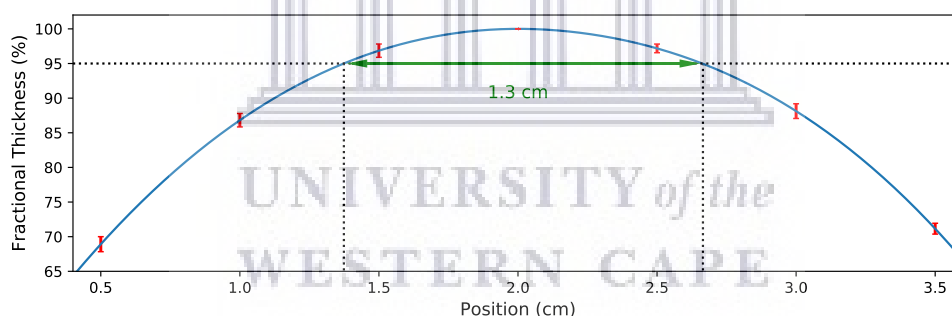
Figure 3.6: Fractional Thickness of Sample's Width
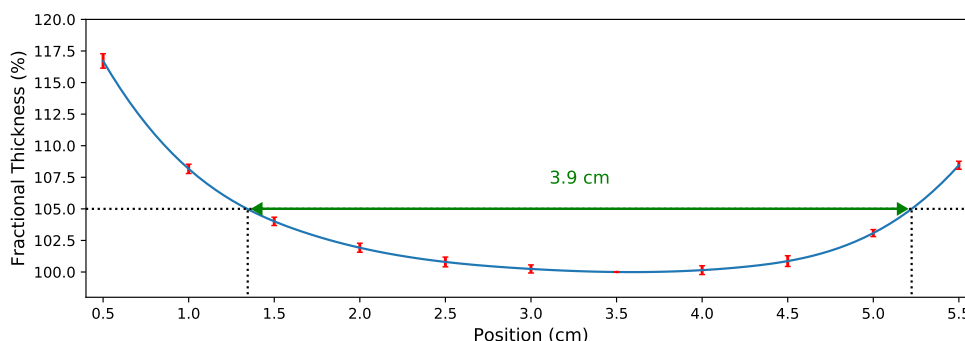
Figure 3.7: Fractional Thickness of Sample's Length

Similar results where obtained for lead chloride. However, less source is required to obtain

the same thickness due to its lower density. However, the source temperature needed to be increased to 420°C to achieve the same rate of evaporation. Within the thickness range between 50 and 200 nm the thickness remains linearly proportional to the amount of source material evaporated. The thickness to source material ratio was 4.0 and 4.2 nm/mg for lead iodide and lead chloride respectively. The roughness tends to increase with thickness limiting the maximum thickness below 200 nm, since the roughness increases more rapidly above 200 nm especially for lead iodide since the hexagonal crystal platelets begin to orientate vertically (fig. 3.17).

Both profilometer and thin film interference measurements could not be used to determine thickness of MAI thin films, due to the softness and high surface roughness. Therefore, a thickness to source material ratio could not be determined. However, a source temperature of 160°C was sufficient to achieve a evaporation rate of 1 mg/min.

3.3   Lead Halide and MAI Depositions

Thin films of lead iodide, lead chloride and MAI were deposited using the method discussed in chapter 3.2 with only change in the amount of source material and source temperature. The aim has been to compare the two lead halides and also gain information on the properties of MAI since even its density could not be found in literature.

As will be discussed in the following chapter, the lead halides expands by different amounts when converted to MAPbI$_3$ perovskite, therefore in order to evaluate perovskites of similar thickness, studies have been done on 150 and 100 nm PbI$_2$ and PbCl$_2$ which should provide approximately 300 nm perovskite thin films. Due to the limitation of the CVD deposition the thickness of samples may vary by 5%. An amount of 38, 24 and 30 mg of source were used for the PbI$_2$, PbCl$_2$ and MAI depositions respectively.

The XRD analysis of lead iodide revealed a preferred (00l) orientation, with crystals orientated parallel to the substrate due to the highly order trigonal crystal structure. The XRD analysis was done based on the P-3m1 space group, which can be seen in fig. 3.10. [92] Due to the preferred orientation, the XRD analysis can only provide information of the height of the unit cell (lattice constant c). The lattice constant could not be determined directly from the diffraction peak positions, due to sample displacement which has been verified with the use of a silicon powder.

The Rietveld fitting was first done for only the (001) and (004) diffraction peaks individually until the same parameters fit both peaks as seen in fig. 3.9. By taking into account -38 μm sample displacement and calibrating for instrumental broadening, the experimental peak position should have been shifted by -0.027° and -0.024° for the (001) and (004) peaks respectively. After the peaks were fitted individually, all peaks could be fitted simultaneously by performing a LeBail extraction, which provided a fit with an Rw value of 15%. The lattice constant c, has a value 6.971 Å and the Scherrer crystal size is 86 ± 8 nm. Information of each peak can be seen in appendix B.1.
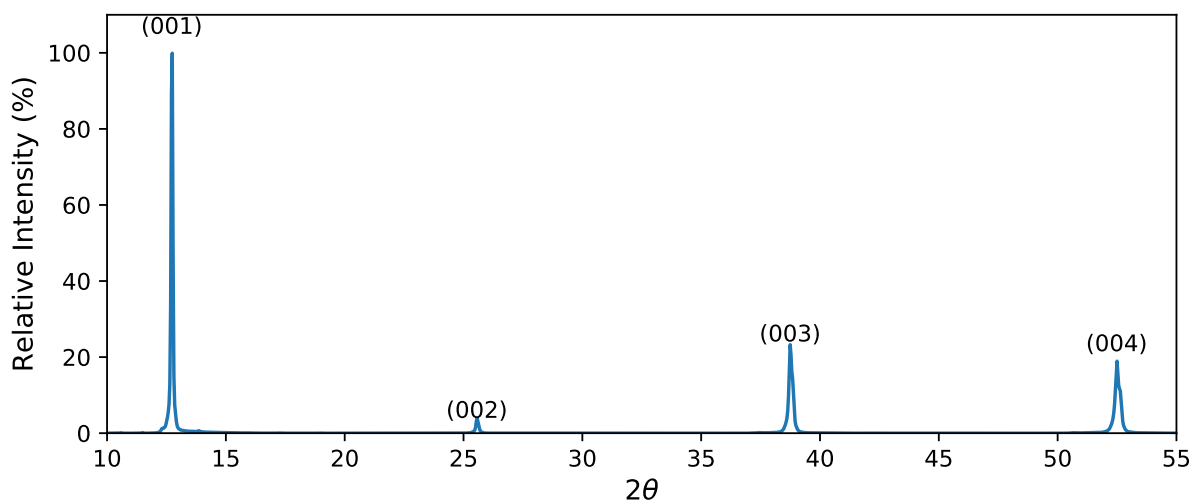
Figure 3.8: PbI$_2$ XRD
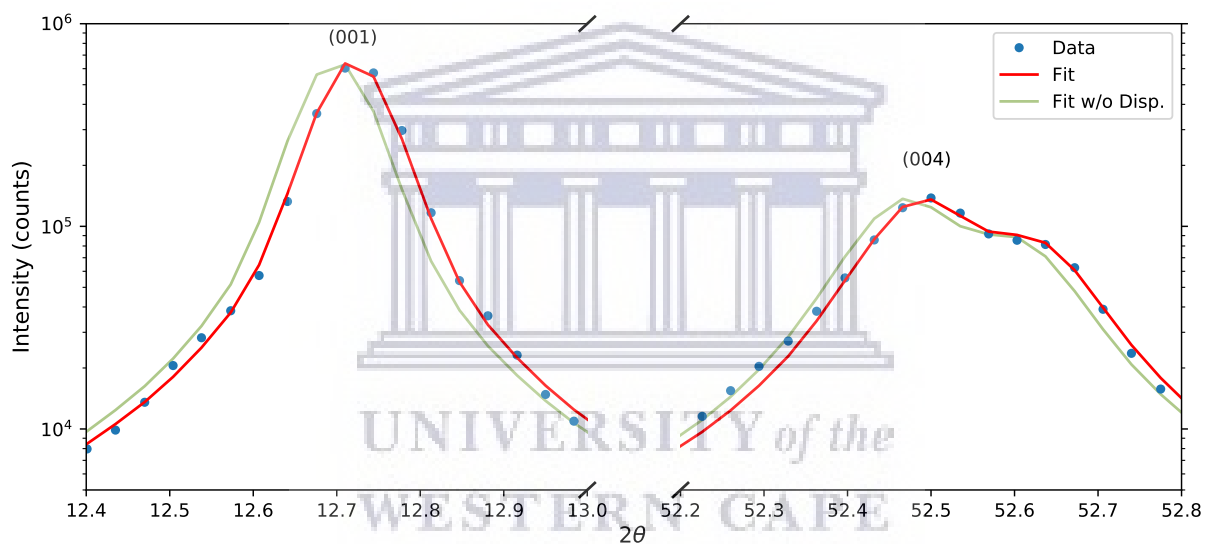
Figure 3.9: PbI$_2$ Rietveld Refinement

(001)
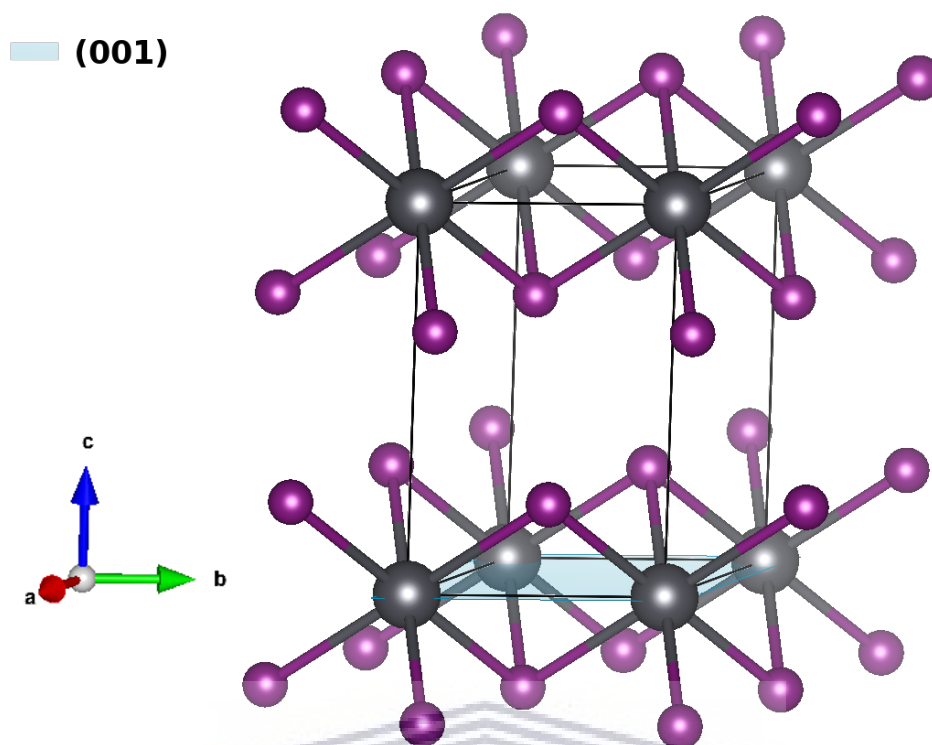
Figure 3.10: PbI$_2$ Crystal Structure

The lead chloride XRD analysis reveals a orthorhombic polycrystalline structure with no preferred orientation. Analysis has been done using the Pbnm space group (no. 62 setting 3).[93] The lattice constants were determined to be a = 9.036, b = 7.611 and c = 4.529 Å providing a density of 5.93 g/cm^3. Scherrer crystal size is 63.9 ± 0.6 nm. The unit cell of PbCl$_2$ can be seen in fig. 3.12 including the planes of the two most intense peaks, (111) and (121).
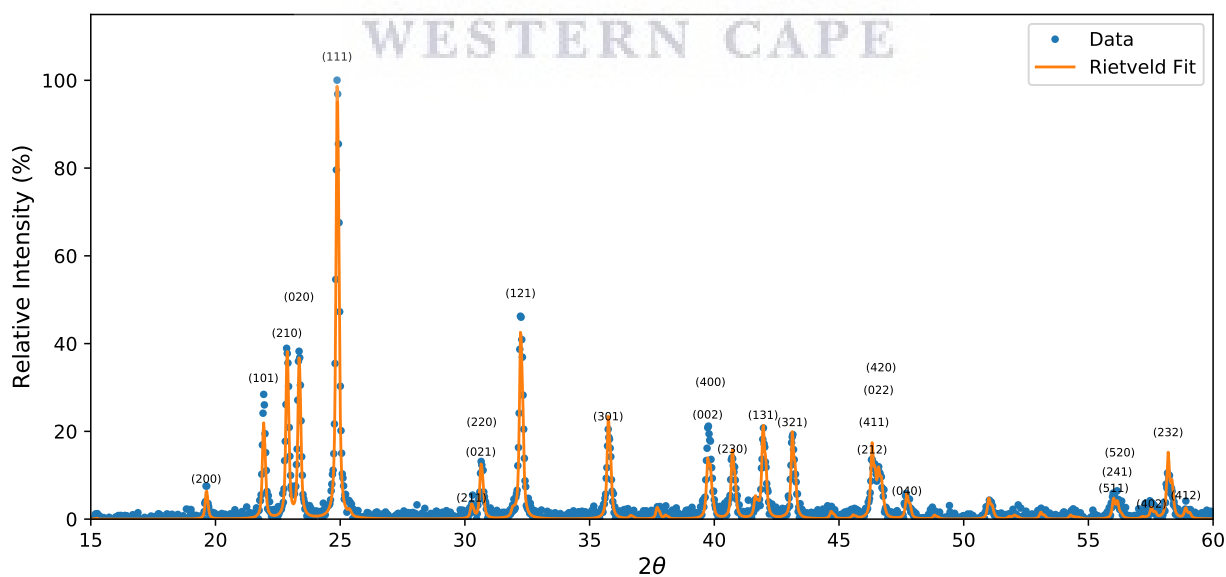
Figure 3.11: PbCl$_2$ XRD
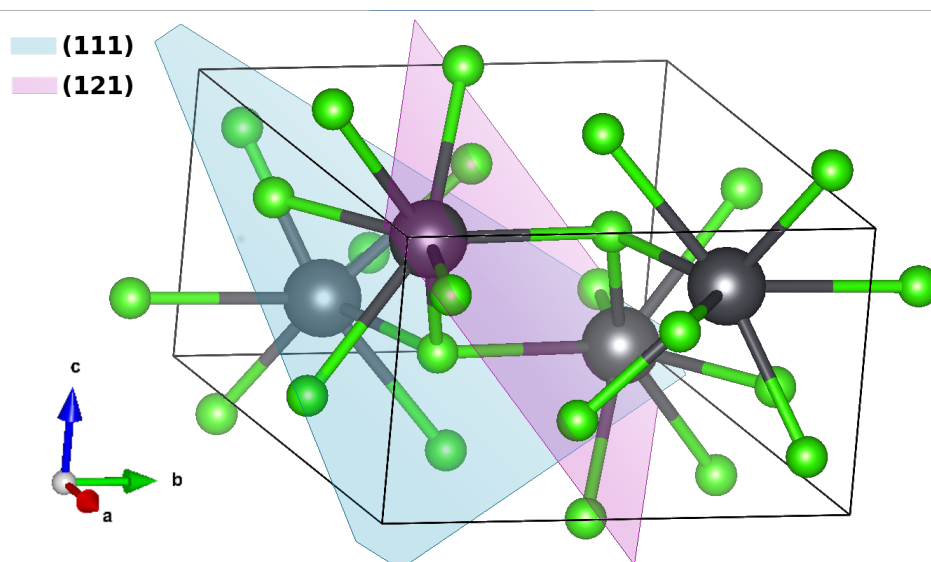
Figure 3.12: PbCl$_2$ Crystal Structure

The crystal structure of MAI has also been studied, by performing XRD analysis of both the powder and a thin film deposited by CVD on glass. As seen in fig. 3.13 MAI thin film also exhibits a similar preferred crystal orientation of (00l) similar to PbI$_2$. The crystallographic information file (cif) was created from parameters in the study by Yamamuro et al. (1992)[94]. MAI has a tetragonal structure with the P4/nmm space group.

The Rietveld refinement of the powder sample had a Rw value of 12% with slight adjustments to lattice constants with a = 5.126Å and c = 9.024Å . All identified peaks can be seen in table B.3 and based on the Scherrer equation the average crystal size is 79 ± 2 nm. The peaks that were detectable for the thin film could also be fitted with the same parameters and the average crystal size is 161 ± 3 nm, the increase in crystal size and preferred (00l) orientation resulted in the (002) peak to increase by a factor of 10. The (001) peak based on the crystal structure should be at 2θ of 9.8° which was bellow the measured 2θ range.
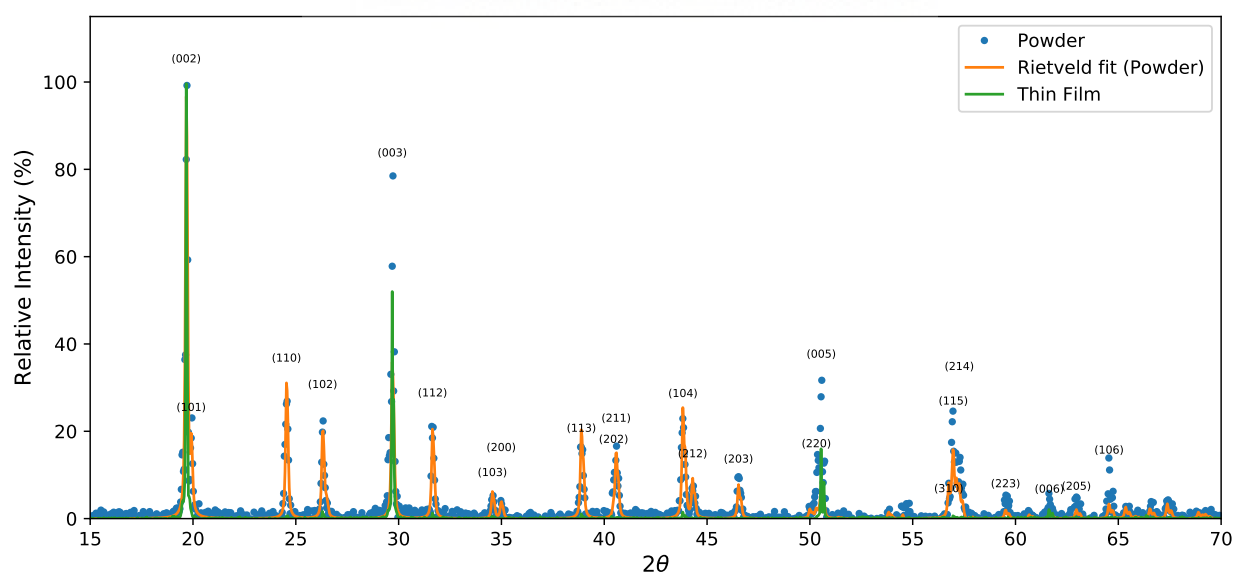
Figure 3.13: MAI XRD

As seen from fig. 3.14 the MAI crystal result in a vertical alignment of carbon, nitrogen and iodide atoms, with the distance between carbon and nitrogen being 1.429Å , iodide and carbon 4.049Å and due to the ionic bond between nitrogen and iodide the distance is 3.546Å . As seen in fig. 1.8 the MAI molecule should have 6 hydrogen atoms, the extra hydrogen in the crystal structure is due to the symmetry of the space group, therefore each hydrogen atom has an occupancy of 0.1875.
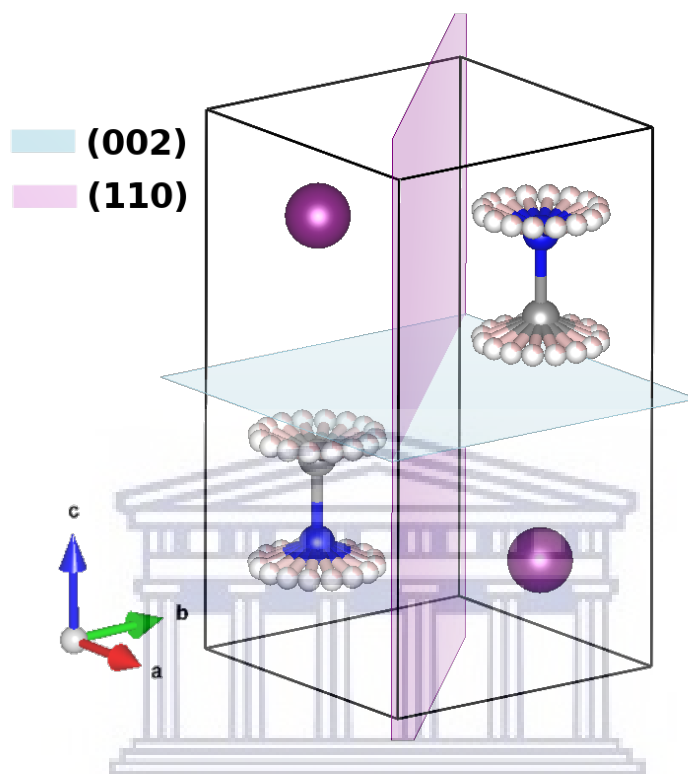
Figure 3.14: MAI Crystal Structure

3.4 Perovskite Conversion

The perovskite is formed sequentially through intercalation of the MAI molecules into the PbI_2 crystal structure, forming $MAPbI_3$. [95] $PbCl_2$ is also used in this study using the same MAI vapour exposure, however a by-product of MACl gas is formed in the process with the $PbCl_2$ converting into an intermediate mixture of $PbCl_2$, PbI_2 and PbICl until the final $MAPbI_{3-x}Cl_x$ perovskite is formed where x is typically less then 0.2. [96]

A complete conversion from the lead halide to the perovskite structure can be approximated by the thickness increases of the thin film.[97] By using the difference in density of the lead halide (ρ_h) and perovskite (ρ_p) and assuming that the number of moles remains constant the thickness ratio T_p/T_h can be determined, where V, A, m and M are the volume, area, mass and molar mass.

$$V = AT \tag{3.1a}$$

$$V = \frac{m}{\rho} \tag{3.1b}$$

$$moles = \frac{m}{M} \tag{3.1c}$$

$$\frac{T_p}{T_h} = \frac{M_p \rho_h}{M_h \rho_p} \tag{3.2}$$

Table 3.1: Thickness Expansion

Compound	Density (g/cm^3)	Molar Mass (g/mol)	Thickness Expansion
MAI	2.23	158.97	
MAPbI$_3$	4.2	619.98	
PbI$_2$	6.16	461.01	1.97
PbCl$_2$	5.85	278.11	3.11

The perovskite conversion is done by placing the MAI source material in a crucible at the centre of the first zone and the samples at the centre of the second zone placed onto the sample holder tilted at 15°. The tube is pumped down to a base pressure of 10^{-2} mbar and then a flow of N_2 is set to 100 SCCM which is kept constant until the end of the conversion. All three zones are heated to the desired temperatures with a ramp rate of 10 °C/min. The third zone is heated to the same temperature as the source in order to prevent the furthest region of the second zone to decrease in temperature. The usable area for conversion is 4x10cm where the width is limited to the tube diameter and the length is limited by uniformity in temperature as defined by the furnace. To achieve an evaporation rate of 1mg/min of MAI the source temperature is maintained at 160°C. The MAI source is crushed into a fine powder and spread uniformly in a ceramic crucible with a surface area of 7 cm^2. MAI can evaporate at lower temperatures at slower rates, thus in order to prevent the conversion from taking place at lower substrate temperatures, the desired substrate temperature is reached five minutes before reaching the set source temperature. Five

minutes before the end of the conversion the source is allowed to cool while the substrate temperature is held constant to decrease the evaporation rate. One minute before the conversion is completed the flow rate is increased to 500 SCCM to remove the MAI in the tube then the pressure is increased to 950 mbar (prevent evaporation of MAI from the perovskite), before allowing the substrate temperature to cool. Once the temperature has reached at least 50°C the samples are removed from the tube furnace.

The diffusion constant (D_g) of a gas is inversely proportional to the chamber pressure (eq. 3.3). The CVD system achieves a lowest pressure between 1 and 2 mbar with a N_2 flow rate of 100 SCCM. Therefore these parameters were kept constant to obtain the lowest possible working pressure to promote better diffusion of MAI gas towards the surface of the lead halide samples.[98]

$$D_g \propto \frac{T^{3/2}}{P} \tag{3.3}$$

Since the working pressure is proportional to the flow rate, increased flow lead to higher pressures. When testing conversions at 200 SCCM the thickness expansion was significantly less than at 100 SCCM under the same experimental conditions. A higher flow increases the velocity of the gas, providing less interaction time with the surface of the lead halide samples, with MAI vapour depositing on the tube walls at the coolest region at the end of the tube. This is the opposite result when lead halides are deposited from CVD, where a higher flow results in thicker thin films.

Initial testing of the perovskite conversions revealed that the substrate temperature is the most critical parameter that determines a complete and stable perovskite formation. If the temperature is below 120°C, then MAI can easily deposit onto surfaces. The lower the temperature the more MAI accumulates which covers the entire surrounding area in a white layer. Low temperatures results in perovskite which is easily over saturated and rapidly turns from dark brown to nearly transparent when exposed to moist air after the conversion which is due to the formation of a monohydrate (MA·H_2O)PbI_3.[99]

The influence of substrate temperature on the stability during perovskite conversions has been studied by evaluating the amount of MAI loss. Fully converted samples with a thickness of 300 nm were kept in the tube furnace with the usual conversion parameters without MAI source. The substrate temperature was kept constant for 20 minutes at either, 110, 130 or 150°C with a working pressure of 1 mbar.

At 150°C most of the MAI evaporated out of the perovskite structure reverting back to lead iodide, resulting in the thickness to decrease to 175 nm. At lower temperatures the perovskite is more stable with the thickness decreasing to 258 and 291 nm at 130°C and 110°C respectively. As measured by the profilometer, the initial roughness of 5 nm, increased to 7, 11 and 18 nm for the 110, 130 and 150°C samples respectively.

The percentage of transmitted light can be seen in fig. 3.15. Less light is absorbed as the perovskite reverts to lead iodide which has a larger bandgap. However, as the roughness increases, more light scatters of the surface and reduces the intensity of the interference fringes.

The perovskite conversion was also tested at elevated substrate temperatures revealing that perovskite could only be formed below 140°C. At 130°C only a partial converted perovskite

was formed under the same conditions as a 1 hour 120°C conversion, which resulted in a fully converted perovskite based on the thickness increase.
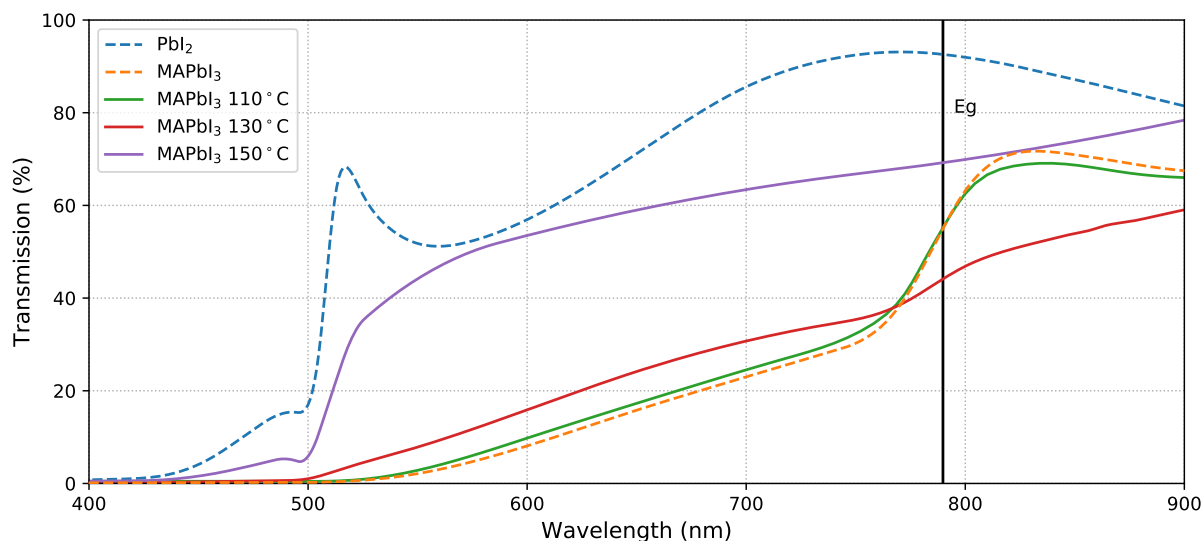
Figure 3.15: UV-Vis of PSK Annealed at Different Temperatures

After the ideal temperature of 120°C was identified, more in depth analyses were used to evaluate the amount of MAI exposure needed to completely form the perovskite structure and also the influence of different lead halide precursor thin films. For an accurate comparison the aim was to deposit 100nm of $PbCl_2$ and 150nm of PbI_2 via CVD to form 300nm perovskite after conversion. A 150 nm of PbI_2 was also dynamically spin-coated from a 0.8M solution dissolved in DMF. Since there had not been a suitable solvent, $PbCl_2$ could not be spin-coated, typically in literature $PbCl_2$ is spin-coated in a one-step process with MAI which increases the solubility of $PbCl_2$ in DMF.[36] The conversion was done for two different durations (a) 20 and (b) 60 minutes with all samples converted simultaneously. 100mg of MAI was placed in the crucible and the amount evaporated was determined after each experiment with 22 and 64 mg evaporated in the 20 and 60 min. experiments receptively. For comparison 150 nm CVD PbI_2 samples was converted at a substrate temperature of 80°C with an conversion duration of 10 and 20 minutes, which resulted in an under and over exposed perovskite, labelled (c) and (d) respectively.

Fig. 3.16 compares the SEM cross-section of the different converted samples on glass. The thickness and roughness were determined by tracing the top of the perovskite thin film and digitizing the data according to the scale into x and y coordinates. The thickness is determined from the average height and the roughness from the standard deviation. The SEM images provide a more accurate roughness than the profilometer, since the tip is 5 μm in diameter which is larger than the length of the cross-section images. The roughness of the samples measured by the profilometer varied between 4 and 6 nm and thickness was within 5% of that measured by SEM, which is similar to the roughness obtain from SEM.

All three samples after 20 minutes conversion were nearly fully converted based on the theoretically thickness expansion (tab. 3.1) and after 60 minutes reached the expected thickness. It has been studied that the growth rate of perovskite via sequential MAI vapour exposure occurs at a high initial rate as MAI can easily diffuse into PbI_2, then the growth slows until complete saturation.[100]
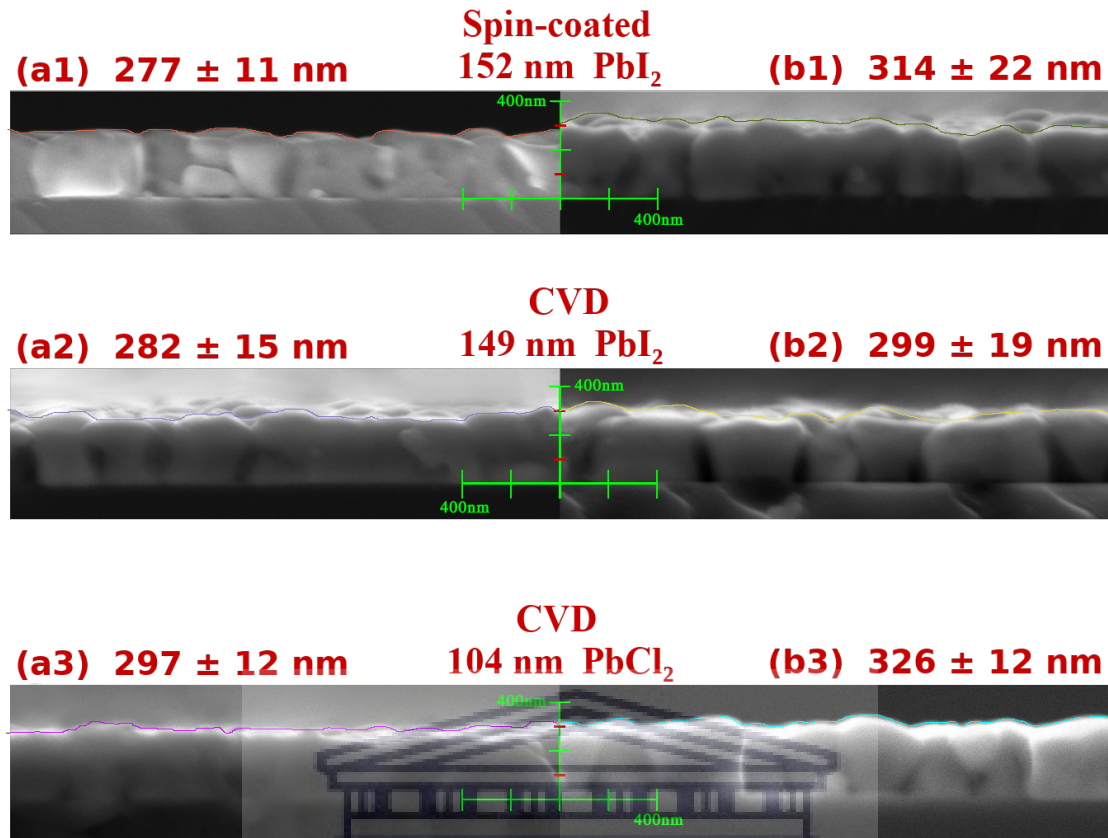
Figure 3.16: Perovskite Conversion SEM Cross-section

The SEM image of the three different lead halides can be seen in fig. 3.17. The lead iodide samples had a flat surface with thin grain boundaries which makes distinguishing grains difficult. However, the lead chloride grain size was determined to be 131 ± 54 nm. The CVD lead iodide had the largest grains up to 1 micron with noticeable hexagonal crystals protruding out of the surface which correlates with the high peak intensity observed from the XRD analysis due to large crystallite size.
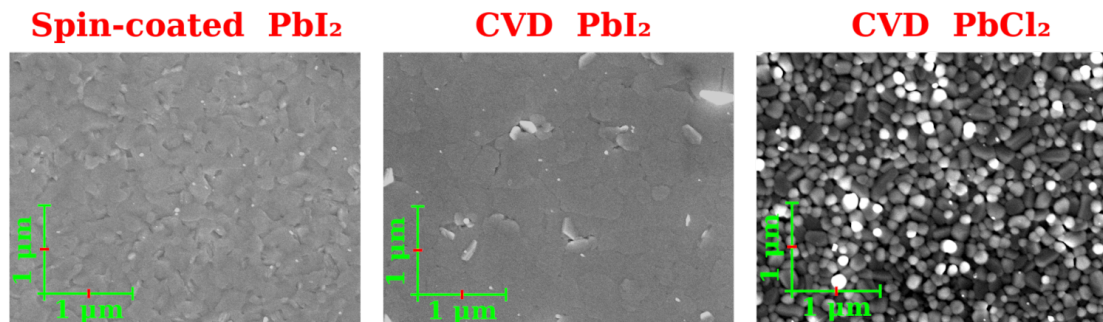
Figure 3.17: SEM of Lead Halide Before Conversion
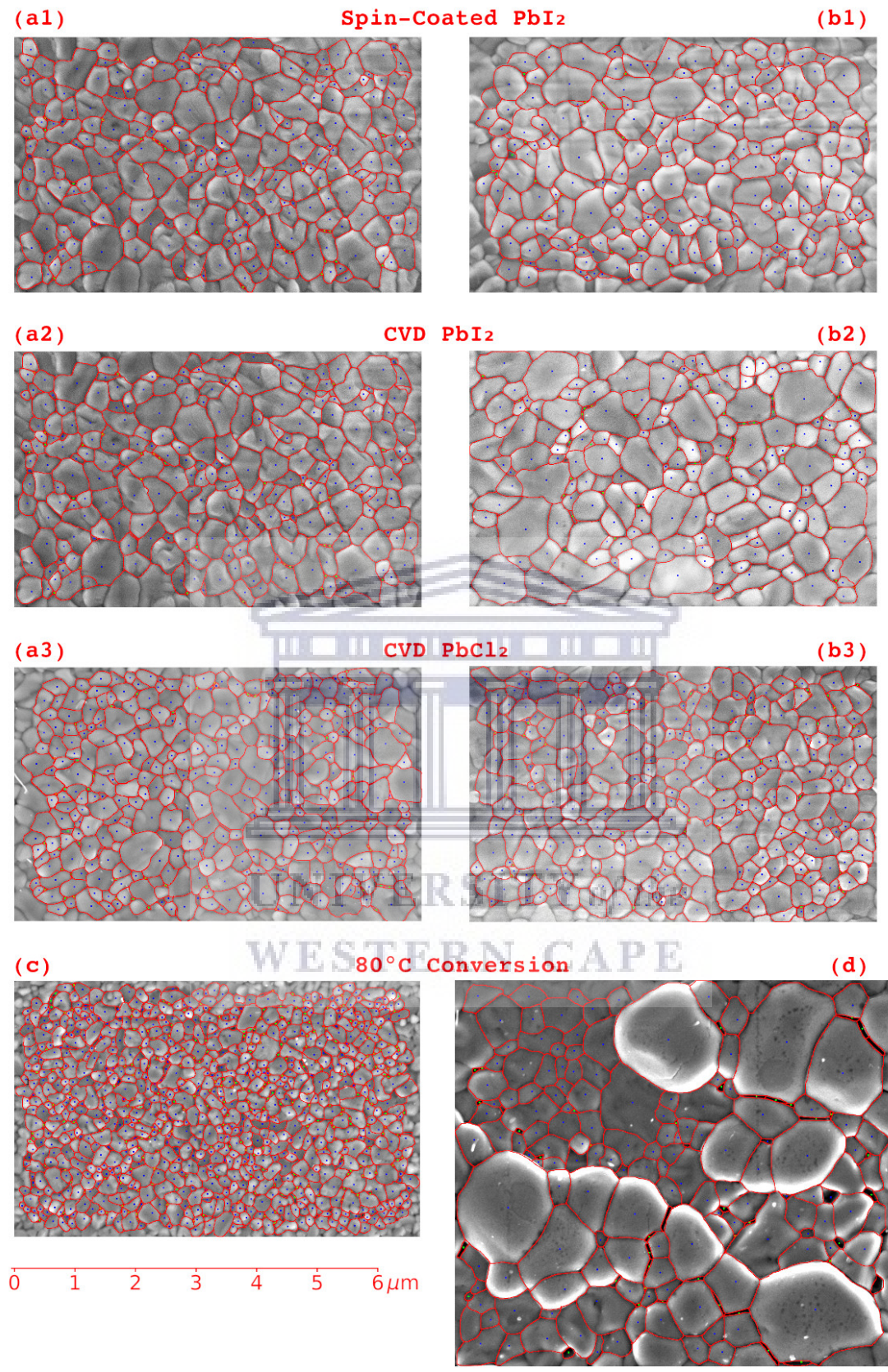
Figure 3.18: Perovskite Conversion SEM
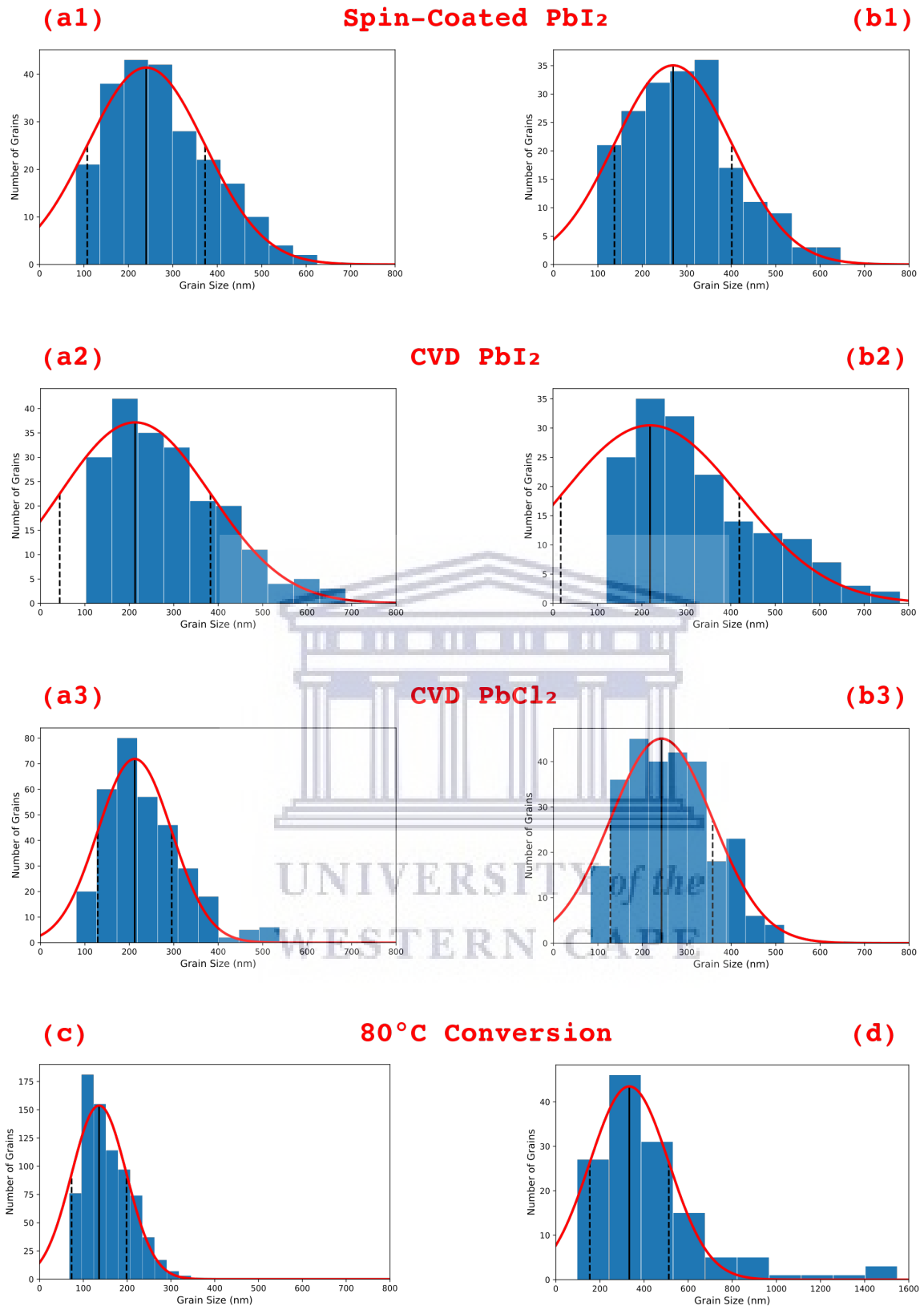
Figure 3.19: Gaussian Fit of Perovskite Conversion

All three samples had an increase in grain size due to the longer 60 min. conversion duration. The largest perovskite grain size was obtained by converting CVD PbI$_2$ which had an average grain size of 330 nm which had also been the largest increase of 14% from the 20 min. conversion. Even though the spin-coated lead iodide had more defects before conversion compared to CVD, the final perovskite was very similar in morphology. The lead chloride which had the smallest grain size also had the smallest grains when converted to perovskite for the 120°C conversions.

The low temperature conversions had the worse morphology, with the under exposed (10 min.) having a grain size of 155 nm and the over exposed (20 min.) sample being highly unstable, with samples visibly degrading while performing SEM measurements as holes formed from being bombarded with electrons. A similar unusual morphology with large protruding grains had also been obtained by Moser et al. (2020) when a mixture of PbI$_2$ and CsBr were over exposed with FAI vapour.[101]

All perovskites indicate a compact morphology with a void percentage below 1% except the under exposed sample, which had not completely crystallized into the perovskite structure evident by the PbI$_2$ peak in the XRD analysis (fig. 3.26).

Table 3.2: Perovskite Grain Size

		Sample	Avg. Grain	Gaussian	Avg. Void	Void %
a1		SC PbI2 (20 min.)	270 ± 110	240 ± 130	44 ± 9	0.41
b1		SC PbI2 (60 min.)	300 ± 120	270 ± 130	55 ± 14	0.52
a2		CVD PbI2 (20 min.)	290 ± 130	210 ± 170	54 ± 13	0.57
b2		CVD PbI2 (60 min.)	330 ± 150	220 ± 200	60 ± 15	0.84
a3		CVD PbCl2 (20 min.)	235 ± 87	212 ± 83	45 ± 13	0.75
b3		CVD PbCl2 (60 min.)	261 ± 94	240 ± 120	46 ± 9	0.75
c		80°C Under Exposed	155 ± 53	136 ± 63	45 ± 11	2.71
d		80°C Under Exposed	430 ± 260	330 ± 180	78 ± 28	0.78

In order to determine the band gap of the lead halides and perovskite thin films the same one hour conversion was performed where samples of different thicknesses where simultaneously converted. Different CVD lead halide thicknesses were used to account for thin film interference due to specular UV-Vis measurement.[102] As seen in fig. 3.20 there was no significant difference between converting lead iodide or lead chloride. The average band gap of the pure MAPbI$_3$ was 1.5930 ± 0.0006 eV and the MAPbI$_{3-x}$Cl$_x$ had a value of 1.594 ± 0.001 eV. Which falls within the typical range of 1.57 and 1.63 eV for pure MAPBI$_3$ and chloride doped perovskite with the latter resulting in a larger band gap.[103] The lead iodide precursor thin films had an average band gap of 2.431 ± 0.002 eV which differs from the typical range between 2.30 and 2.38 found in literature.[104][105] Due to the large band gap of PbCl2 of 5 eV, the band gap calculation could not be performed.[106] The absorbance coefficient (α) is approximated using eq. 2.5 and the vertical lines in fig.3.20 indicates the linear regions used for calculations. The approximated absorbance can be seen in fig. 3.21 which were determined from specular reflection and transmission measurements, the measurement of the Corning glass that was used as the substrate is also included.
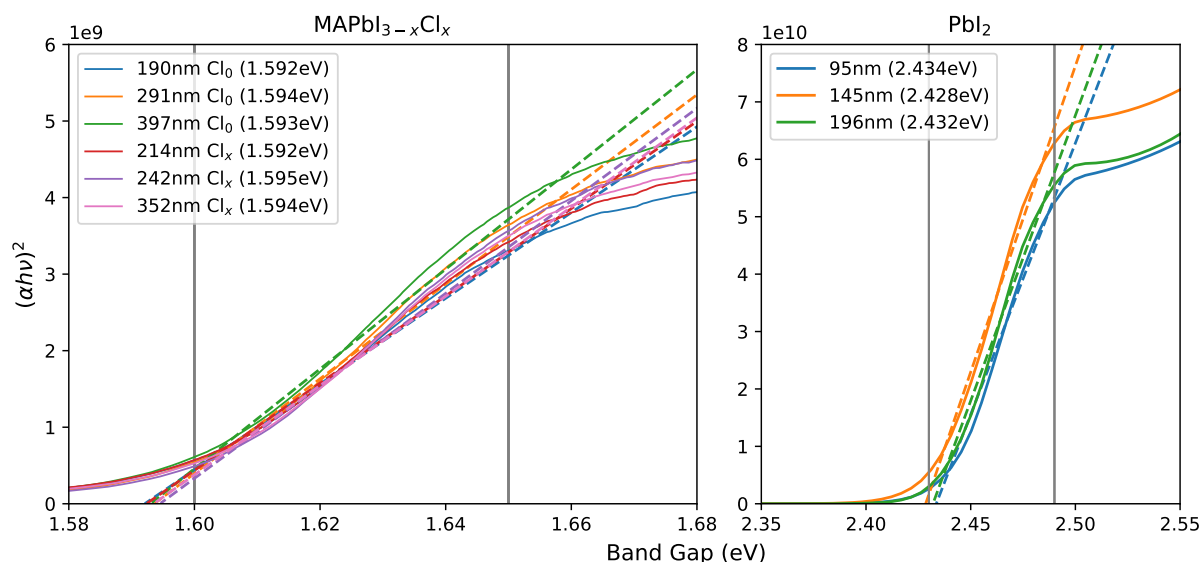
Figure 3.20: Tauc Plot of Lead Iodide and Perovskite
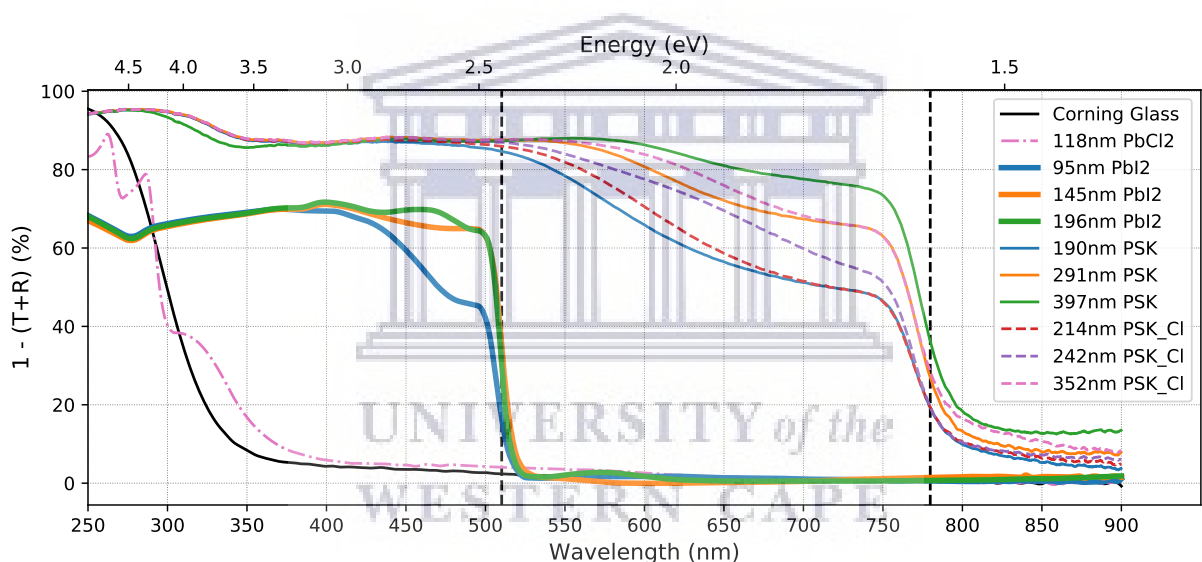
Figure 3.21: UV-Vis of Lead Halides and Perovskite

The XRD analysis of the 60 min. perovskite can be seen in fig. 3.22, there was no detectable lead iodide peaks for any of the three samples indicating a complete conversion, with the perovskite formed from CVD PbI_2 having the most intense peaks which correlates with its large grain size. Since the XRD spectra are very similar it had also been plotted with an overlaying relative intensity (log scale) in comparison to the accumulative peak intensity of the (002) and (001) diffraction peaks. Most noticeable is the increase in peak position of the CVD $PbCl_2$ perovskite which corresponds to a smaller unit cell with a calculated volume of 955 $Å^3$ compared to CVD PbI2 of 993 $Å^3$.
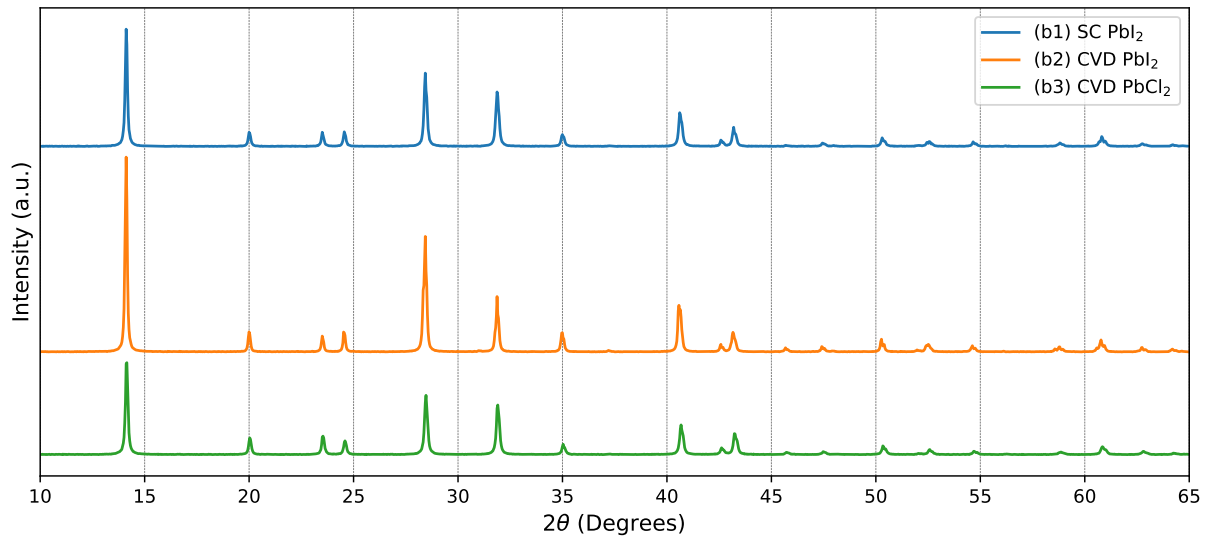
Figure 3.22: XRD of Fully Converted Perovskite
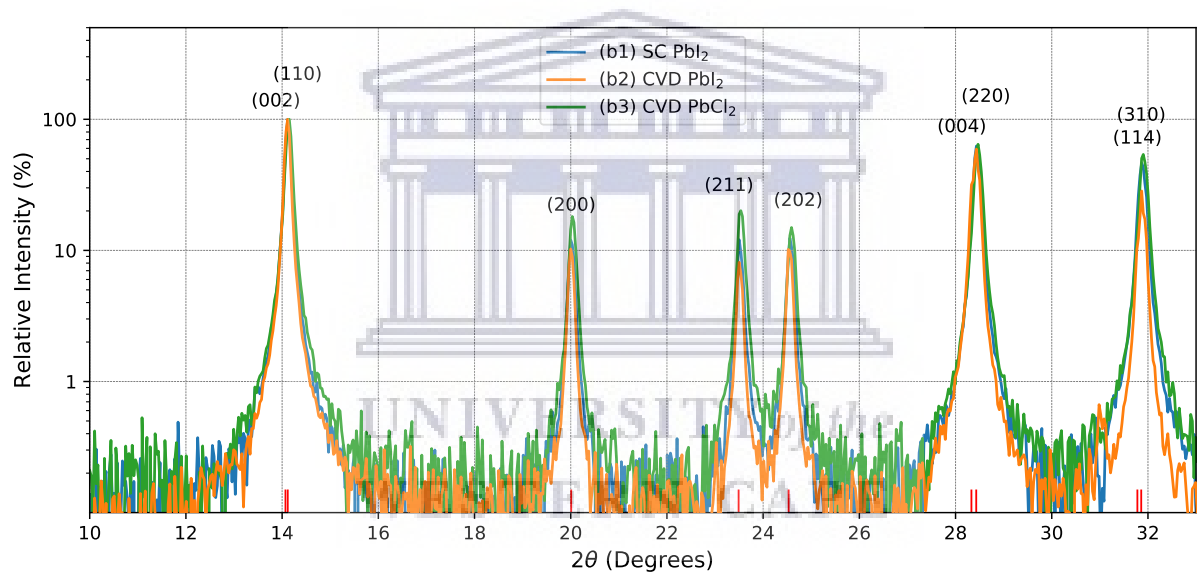
Figure 3.23: XRD of Fully Converted Perovskite 10 - 33°
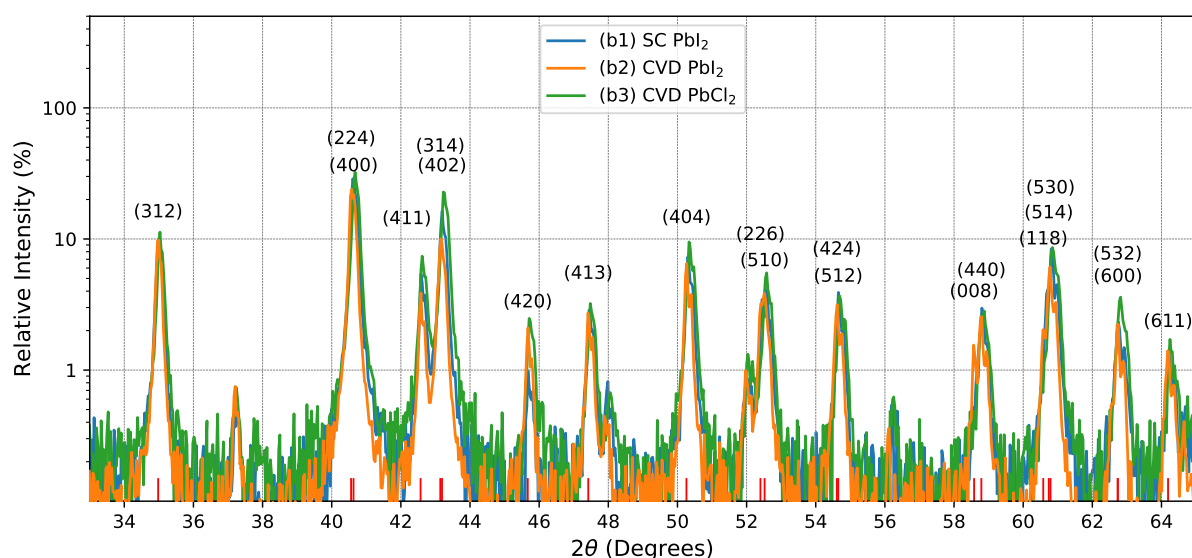
Figure 3.24: XRD of Fully Converted Perovskite 33 - 65°

All three of the 20-minute converted samples indicate a trace amount of unconverted PbI_2 including the CVD $PbCl_2$ sample which had no trace of $PbCl_2$ indicating that the $PbCl_2$ is nearly completely converted to PbI_2 during the exposure with MAI. The chloride content had also been barely detectable in the RBS study with less than 2% of the iodide substituted with chloride (tab. 3.4). The 60-minute CVD Pb_2 based perovskite had also been included in fig. 3.25 which demonstrates that the longer conversion duration lead to an increase in peak intensity compared to the 20 min. conversions due to larger crystallite size.
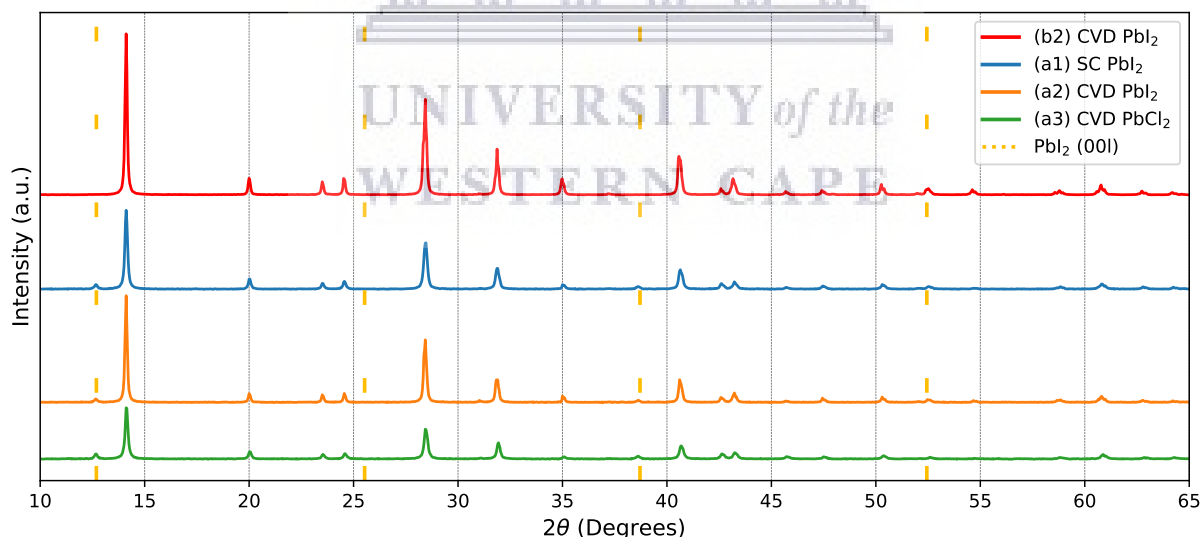
Figure 3.25: XRD of Perovskite Partial Conversion

The 80°C conversions (fig. 3.26) had the lowest peak intensity with 5 times lower peak intensity compared to the 60 min. CVD PbI_2 conversion even though the FWHM indicates large crystallite size. The under exposed sample had noticeable PbI_2 (001) and (003) peaks, indicating that it was the most incomplete of all the conversions. The lead iodide peaks

indicated an increase in the lattice constant from 6.971 to 6.981 Å as the remaining PbI_2 crystals are partially converted due to the intercalation of MAI.

The over exposed sample had no trace of MAI peaks, which suggests that no MAI crystals have formed even with the large surplus of MAI throughout the entire structure confirmed by RBS. There had also been 3 unknown peaks detected in the over exposed samples, that might be due to water molecules within the crystal structure forming a monohydrate, due to the high moisture sensitivity of the over saturated MAI perovskite with the closest match at 10.6°. [99]
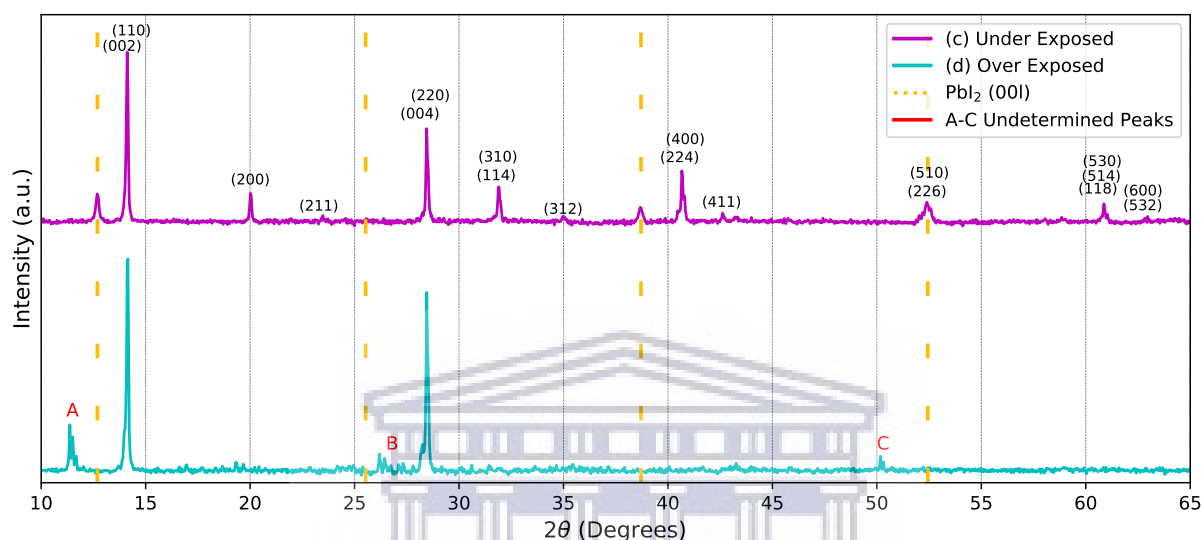
Figure 3.26: XRD of Perovskite at 80°C Conversion

Table 3.3: Perovskite XRD Analysis

	Sample	a (Å)	c (Å)	C. Size*	C. Size**	Texture	Disp (μm)
a1	SC PbI2 (20 min.)	8.873	12.579	65 ± 2	109	123	-29
b1	SC PbI2 (60 min.)	8.876	12.574	75 ± 2	143	406	-32
a2	CVD PbI2 (20 min.)	8.875	12.580	86 ± 3	172	21	-36
b2	CVD PbI2 (60 min.)	8.880	12.599	93 ± 3	188	19	-46
a3	CVD PbCl2 (20 min.)	8.870	12.558	55 ± 2	84	215	-44
b3	CVD PbCl2 (60 min.)	8.872	12.564	69 ± 2	121	621	-52
c	80°C (PSK)	8.866	12.546	63 ± 3	112	25	-23
c	80°C (PbI_2)	-	6.981	66 ± 3	183	-	-23
d	80°C Over Exposed	8.868	12.544	95 ± 9	206	219	-30

*Scherrer **Rietveld Crystal size in nanometre

Based on the XRD analysis both lead halides produce similar perovskite structures and have a tetragonal crystal structure at room temperature as seen in fig. 3.27(a). However, the structure does not deviate by a large amount from the ideal cubic phase perovskite. Fig. 3.27(b) is a section of the unit cell which simplifies the structure for comparison to the cubic phase indicating the difference in perovskite structure converted from CVD PbI_2 and $PbCl_2$. The height of the perovskite only deviates by 0.3% from its width with a slight

60

8.7° tilt in the bond angle between iodide and lead atoms, which alternates with an inward and outwards bending. The cubic structure as determined by Ju et al. (2017) had a lattice constant of a = 6.30Å with the CVD PbI_2 perovskite being the closest in structure.[107]
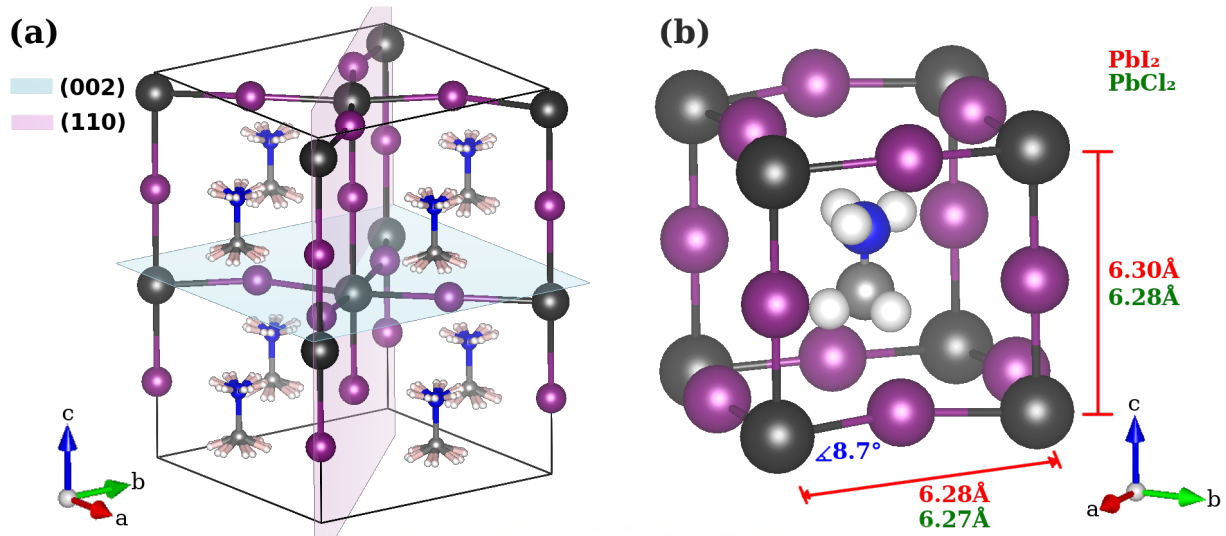
Figure 3.27: Perovskite Structure (a) I4cm Space group and (b) Simplified to Conventional Structure

To illustrate the difference in XRD spectra of the tetragonal to cubic phase, the cubic phase was simulated using the Pm-3m space group. Since the cubic structure is more symmetric it will have less diffraction peaks. All tetragonal peaks that are clearly visible and separate from that of the cubic phase have been highlighted in fig. 3.28 with the most prominent peak being (211) at a 2θ angle of 23.5°.
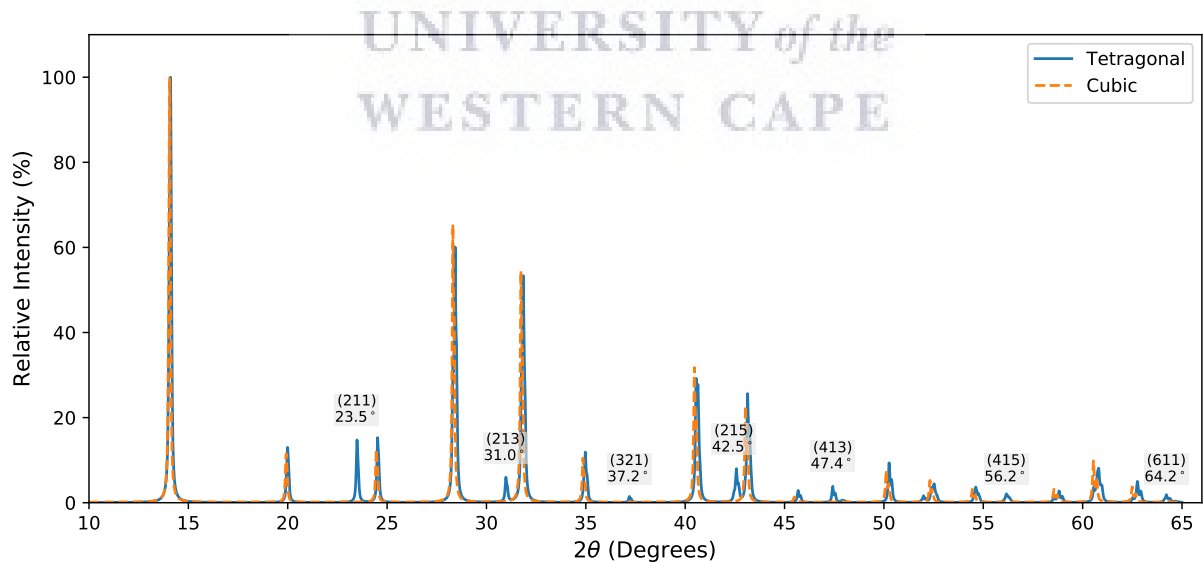
Figure 3.28: Simulation Comparing Tetragonal to Cubic $MAPbI_3$

The samples that were used for RBS where deposited on a silicon substrate since glass contains barium that has a higher kinematic factor than chloride which would result in a overlap of peaks and additional noise in the experimental data. Since the beam intensity had to be reduced to prevent damage of the samples, the data acquisition time had to be increased resulting in approximately 30 min. beam exposure per sample, thus limiting the number of samples that can be measured due to time constraints. Attempts at measuring a sample of MAI was unsuccessful, since the sample was completely damaged within 5 minutes of beam exposure evident with no further counts being collected in the region of interest. All other samples had no signs of any damage.

The number of lead atoms in the PbI_2 and $PbCl_2$ samples from RBS analysis was 124.2 and 126.1 ($10^{15}/cm^2$) respectively. The iodide to lead atomic ratio was 2.01 as expected from PbI_2. However, the chloride ratio for the $PbCl_2$ was slightly lower at 1.94. As seen in fig. 3.29, the chloride peak is significantly lower in intensity compared to iodide, which provides less accurate calculations, hence the possible lower chloride concentration. The $PbCl_2$ powder also had a lower purity of 98% compared to the 99% for PbI_2. Chloride has two abundant isotopes (tab. 2.1) producing two peaks with the reduced energy (E_1) due to their respective kinematic factors indicated within the magnified region of fig. 3.29. The RBS also revealed a uniform distribution for both compounds with only a single layer needed for fitting.
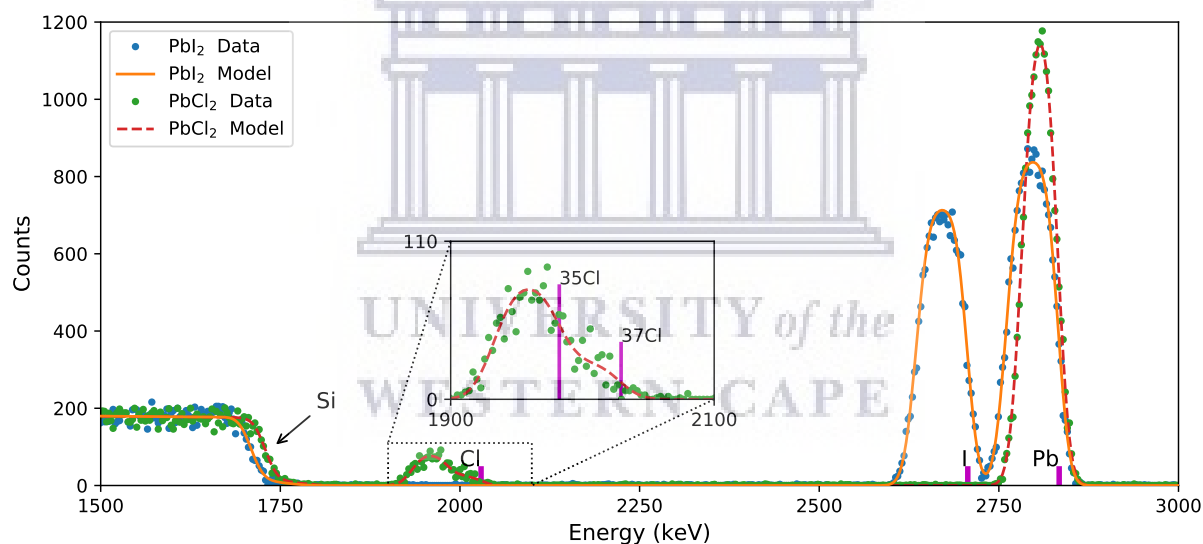
Figure 3.29: RBS analysis of Lead Halides

The RBS of the perovskite samples converted at the ideal 120°C (fig. 3.30) revealed a similar nearly ideal stoichiometry with a slightly lower halide concentration suggestion a small amount of under conversion. The chloride concentration was too low for accurate calculation, indicated that almost all the chloride is removed during the conversion process as the $MAPbI_{3-x}Cl_x$ is formed. The two spectra nearly perfectly overlap due to their similar thicknesses (see tab. 3.31) showcasing the level of control that can be achieved with CVD perovskite formation. Several samples were made for the RBS study with samples with the closest matching thickness chosen for RBS measurements.
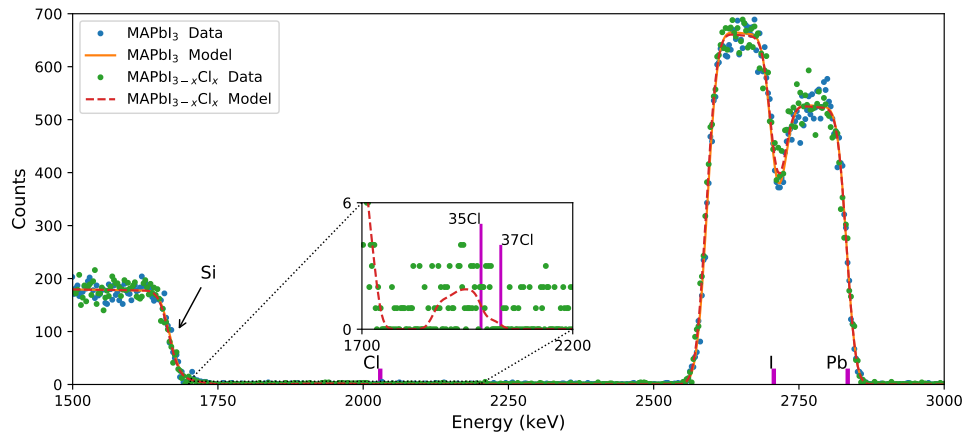
Figure 3.30: RBS analysis of Perovskite

The lead iodide samples converted at 80°C were more difficult to control since MAI vapour can more easily deposit onto the surface of the thin film. The sample with a 10 minute conversion had nearly the same iodide concentration as the 120°C, 60 minute conversion. However, the XRD revealed much greater lead iodide peaks, which suggests that there is larger portion of MAI which did not fully bond with the lead iodide to form a complete perovskite structure. After only 20 minutes at 80°C the perovskite is completely oversaturated with 1.5 times the expected iodide concentration. RBS also revealed a uniform distribution of iodide thus the higher concentration of unconverted MAI is mixed within the perovskite structure. All thicknesses were determined from RBS using the densities in table 3.1 except the over exposed sample which deviates too greatly form the ideal stoichiometry.
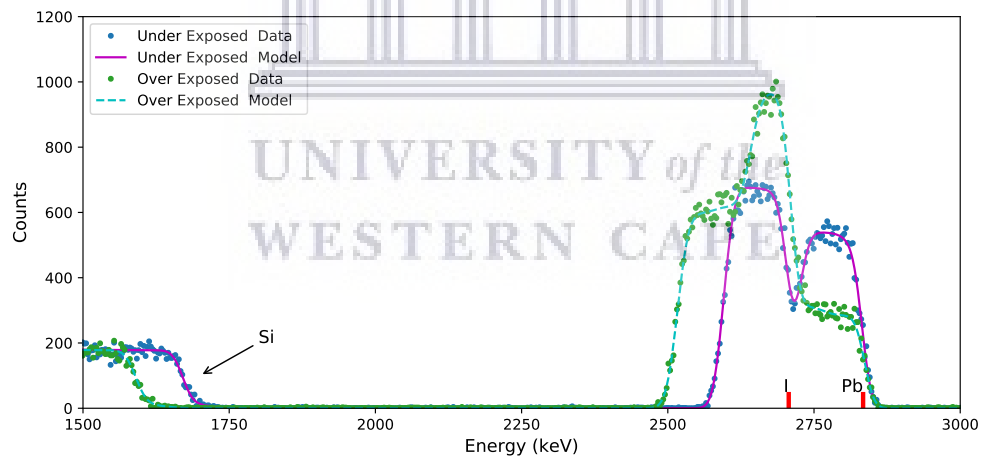
Figure 3.31: RBS Analysis of Perovskite at 80°C Conversion

Table 3.4: Perovskite RBS Analysis Ratio to Pb

Sample	Pb (10^{15}/cm^2)	I	Cl	C	N	H	Thick. (nm)
PbI$_2$	124.2	2.01					155
PbCl$_2$	126.1		1.94				99
MAPbI$_3$	124.0	2.97		1.01	1.01	5.98	303
MAPbI$_{3-x}$Cl$_x$	125.0	2.96	0.05	0.97	0.98	5.96	306
Under exposed	120.7	2.95		0.93	0.95	5.68	294
Over exposed	122.4	4.64		2.96	2.97	17.67	-

Chapter 4

Perovskite Solar Cells

This chapter will focus on the construction of perovskite laboratory solar cells, with attention on the deposition of each layer including encapsulation. The influence of changes in the architecture which affect PV performance will be discussed. The results from this work is also compared to similar research in literature.

4.1 Cell Design

The solar cell design is regulated by the dimensions of the TCO and the electrode (Au or Ag), with all the other layers stacked between to form the functioning solar cell. The overlapping area between the TCO and electrode forms the active area. The cells are illuminated through a mask with an aperture slightly smaller than the active area to ensure the most accurate area of the cell. The portion of the active area that is masked forms the dark-state area. [108]

In a study by Xu et al. (2015) the size of the dark-state area compared to the active area can influence the IV curve of the solar cell. It has been concluded that the larger the dark-state area in proportion to the active area, the higher the V_{oc}, but the lower the FF. By only changing the aperture their PCE increased from 11.3% to 13.3% by using the smallest aperture size of 4mm^2 with an active area of 24mm^2 (100mm^2 = 1cm^2). The general perovskite architecture has been used FTO/c-TiO$_2$/MAPbI$_3$/Spiro-Ometad/Au.[108]

Laboratory solar cells are typically tested with an illuminated area of 1cm^2. However, the common practice in the field of perovskite solar cells is to subdivide a sample into multiple cells less than 10mm^2. As mentioned in chapter 1 all certified measurements of perovskite cells are done with an illuminated area between 9 and 10mm^2 which is large enough to be accepted by NREL for record efficiency.

Having multiple cells per sample is useful to gather more statistical information on the deviation in performance. This is especially useful to identify non-uniform defects of a sample, which can be used to evaluate improvements in a deposition technique for upscaling. Since lead halide perovskites have diffusion lengths less than 10μm for polycrystalline and less than 100μm for single crystal [109], one can easily separate adjacent cells by ensuring a gap between the electrode on the order of a few 100μm obtained via the deposition mask, without the need to etch the TCO for each cell. This allows all cells to be illuminated at once and be measured individually without needing a aperture mask that illuminates only one cell at a time.

The Ossila solar cell design seen in fig. 4.1 was used for this work. The active area is 4mm^2 and the illuminated area which is restricted by the aperture mask is 2.56mm^2. In figure 4.1 a)

the yellow rectangle indicates the electrode deposition of an individual cell and the green square indicates the illuminated area. Samples are designed to be encapsulated by an UV curable epoxy with a glass cover slip with a size of 12 by 15mm, which completely covers the cells including the metal electrode. This protects the cells from moisture and accidental scratching during handling of the samples as seen in fig. 4.1 (b).The numbers in fig. 4.1 (a), indicates the position of the spring loaded gold coated pins marked with yellow circles. Pins 1, 6, 7 and 12 are to connect to the ground (negative) terminal and the others pins are the positive terminals of each individual cell.
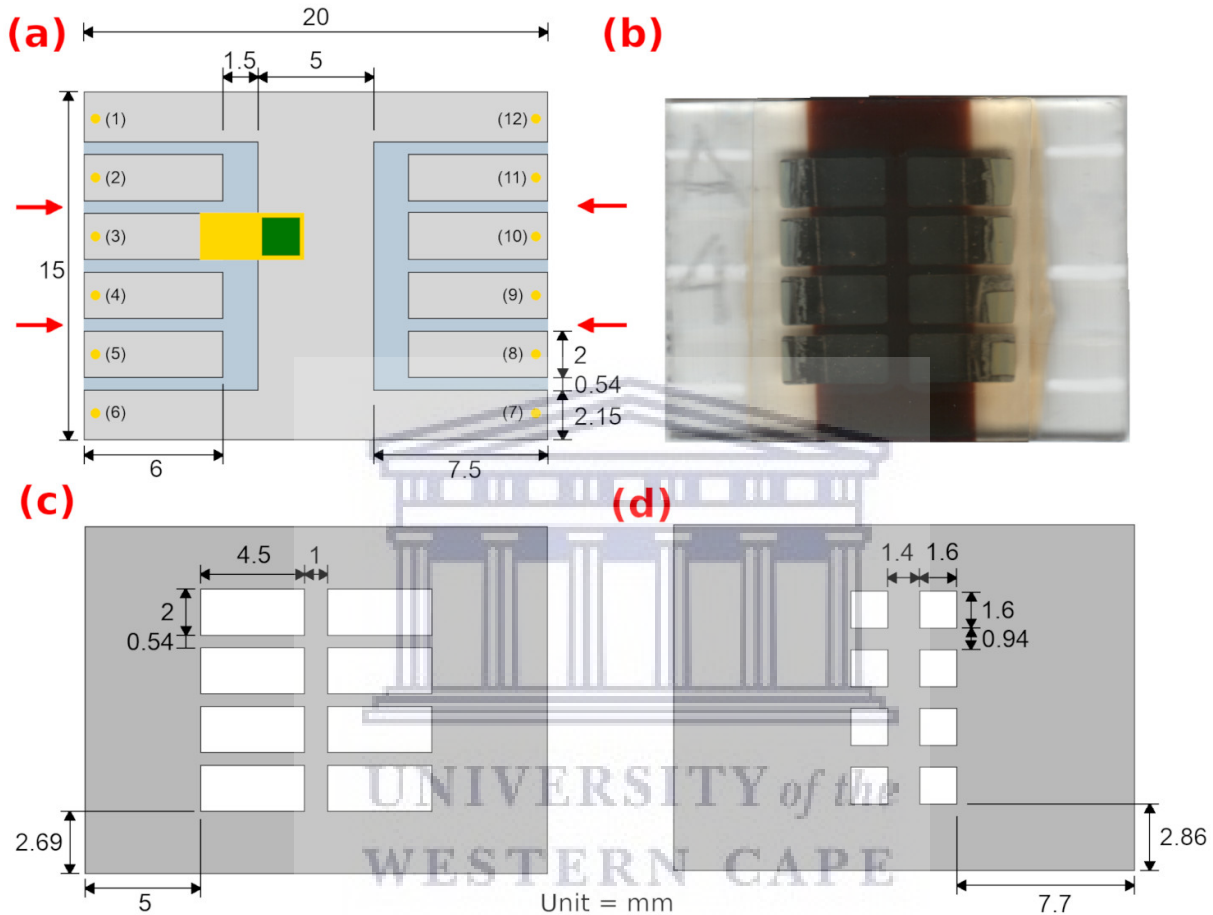
Figure 4.1: Ossila 8 Pixel TCO Design: (a) Etched TCO, (b) Solar Cell Sample, (c) Electrode Deposition Mask, (d) Aperture Mask

According to the ASTM 948-16 standards solar cells must be measured by a four-wire connection, which is capable via the SMU used in this study, Keithley 2420. The reason is to remove contact resistance between the terminals and the sample. Since each sample has 4 ground connections, 2 can be used to measure a single cell. However, an additional positive pin is required, hence the gap between contacts as indicated with red arrows in fig. 4.1(a) is not etched thus, combining two adjacent cells to give a total illuminated area of 5.12mm^2 with 4 cells per sample. By constructing a device consisting of only etched FTO and silver, it was confirmed that most resistance in measurements is from contact resistance between the gold pins and the FTO with a value of $83 \pm 7\,\Omega$. By using the four-wire configuration as demonstrated in fig. 4.2 the resistance was $48 \pm 2\,\Omega$, thus, a reduction of 35Ω in contact resistance. As an approximation to determine the resistance of the FTO from its sheet resistance (R_{SH}) and the path current must propagate through the FTO the following equation is used:

$$R = \frac{\rho L}{tW} = \frac{R_{SH}L}{W} \tag{4.1}$$

where ρ is the resistivity, L and W is the distance and width current must propagate through and t is the thickness of the FTO. FTO having a R_{SH} of 10 Ω/sq if propagating through L= 2mm and W = 6mm as well as L = 4mm and W = 5mm giving a total resistance of 42.5 Ω.

One can also approximate the influence that resistance of the FTO has on the efficiency measurements of a solar cell, since transmitted power loss is equal to I^{2}R. For a typical MAPbI$_3$ based solar cell with a PCE of 20%, J$_{sc}$ of 22.7 mA/cm^2, V$_{oc}$ of 1.1V and a FF of 80% a power loss due to a resistance of 83Ω would equate to a 11% decrease in PCE to value of 17.8%, with contact resistance removed the PCE would still decrease to a value of 18.7%. The original design by Ossila had a resistance of 90Ω with an area of 2.56mm^2 which would give a reduced PCE of 18.8%. Thus, the alteration to the initial design has no advantage in terms of PCE. However, the cell size of 5.12mm^2 is closer to the typical cell area of 10mm^2.

The greatest concern with the Ossila solar cell 8 pixel design is the small gap (1.5mm) between the active are and the edge of the TCO. The TCO on either side of the active area must remain clean to ensure contact to the cells. This is mostly a concern when spin-coating is used to deposit a necessary layer during fabrication. Either the edges must be masked with tape, or cleaned with an appropriate solvent, depending on what compound is spin-coated this could lead to a defective active area.
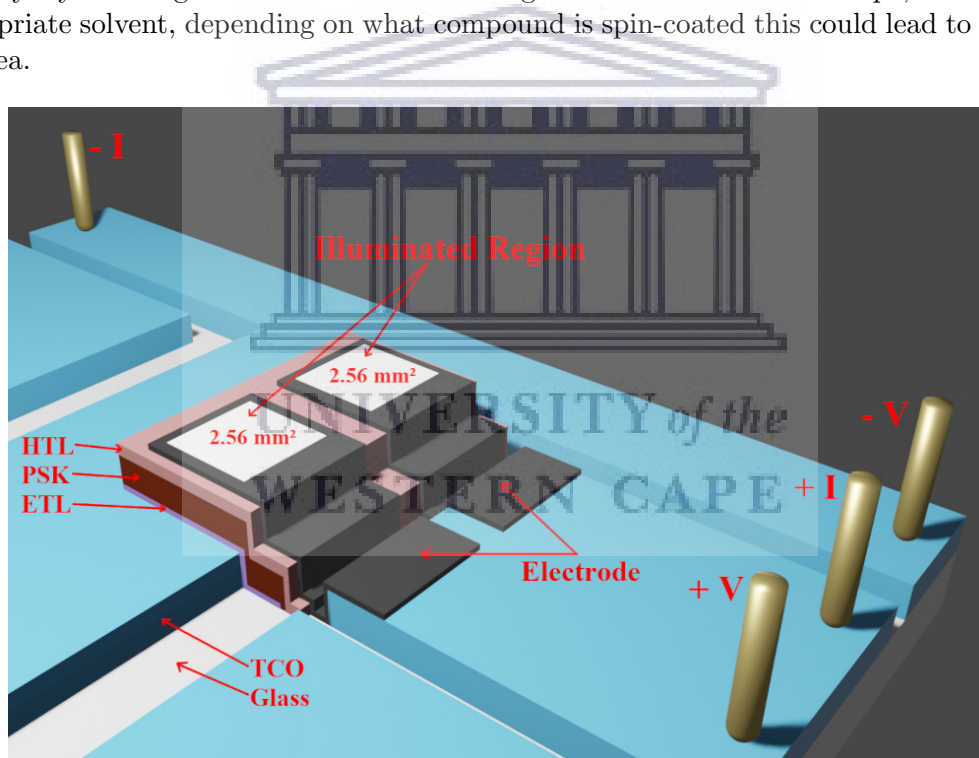
Figure 4.2: Cross-section of single cell of the 4-Wire Design

To conduct IV-characterization a solar cell samples is placed upside down to allow contact between the spring-loaded gold coated pins and the sample's TCO as seen in fig. 4.3(a). The aperture mask is placed on top of the sample and the lid (b) is fastened. The sample is completely masked for dark IV measurements and is placed below the solar simulator which is adjusted to the desired illumination intensity by varying its output power. The intensity is verified by a Daystar Solar meter. The height of the holder was adjusted to ensure that the sample when placed in the holder is the same distance as the Daystar meter to the solar simulator. To select a cell the desired connection is made by toggling a switch (c) either to ground (GND) or positive (BNC). Toggling

a switch completes the connection to either the positive or negative of the BNC connector (d) which is connected to the input of the Keithley 2420 SMU. For inverted architectures either the switches (c) can be reversed or the positive and negative connections from the BNC cable to the SMU can be reversed. To perform a four-wire measurement a separate set of positive and negative connections are selected by connecting two of the output pins (e) to the four-wire input of the SMU.

The output pins (e) can be used to automate the measuring process since a circuit is completed by connecting the pins labelled 1 to 12 to either GND or BNC. By adding a servo controlled shutter the measuring process of Dark and illuminated IV measurements can be made by adding additional commands to the Solar Cell Software. This is especially useful for conducting time consuming stability measurements of each individual cells.
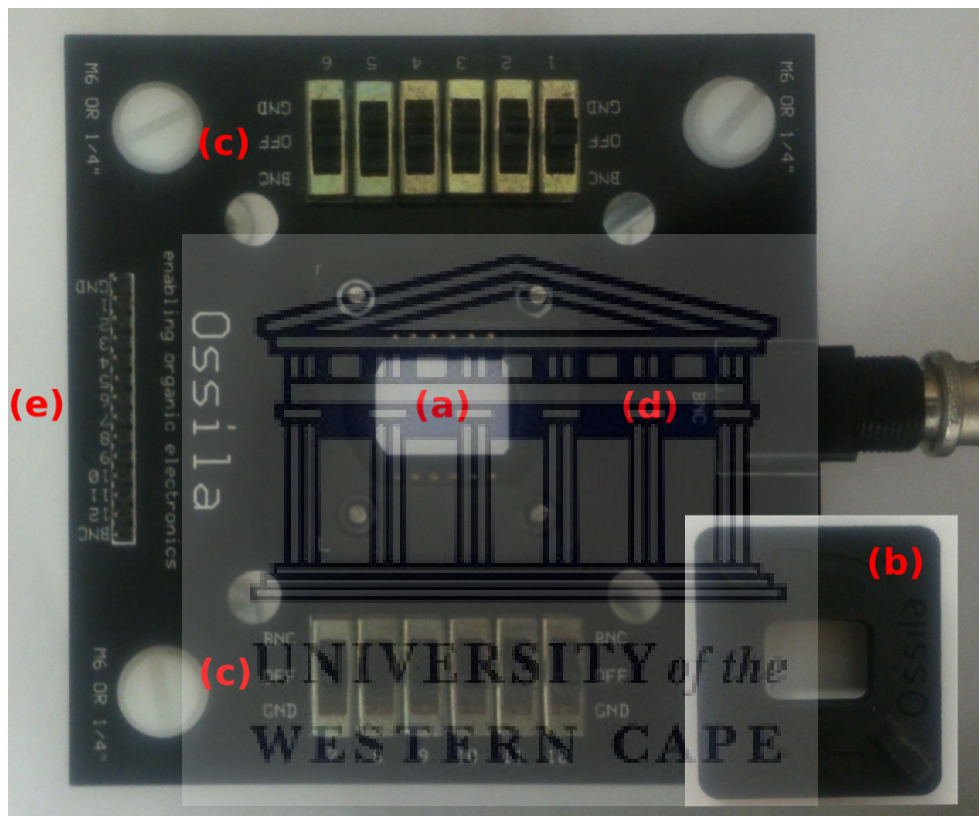
Figure 4.3: Ossila Solar Cell Holder

As mentioned before the solar cell design was limited by the Ossila deposition and aperture mask, fig. 4.4 demonstrates a prototype design of which the CAD model can be made available upon request. This design works with the existing solar cell holder and the active area can still be encapsulated by the glass cover slips. Since the 12 sample deposition mask consists of multiple layers only the top layer was redesigned. The advantage of the new design is that it allows for the possibility of different aperture sizes as demonstrated with the green and red rectangles in fig. 4.4 indicating the 4 and $12mm^2$ illuminated areas. The design also requires a more simplistic TCO etching pattern. The electrodes are deposited up to the position of the holder pins with an additional deposition on the ground to minimize contact resistance. The top and bottom cell connect to 2 positive pins for the option of four-wire measurements. The prototype design also has a large gap between the active area and contact regions to ensure ease of deposition of layers and cleaning without risk of damaging the active area.
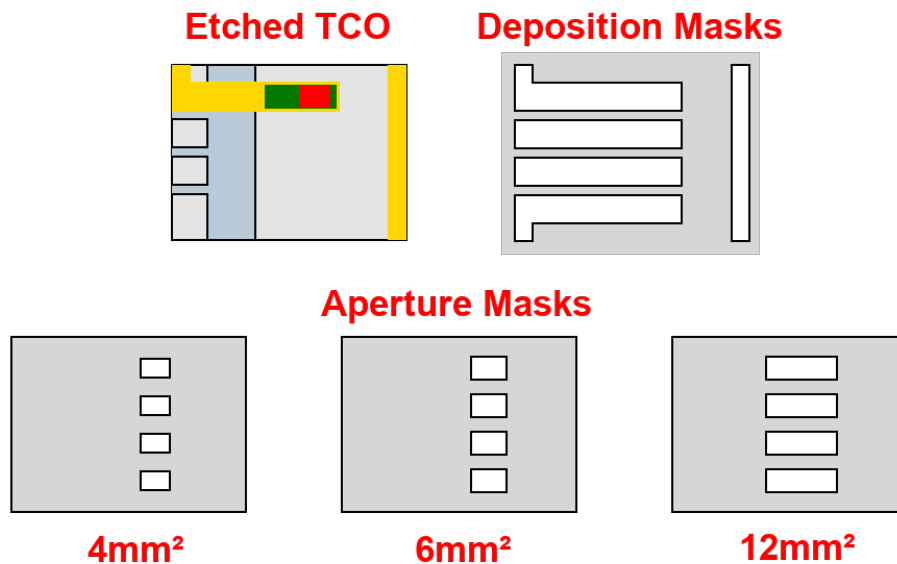
Figure 4.4: Prototype Design

4.2 Device Assembly

The solar cell architecture with superimposed colours can be seen in fig. 4.5 with the use of FTO (Techinstro) (10 Ω/sq) as a TCO with a thickness of 650 nm. The ETL is a 40 nm layer of spin-coated TiO_2 on which a 400 nm $MAPbI_{3-x}Cl_x$ perovskite is deposited via sequential CVD. The HTL is a 200 nm spin-coated layer of Spiro-Ometad. The device is completed with a 90 nm thermal evaporated gold electrode. All other solar cells studied were based on this structure with minor alterations.
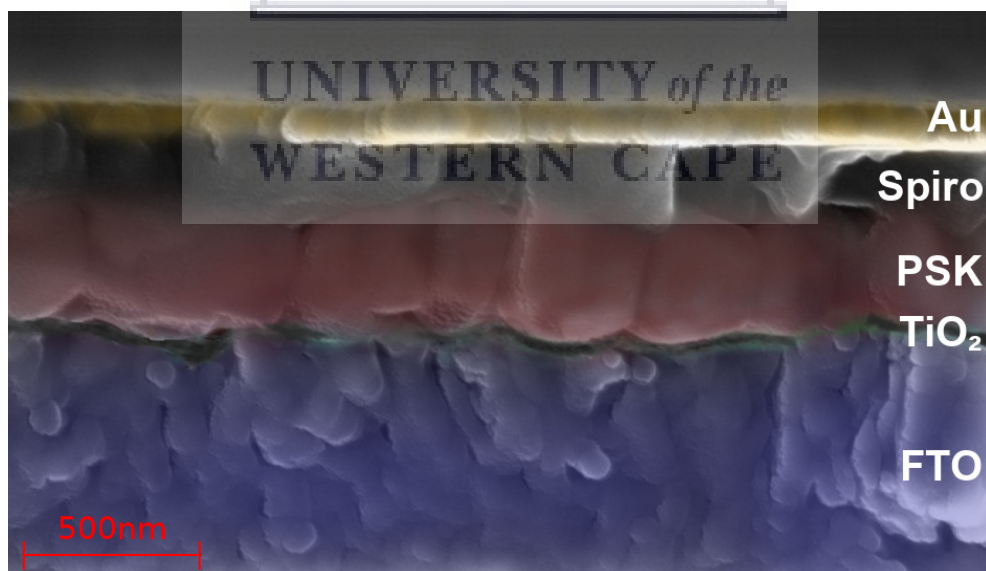
Figure 4.5: Solar Cell SEM Cross Section

The initial goal was to replace TiO_2 with SnO_2 as ETL, to utilize ITO coated glass as the TCO substrate and to achieve a higher stabilised PCE. FTO has a higher thermal stability and is used when annealing temperatures above $400°C$ is required. This was confirmed by four point probe measurements of annealed FTO and ITO (Ossila) in air at $500°C$ for 1 hour. The sheet resistance

of FTO remained constant at 10.2 ± 0.1 Ω/sq and the ITO increased from 9.6 ± 0.1 Ω/sq to 28.3 ± 0.2 Ω/sq, a similar increase has been observed in literature.[110]

Gold is the most widely used electrode for solar cells with a Spiro-Ometad HTL, due to its chemical stability and high work-function of 5.1eV. However, due to its high cost it must be replaced for the commercialization of perovskite solar cells.[111]. Therefore, silver was also used as an electrode.

4.2.1 TCO Preparation

The solar cells consist of a TCO either FTO or ITO. The TCO is cut to a size 15 by 20mm. It is important that the TCO be cut to match these dimensions as precise as possible with a maximum allowed error of 0.1mm. This is to ensure that the samples fit in the measurement (fig. 4.3) and deposition mask holder. The cut TCO is masked with Kapton tape and scribed with callipers to the required patterned, a scalpel is used to cut along the scribed lines and the tape is carefully removed where etching is necessary.

The samples are etched using a 3M HCL solution for FTO and depending on the type of ITO used the concentration can be lowered since the etching rate varies. The exposed regions of the TCO is covered with Zinc powder and excess is tapped of the samples to ensure a thin layer on the surface. The HCL solution is dropped onto the samples and left to etch up to 2 minutes. It is important to ensure that the tape used for masking can withstand the etching process, certain brands of tape do not have suitable adhesions and result in pealing during the etching.

The samples are washed and gently wiped with acetone to remove all traces of tape adhesion. Then the samples are sonicated for 10 minutes in Hellmanix^{TM} solution, rinsed with deionised water, sonicated for 10 minutes in ethanol, rinsed with deionised water and sonicated for a further 10 minutes in deionised water. The samples were dried with a stream of Nitrogen.

4.2.2 ETL Preparation

TiO$_2$ Preparation

The TiO$_2$ layer was prepared by a similar method to Quin et al. (2017) [112] with a slight increase in concentration to ensure a thickness between 30 and 40nm. 200μL of 97% titanium isopropoxide was added to 1ml of 99.9% ethanol and magnetically stirred for 5 minutes until the solution turned from transparent to cloudy white. A separate acidic ethanol solution is prepared by adding 20μL of 2M HCL solution (164μL 37% HCL with 836μL H$_2$O) to 1ml ethanol. The acidic ethanol solution is added drop wise during stirring to the cloudy titanium solution, which returns the solution to transparent. The solution is allowed to stir for a further hour then filtered with a 0.1μm PTFE filter into the empty vial that was used to prepare the acidic ethanol solution.

Since the titanium solution dries rapidly during the spin-coating to an insoluble layer the edges of the FTO that exclude the active area are masked with Kapton tape ensuring to leave a 1mm gap between the tape and the edge of the active area to prevent an undesirable build-up of material on the edge. 30 μL of solution is statically spin-coated at 3000 RPM for 30 seconds. The tape is removed and the samples are dried on a hot plate at 80°C for at least 5 min., which is slightly above the boing point of ethanol. The samples are annealed at 500°C for 1 hour in air to fully oxidise the samples with a ramp rate of 10°C/min. The adhesive of the Kapton tape can remain on the FTO especially if heated, hence the tape is removed before drying, the adhesive can also be removed with chlorobenzene.

Since the thin film are insoluble in ethanol sequential layers can be deposited after drying without the need to anneal each layer. It is important to use a new micropipette for each sample since the solution dries in the tip to form insoluble particles that can contaminate the titanium solution

and result in undesirable particles in the thin film that can negatively affect the deposition of other layers. The solution can be used for several days when sealed in a air tight vial, but it is recommended to filter before use.

As a test the solution was also prepared by adding the $200\mu L$ titanium isopropoxide directly to a 2ml acidic ethanol. The solution remained transparent and spin-coated the same as before. However when drying the TiO_2 layer on FTO, large defect immediately formed. Spin-coating on glass formed a smooth uniform layer. TTIP is known to undergo hydrolysis to form TiO_2 [113]:

$$Ti(OCH(CH_3)_2)_4 + 2H_2O \rightarrow TiO_2 + 4(CH_3)_2CHOH \tag{4.2}$$
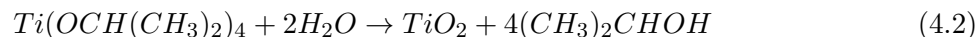
Solvents can absorb moisture from the air, thus, even if anhydrous Ethanol or IPA is used as a solvent[114], once the containers are exposed to air, moisture begins to be absorbed, due to its hygroscopic nature, hence HCL is used to stabilize the solution. It appears that a small amount of hydrolysis of TTIP, which creates TiO_2 nanoparticles is beneficial during the spin-coating to form smooth uniform TiO_2 thin film on FTO.

SnO_2 Preparation

The initial objective was to replace TiO_2 with SnO_2 since it has been well documented to be a superior material for the planar perovskite solar cell architecture (see chapter 1). However, the only precursors that was available were $SnCl_2$ and $SnCl_4 \cdot 5H_2O$ both of 98% purity from Sigma-Aldrich. The SnO_2 thin films incorporated in the solar cells resulted in very poor performance. It is recommended to use the most commonly used precursors, colloidal SnO_2 from Alpha Aesar and $SnCl_2 \cdot 2H_2O$ with the addition of UV-Ozone treatment.

The SnO_2 layer was prepared by two different methods. The First method consisted of a 0.3M $SnCl_2$ solution in 2ml ethanol, $10\mu L$ of 2M HCL was added after 5 min. of stirring. The solution was stirred for a further 2 hours at 40°C then filtered with $0.1\mu m$ PTFE filter. The $SnCl_2$ at room temperature required up to 12 hours to be completely dissolved, hence the need for an elevated stirring temperature. The FTO was covered with Kapton tape as explained in the TiO_2 preparation. Samples were dynamically spin-coated at 4000 RPM for 30 seconds by dropping $30\mu L$ of solution. The samples were dried at 80°C for 10 mins., then annealed at 450°C for 1 hour in air with a ramp rate of 10°C/min.

A test to confirm if a solution is completely dissolved is to shine a light through the vial, this makes particles more visible since it scatters the light. The addition of HCL did not seem to have any effect on the solution, since there was no indication of hydrolysis with the solution becoming clear and stable even without the addition of HCL, this could be due to the absence of the dihydrate. During testing to verify oxidation the samples were swabbed with ethanol after annealing, since SnO_2 is insoluble in ethanol once oxidized prepared thin films could not be removed. The oxidation process required temperatures above 250°C. Fig. 4.6 demonstrates the crystallinity of the spin-coated SnO_2 on glass, preventing overlapping peaks if characterization was done on FTO. Complete XRD analysis can be found in appendix B.6. The thin films also had a low resistivity which varied between 0.1 and 5 Ω·cm, which is within the typical range for SnO_2.[115]. The resistivity was significantly lower than the TiO_2 thin films which were beyond the measuring capability of the four point probe (resistivity $> 10^4$ Ω·cm).
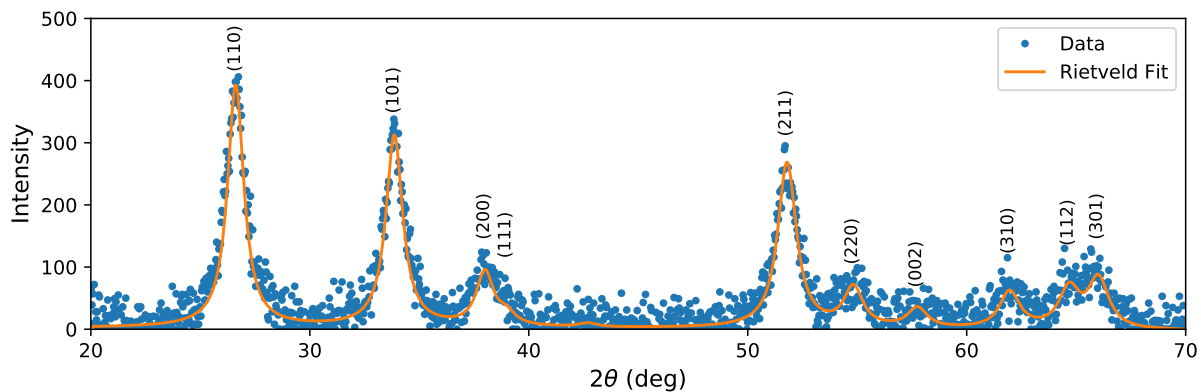
Figure 4.6: SnO$_2$ XRD

The second method used 0.05M SnCl$_4$·5H$_2$O dissolved in IPA which is spin-coated onto FTO at 3000 RPM for 30 seconds. The samples were dried on a hot plate for 10 minutes at 80°C and further annealed at 180°C for 1 hour, resulting in a 3 to 5 nm thin film. This method was successfully used by Matsui et al. (2016) to achieve a PCE of nearly 20% by also using UV-Ozone treatment to improve spin-coating.[116] Ganchev et al. (2019) obtained a thickness of 5nm with a similar method and relied on multiple spin-coating to increase thickness[117]. However, this could not be reproduced, since the solution had low wettability on smooth surfaces. The solution concentration was increased to 0.1M and 0.2M, which resulted in incomplete coverage. Ethanol had also been attempted as a solvent with similar results. The addition of 10μL of 1M HCL also had no noticeable effect. Since it is recommended that the ETL thickness be between 20 and 30 nm [118], the thin SnO$_2$ ETL lead to poor performance. (see table 4.5)

4.2.3 Perovskite Preparation

The perovskite layer was deposited via sequential CVD. The First layer consists of a 130 ± 5 nm of PbCl$_2$, deposited by evaporating 31 mg of PbCl$_2$ powder at 420°C for 15 minutes with N$_2$ flow rate of 500 sccm at a working pressure of 4 mbar. The samples were removed and the conversion was done by evaporating 60 mg of MAI powder at 160°C for 1 hour with a substrate temperature of 120°C and a N$_2$ flow rate of 100 sccm providing a working pressure of 1mbar. The full description can be found in chapter 3.

Solution processing was also used to test the effectiveness of PCBM as an interface layer between the TiO$_2$ and perovskite for improved band alignment. The reason is that during the deposition of PbCl$_2$ the substrate reach temperatures up to 140°C which was confirmed to damage the PCBM layer due to a small amount of evaporation at temperature above 100°C at 4mbar pressure, mostly occurring around the edges of the sample with the centre remaining unchanged (appendix A.1).

For a one step solution deposition 1M PbI$_2$ and 1M MAI was dissolved in 0.5ml DMF and stirred at 60°C for 2 hours, then filtered with a 0.1μm PTFE filter. The substrates were heated at 100°C and immediately transferred to be dynamically spin-coated at 3000 RPM for 30 seconds, which is referred to as hot-cast spin-coating which is to improve the quality of the films when working in humid environments.[119] The samples were annealed in air for 10 minutes at 100°C.

The other method was to deposit 150nm layer of PbI$_2$ via spin-coating by preparing a 0.8M solution of PbI$_2$ in DMF. The solution was stirred at 70°C for two hours. It is important to have a vial that has an air tight seal to avoid evaporation of the solvent. The solution is filtered which removes all undissolved particle. Samples were spin-coated in the same hot-cast method as before. The samples are converted using the same CVD procedure.

The one step method resulted in poor quality perovskite with noticeable defects resulting in a porous thin film, filled with voids that did not result in working solar cells. The PbI_2 layer resulted in dense films with a uniform smooth surface, which had a significantly improved morphology compared to room temperature spin-coating. The filtering also made a large improvement since without filtering there were several particles on the surface. It is important to remove these particles since the CVD conversion requires a smooth surface. MAI vapour tends to accumulate at the PbI_2 particles resulting in weak points in the film where moisture can easily accumulate and accelerate the degradation of the perovskite.

As a post treatment, 30 μL of IPA was dynamically spin-coated onto the perovskite at 6000 RPM for 60 seconds. The samples were then annealed at 100°C for 10 minutes in air.

4.2.4 Spiro-Ometad (HTL) Preparation

Most perovskite solar cells in literature use the following solution concentration which will be referred to as the standard solution: 72.3 mg/ml of Spiro-Ometad dissolved in anhydrous chlorobenzene (CB), separately 520 mg/ml LiTFSI is dissolved in acetonitile (ACN) and 17.5μL of the LiTFSI solution as well as 28.8μL tBP is added to the Spiro-Ometad solution this provides a molar ratio of 1.85:6.2:1 (Spiro:tBP:LiTFSI).

The thickness at different spin speeds were first tested on perovskite thin films using the standard solution with and without dopants. All spincoating of Spiro-Ometad was done for 30 seconds with a clear change in thin film interference for the first 5 seconds as the thickness decreases. The measurement were averaged from 3 different positions as measured by the Dektak profilometer as seen in table 4.1. The thickness of the undoped Spiro-Ometad was on average 5% less thick than the doped with more uniform thickness at higher spin speeds. Static spin-coating resulted in thicker films which coincides with the findings of Wang et al. (2020).[120] The thickness was considerably thinner in comparison to most work in literature, where the thickness is greater than 200nm for dynamic spinning at 3000 RPM or even 4000 RPM with the standard solution. However, similar thicknesses were obtained by Marinova et al. (2015).[121]

Table 4.1: Thickness (nm) of Standard Spiro-Ometad Solution

Speed (RPM)	Doped	Undoped
6000	108 ± 7	102 ± 3
4000	117 ± 6	111 ± 4
3000	142 ± 7	133 ± 8
2000	187 ± 10	176 ± 10
2000 (static)	240 ± 20	230 ± 20

The spin-coating of the doped solution lead to the formation of large particles on the surface of the Spiro-Ometad film as seen in fig. 4.7 which compares the surface of doped and undoped films spin-coated dynamically at 2000 RPM. The solutions were filtered with a 0.1μm PTFE filters after 1 hour of stirring, thus, the particle formation must occur during the spin-coating, the most likely cause is the agglomeration of the highly hygroscopic LiTFSI while spin-coating in a relative humidity of 70%. The preparation of the solution and spin-coating should be performed in a glovebox without exposing the materials to air.[118]
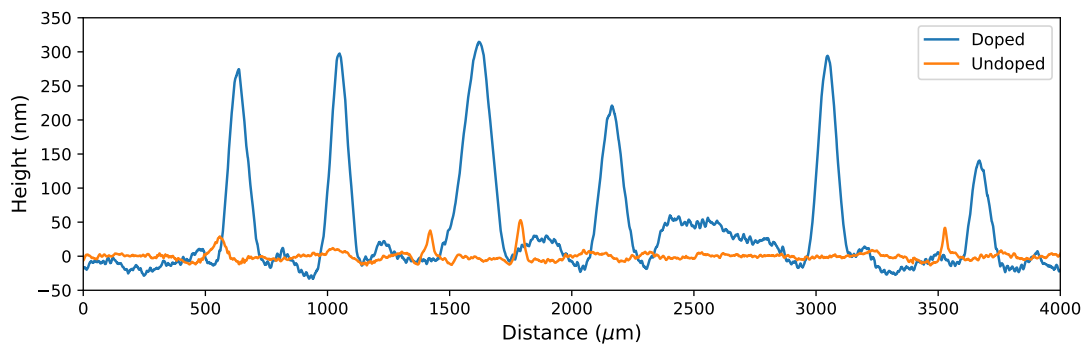
Figure 4.7: Surface Profile of Spiro-Ometad on Perovskite

Spiro-Ometad thin films are often left to oxidize in a low humidity environment to improve the PCE. A study by Liu et al. (2018) concluded that the average PCE increased by 18% after 24h oxidization in pure oxygen compared to no oxidation. Further oxidation lead to a decrease in PCE due to the degradation of the perovskite [122]. The oxidation process of Spiro-Ometad with LiTFSI leads to an increase in absorbance and conductivity. The same doped and undoped solutions were spin-coated on glass coated with 20nm of $PbCl_2$ via CVD, this is to ensure increased wettability, whilst maintaining low absorbance due the large bandgap of 5eV of $PbCl_2$.[106]. It is also important that the substrate have a higher resistivity than Spiro-Ometad, to obtain an accurate four point probe measurements.

Samples were oxidized in a desiccator with a relative humidity of 15%. The sheet resistance of the undoped Spiro-Ometad was beyond the measuring capability 10^{10} Ω/sq and therefore, had a resistivity greater than 2×10^5 Ω.cm. The doped samples had an average resistivity of 6 ± 1 Ω.cm immediately after spin-coating which remained unchanged after oxidation. The absorbance measurements which were determined by A = 1 - (R + T) demonstrates a continues oxidation process even 20 days after spin-coating with increase in absorbance of wavelengths longer than the bandgap of Spiro-Ometad of 3eV (413nm).[123][124]
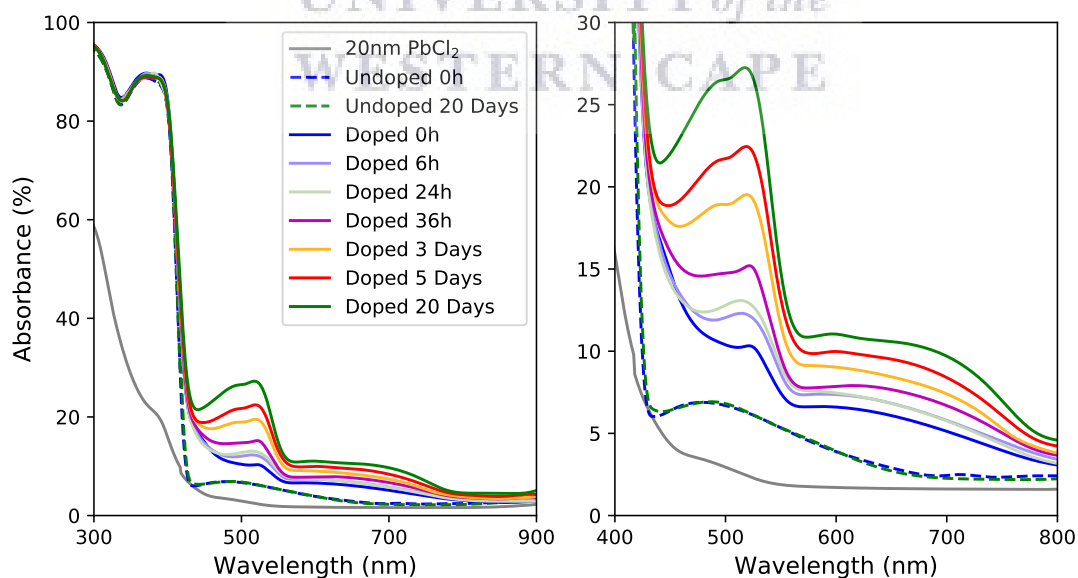
Figure 4.8: UV-Vis Absorbance of Spiro-Ometad on $PbCl_2$ with Magnified Region

Since the LiTFSI was not stored in a glovebox the powder was dried in a vacuum (1 mbar) furnace

at 80°c for 5 hours, by placing a 52 mg in an unsealed vial. After drying 100ml of 99.9% IPA was added to the vial. IPA was used as a replacement for ACN since it can damage the perovskite surface.[125]. To increase the thickness of the Spiro-Ometad the concentration was increased to 80 mg/ml with the addition of 24μL tBP and 18μL LiTFSI solution, providing a molar ratio of 2:5:1 (Spiro:tBP:LiTFSI), which will be referred to as the modified solution. Static spin-coating at 2000 RPM resulted in an average thickness of 260 ± 20 nm with similar particles on the surface as the standard doped solution. All cells were left in a desiccator for 12 hours before thermal evaporation of the electrodes.

4.3 IV Results

The first batch of solar cells consisted of either TiO_2 or SnO_2 ($SnCl_2$ precursor) spin-coated on FTO with CVD $MAPbI_{3-x}Cl_x$ perovskite. The Spiro-ometad was dynamically spin-coated with 30μL at 2000 RPM from the standard solution doped and undoped. A 90nm layer of gold was thermally evaporated at a pressure of $5x10^{-4}$ mbar. The temperature of the sample holder as measured via a k-type thermocouple after the deposition was 55°C. Thus, the samples could have exceeded the recommended highest temperature of 60°C during the 10 minute deposition of the gold electrodes which is known to reduce the performance of perovskite solar cells.[118] Samples were encapsulated with a glass cover slip and epoxy (Ossila).

All 8 solar cell samples (4 cells per sample) with Sno_2 as ETL had a PCE below 0.1%. Unfortunately, only four samples were made of TiO_2 (2 doped, 2 undoped) providing a small data set yet all the cells had a PCE above 1.2% as seen in fig. 4.11. The samples with gold did produce the highest V_{oc} of 0.976V which is still significantly lower than the 1.1V that has been achieved with a similar solar cell architecture. [126]

The second batch of samples focused on the different thicknesses of undoped Spiro-Ometad using 72.3mg/ml concentration. Only TiO_2 was used as an ETL and the gold was replaced with silver to reduce the substrate temperature during the deposition. The substrates holder after the deposition reached 25°C. The spin-speed was varied between 3000 and 6000 RPM. All cells showed low fill factors with an IV-curve with nearly straight lines from the J_{sc} to the V_{oc}. There was no significant difference in PCE of the cells with all samples having cells that range in PCE between 1.2% and 4.2%, mostly due to the fact that there was no significant difference in thickness at different spin speeds. This was later verified with average thicknesses seen in table 4.1. The thicknesses were between 100nm and 140nm not ideal for undoped Spiro-Ometad which should be less than 70nm to ensure sufficient hole transportation through the less conductive HTL.[127] The TiO_2 thickness was also increased to 80 nm, with no significant change in PCE.

The third batch consisted of samples made using the standard doped Spiro-Ometad solution dynamically and statically spin-coated at 2000 RPM and 4000 RPM with a silver electrode. All cells had the same TiO_2 ETL and CVD Perovskite as previous. All cells resulted in low PCE less than 3% with the highest V_{oc} at 0.62 V. The cells were also highly unstable and rapidly degraded after the first few repeated measurements, with visible formation of silver spots penetrating trough the Spiro-Ometad and Perovskite layers as seen in fig. 4.9. The cells with silver spots did no longer function due to very low shunt resistance which reduces the J_{sc} to zero. Cells that were spin- coated at 4000 RPM were the most unstable with most cells producing no current or only producing between 0.5 and 1.5% efficiency for the first measurement and then no current by the second measurement.
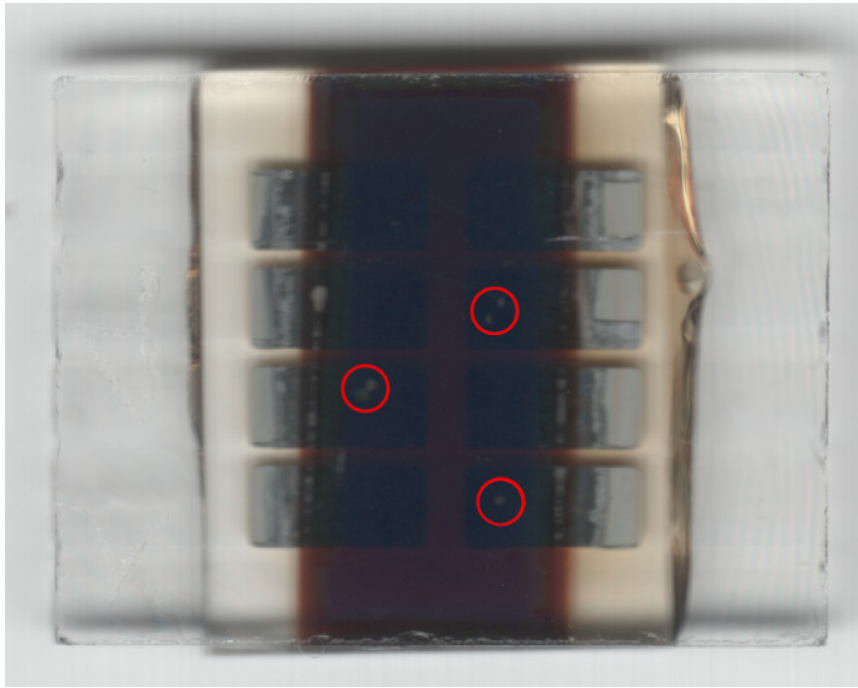
Figure 4.9: Silver Penetration Through Solar Cells marked in Red

The fourth batch of samples were made the same as batch 3, except for the Spiro-Ometad that was spin-coated using the modified solution as mentioned in the preparation section. These cells had a significant improvement in efficiency and stability. However, even the most stable cell degraded after a few days with encapsulation as seen in figures 4.14 and 4.15. Unencapsulated cells degraded to less than 10% of its initial PCE within 12 hours after being stored in a desiccator.

The IV-curves of all the cells with the highest PCE for the different architectures can be seen in fig. 4.10. The labels refer to doped or undoped Spiro-Ometad and the use of either gold or silver as electrode. Due to the much larger fill factor the Doped Spiro-Ometad and silver electrode architecture provided the highest efficiency using static spin-coating at 2000 RPM, which provided the thickest layer creating the largest barrier between the Perovskite and silver electrode. Despite the high deposition temperature during the gold deposition the cells had the largest V_{oc}. All cells with silver electrodes had a much lower V_{oc} than the typical 1 to 1.1V that is obtained with a similar architecture in literature. The s-shape cure which is discussed in chapter 4.4, is a clear indication that energy levels are not properly aligned in the silver solar cells reducing the transport of holes at the interface between the Spiro-Ometad and silver. All cells experienced a significant hysteresis which can be caused by several different factors predominately due to mobile ions in perovskite layer migrating into transport layers, which is common for the n-i-p architecture.[128] However, the amount of defects in the Spiro-Ometad can also give rise to an increase in hysteresis.[120]
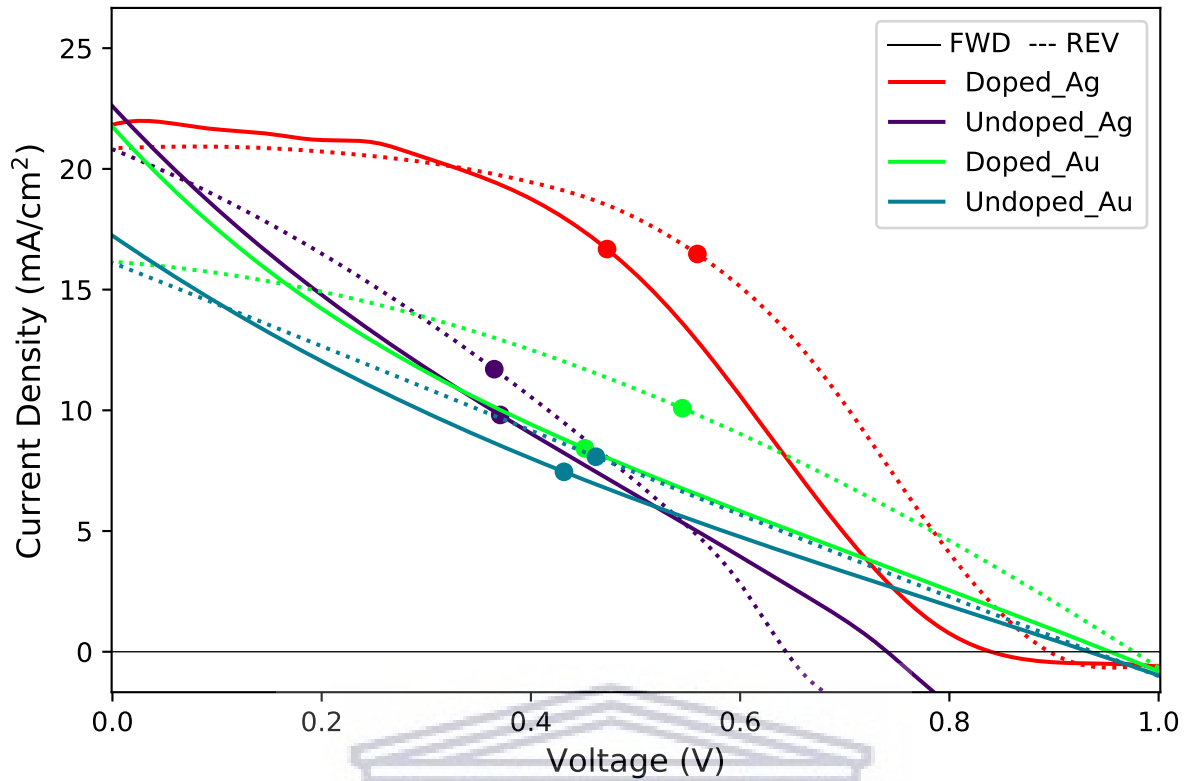
Figure 4.10: Highest PCE Cells with CVD Perovskite

Table 4.2: Highest Efficiency Cells of Different Architectures

Solar Cell Type	Direction	J_{sc} (mA/cm^2)	V_{oc} (mV)	FF (%)	PCE (%)	HI (%)
Doped Spiro, Ag	FWD	21.83	840	43.03	7.89	14.33
	REV	20.85	895	49.33	9.21	
Undoped Spiro, Ag	FWD	22.59	741	21.73	3.64	14.75
	REV	20.81	644	31.88	4.27	
Doped Spiro, Au	FWD	21.75	954	18.34	3.80	30.91
	REV	16.15	976	34.83	5.50	
Undoped Spiro, Au	FWD	17.23	934	20.00	3.22	13.67
	REV	16.11	938	24.71	3.73	

The performance of the different architectures were averaged over multiple cells with individual data points plotted in fig. 4.11. The cell architecture consisted of the same 30 to 40nm compact TiO$_2$ layer spin-coated onto FTO and annealed at 500°C for 1 hour and 400nm sequential CVD MAPbI$_{3-x}$Cl$_x$ perovskite. The silver and gold electrode were thermally evaporated with a thickness of 150 and 90 nm, respectively. The undoped Spiro-Ometad was a 100 to 110 nm spin-coated layer with a 72.3 mg.ml^{-1} concentration, the "Doped Au" samples used the standard Spiro-Ometad solution dynamically spin-coated at 2000 RPM and the "Doped Ag" samples were statically spin-coated at 2000 RPM from the modified solution (chap. 4.2.4).

Table 4.3: Average Performance of Different Architectures

Solar Cell Type	Direction	J_{sc} (mA/cm^2)	V_{oc} (mV)	FF (%)	PCE (%)	HI (%)
Doped Spiro, Ag	FWD	18 ± 3	720 ± 60	33 ± 7	4 ± 2	30 ± 40
	REV	14 ± 5	770 ± 70	48 ± 6	6 ± 2	
Undoped Spiro, Ag	FWD	17 ± 3	690 ± 50	19 ± 3	2.4 ± 0.8	10 ± 40
	REV	16 ± 3	600 ± 40	29 ± 3	2.8 ± 0.9	
Doped Spiro, Au	FWD	16 ± 3	950 ± 30	16 ± 2	2.5 ± 0.8	40 ± 40
	REV	14 ± 2	970 ± 30	28 ± 4	4 ± 1	
Undoped Spiro, Au	FWD	13 ± 2	930 ± 20	20 ± 1	2.5 ± 0.8	10 ± 30
	REV	13 ± 1	940 ± 20	24 ± 2	2.9 ± 0.4	
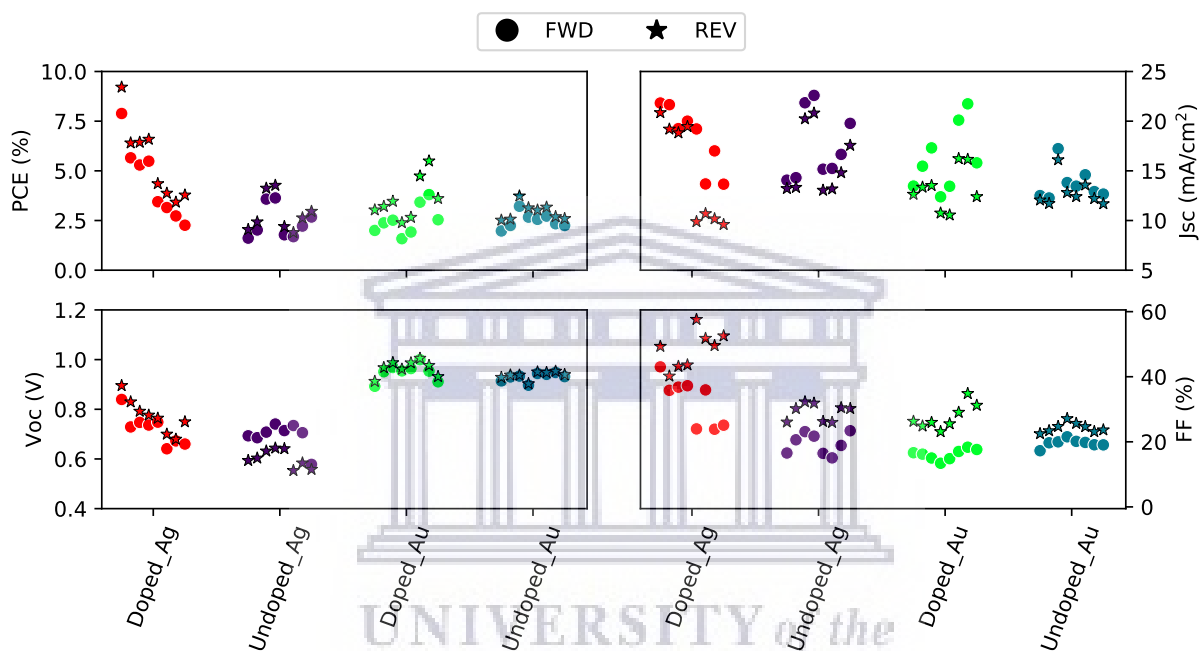
Figure 4.11: Individual Solar Cell Results

To achieve the highest measurable efficiency the cells are light soaked for 2 minutes before measuring at a high scan rate of 1000mV/s. However, this is not a true representation of the performance of the solar cell since it would need to maintain a maximum power output for several hours a day under real world conditions. Since many researchers do not include scan rate values and stabilised efficiency measurements, it is important to perform IV measurements with high scan rates to compare results from literature.

When the scan rate is decreased the amount of current also decreases due to a build-up of charge at the perovskite TiO$_2$ interface leading to a large capacitance due to energy band misalignment.[129]. Forward and reverse scan directions are also dependent on scan rates which give rise to varying amounts of hysteresis. The cell with the highest PCE with doped Spiro-Ometad and silver electrodes were used to demonstrate the effect of scan rate and stabilised efficiency, but all cells exhibited the same effect with varying amounts including cells with gold electrodes.

The time dependent decrease in current density can be seen most prominent at 100 mV/s which takes 10 seconds to complete a scan with the forward scan measured first. The forward scan has a high J$_{sc}$ which quickly decreases, resembling a solar with a low shunt resistance however this

is not the cause and rather due to the capacitance within the cell, demonstrating that the diode model can not provide an accurate representation of the cells. The reverse scan at 100 mV/s even demonstrates an increase in current from its J_{sc} towards the maximum point. At 10 mV/s the cells reach a steady state before its maximum point, providing a current density in both forward and reverse scans similar to the stabilized measurements seen in fig. 4.13.

The impact of replacing TiO_2 with SnO_2 using atomic layer deposition (ALD) was studied by Pablo et al. (2015).[129] The SnO_2 ETL provided a PCE of 19.5% at 1000 mV/s and decreased to 18.4% at 10 mV/s (5.6% decrease), by only replacing the ETL with TiO_2 the PCE was 9.5% at 1000 mV/s and decreased to 5.9% at 10 mV/s (38% decrease). The $(FAPbI_3)_{1-x}(MAPbBr_3)_x$ mixed perovskite was used. However, a similar decrease in PCE was obtained for the $MAPbI_3$ based solar cells with a TiO_2 ETL, no interface or mesoporous layers were used in the study. UPS studies revealed that the conduction band minimum (CBM) of TiO_2 was 0.08 eV above the CBM of $MAPbI_3$ and 0.3eV of the mixed perovskite. The CBM of SnO_2 was lower than both perovskites allowing electrons to be transported more freely.

In a different study a compact layer of TiO_2 via spray pyrolysis was used to achieve a PCE of 19.1% with a scan rate of 50 mV/s and a stabilised PCE of 18.8% (2 minutes at 0.93V). The perovskite was spin-coated from a purified $MAPbI_{2.91}Cl_{0.09}$ powder to achieve a highly uniform distribution of chloride.[130]. The incorporation of chloride is known to shift the CBM. Therefore, it is possible achieve the appropriate energy band alignment.[131]
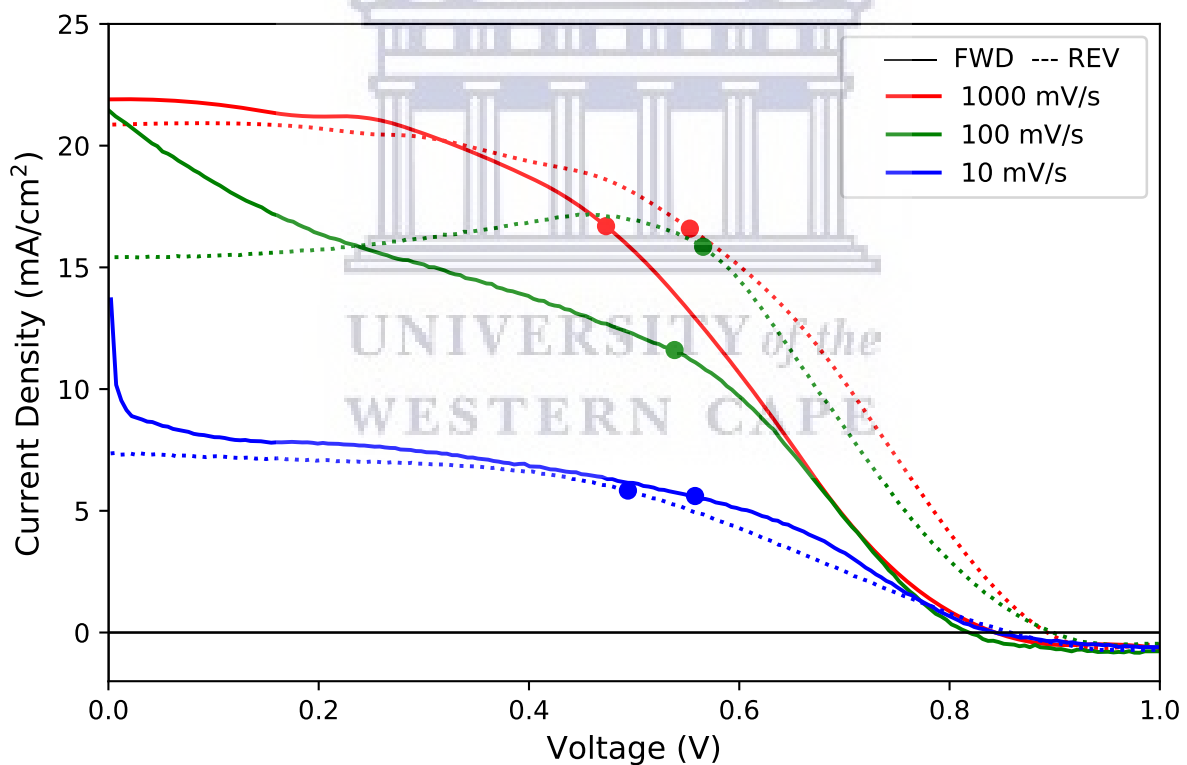
Figure 4.12: IV Measurements at Different Scan Rates

Three stabilised measurements were performed on the same cell as seen in fig. 4.13 illuminated at 1000W/m^2, the first with a zero-volt bias after light soaking for 2 minutes before performing the measurement leading to a rapid decrease in current density during the first 10 seconds. The cell was then placed in the dark for 2 minutes and the zero-volt bias was applied before being illuminated, resulting in a increase in current density. A shutter was used which results in zero

Table 4.4: Performance at Different Scan Rates

Scan Speed (mV/s)	Direction	J_{sc} (mA/cm^2)	V_{mp} (mV)	V_{oc} (mV)	FF (%)	PCE (%)	HI (%)
1000	FWD	21.83	473	840	43.03	7.89	14.33
	REV	20.85	553	895	49.33	9.21	
100	FWD	21.46	539	819	35.57	6.25	30.25
	REV	15.85	566	898	64.72	8.96	
10	FWD	17.53	558	843	21.16	3.13	8.68
	REV	7.35	494	858	45.69	2.88	

current generation. After the shutter was removed it took on average 3 seconds to reach 99% of the maximum stabilised current density. The stabilised zero-volt bias provided similar current density to the 10 mV/s scan rate indicating the importance of slow scan rates for accurate representation of solar cell performance.

There was a slight decrease in current density at zero volt with extended light exposure which is probably caused by a slow degradation within the cell. However, the degradation was more pronounced when applying a 0.5 V bias near the maximum point of the cell. The stabilised PCE decreased from 2.7% to 2.1% after nearly 1 minute of exposure. The cell was placed in the dark for 10 min before performing a reverse scan at 1000 mV/s and 10 mV/s However, the cell performance had degraded, resulting in a PCE of 5.45% and 1.94% at the respective scan rates, significantly lower than what was achieved prior to stabilised measurements (table 4.4).
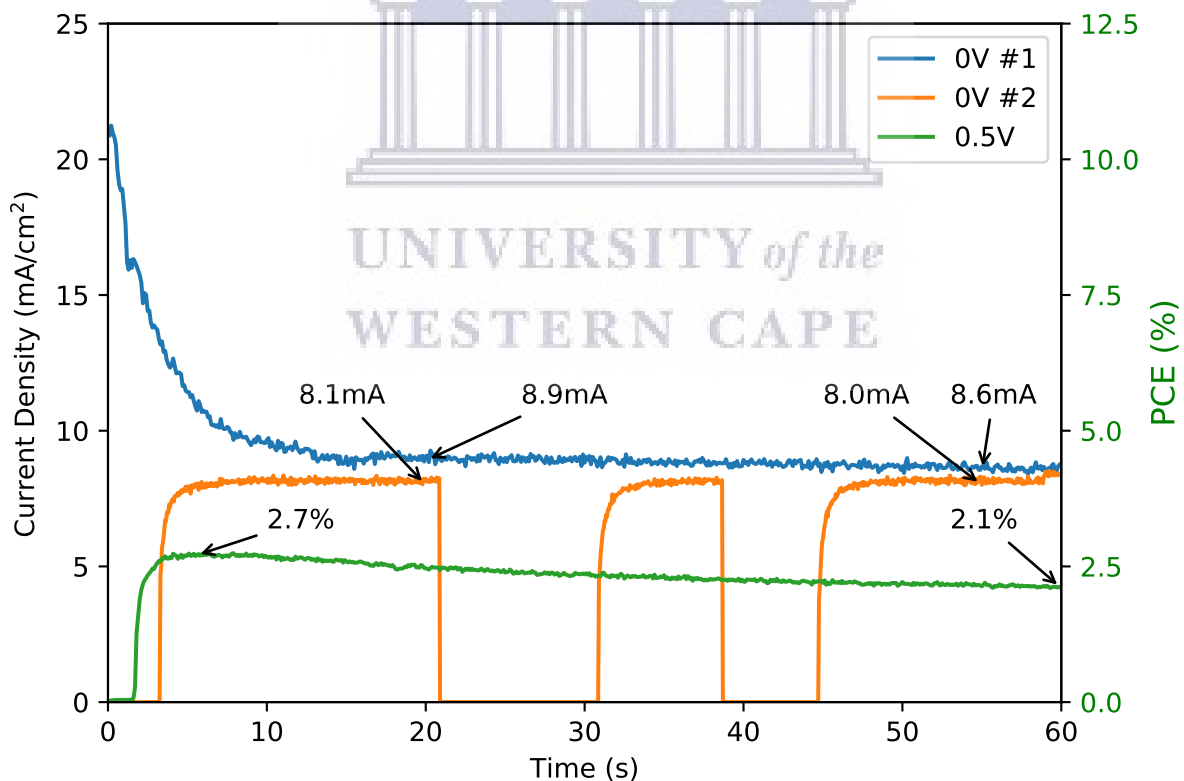
Figure 4.13: Stabilized Measurements

In order to monitor the degradation over time, a cell from a different sample was used. The sample was encapsulated and stored in a desiccator in the dark. Light soaking of 2 minutes was

performed prior to measuring at a scan rate of 1000 mV/s to prevent the cell from degrading during long measurement durations. The initial reverse scan performance was as follows: PCE 7.71%, J_{sc} 20.45 mA/cm^2, V_{oc} 823 mV and a FF of 45.8%. The forward values were: PCE 6.82%, J_{sc} 20.99 mA/cm^2, V_{oc} 855 mV and a FF of 40.0%. The degradation over a period of 7 days can be seen in fig.4.14 with normalised performance values seen in fig. 4.15. Even with encapsulation the cell degraded to 20% of its initial PCE after 3 days. The cell was not measured between the third and seventh day. Encapsulated cells have no visual signs of degradations even after 30 days exposed to air, as seen in fig. 4.16. The particles on the Spiro-Ometad surface are not visible on encapsulated samples, due to the thick epoxy layer.
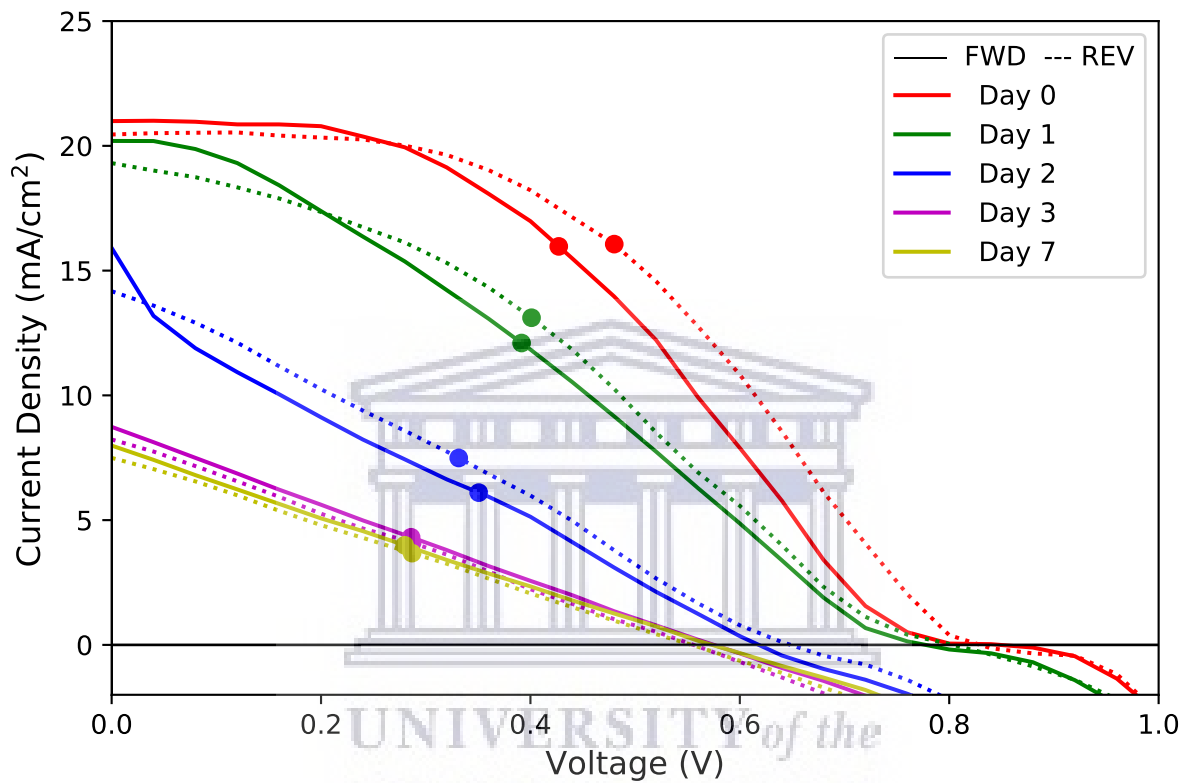
Figure 4.14: Degradation of Encapsulated Solar Cell
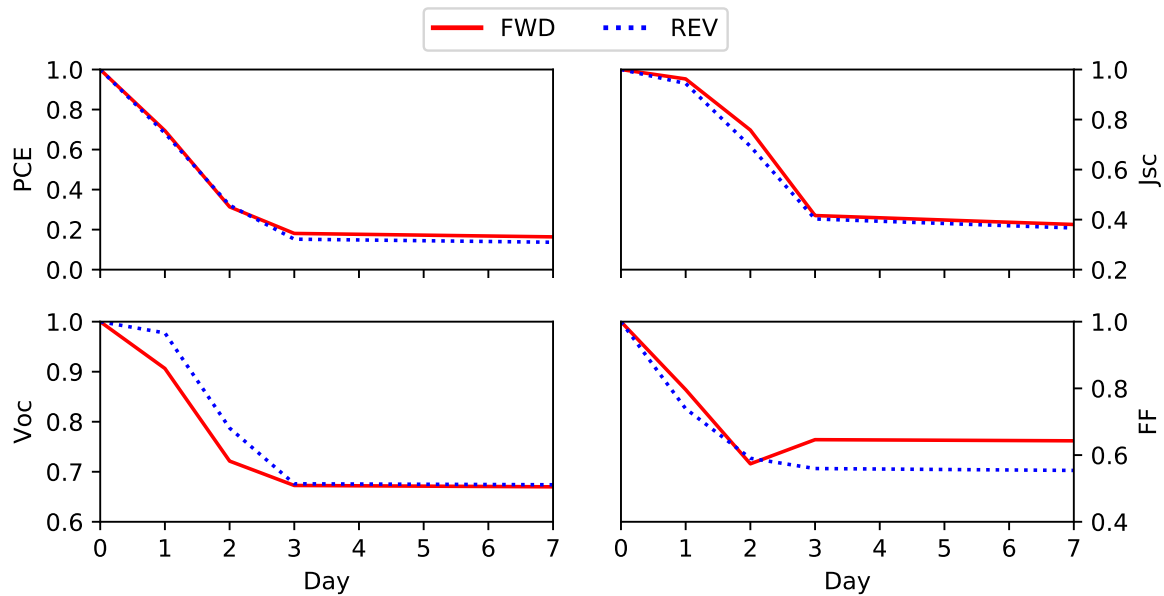
Figure 4.15: Normalised Degradation

Figure 4.16: 30 Days Air exposed (60-80% RH) (a)Unencapsulated and (b)Encapsulated Sample

Table 4.5 demonstrates the highest PCE achieved with alternative architectures, the first three cell types are from the first batch of samples were gold was used as electrode, the last 3 types were from the fifth batch of samples, with the 1-step solution perovskite samples being excluded due to poor performance with PCE < 0.01%. The fifth batch used the modified Spiro-Ometad solution and silver electrodes. "CVD PSK" refers to the standard sequential CVD method (chap. 4.2.3 and "Sol PSK" are samples with spin-coated PbI_2 that were converted to perovskite as normal with CVD. The spin-coated Pb_2 layer was used since it prevents PCBM from damaging during the high substrate temperatures of vapour deposition of $PbCl_2$ (see appendix A.1). It also provided a test to verify the quality of the spin-coated PbI_2 layer for conversion to perovskite, used in a solar cell.

Despite the SnO_2** ETL having a thickness less than 5 nm, it did provide a significant improvement compared to the ETL free solar cells. The average reverse PCE from 8 cells of the TiO_2/Sol PSK type was $3 \pm 2\%$ and the TiO_2/PCBM/Sol PSK type was $5 \pm 2\%$.

Table 4.5: Performance of Alternative Architectures

Solar Cell Type	Direction	J_{sc} (mA/cm^2)	V_{oc} (mV)	FF (%)	PCE (%)	HI (%)
ITO[†]/CVD PSK	FWD	1.12	287	28.3	0.09	10
	REV	0.98	323	32.2	0.10	
FTO[†]/CVD PSK	FWD	0.45	138	36.2	0.02	50
	REV	0.37	203	17.8	0.01	
SnO$_2$*/CVD PSK	FWD	2.53	167	17.8	0.08	86.9
	REV	5.86	419	24.9	0.61	
SnO$_2$**/CVD PSK	FWD	20.90	437	12.2	1.10	62.2
	REV	11.10	634	40.5	2.91	
TiO$_2$/Sol PSK	FWD	18.32	750	29.2	4.01	23.9
	REV	17.34	783	38.8	5.27	
TiO$_2$/PCBM/Sol PSK	FWD	19.53	796	45.7	7.10	5.5
	REV	19.21	789	44.3	6.71	

*Method 1: SnCl$_2$, **Method 2: SnCl$_4$·5H$_2$O, [†]ETL Free solar cell

4.4 Comparison to Similar Research

The purpose of a solar cell is to harness as much energy from the sun while maintaining long-term stability. The solar cell in this research has not succeeded in this task. Therefore, it is important to investigate the potential failure points that hinder performance in order to make the necessary alterations. Several research groups have achieved stable efficiencies with methylammonium based solar cells in excess of 20%.[ref] To achieve this level of performance each component of the solar cell must be meticulously optimised, since a single weak point can lead to a drastic reduction in efficiency and stability.

The aim of this study has been to optimize the perovskite material using CVD for solar cell application. The only definitive measure of success is to achieve a high stabilized PCE exceeding 20% (J_{sc} 23 mA/cm^2, V_{oc} 1.1 V and FF 80%), demonstrating near perfect optimization. However, a more realistic target would be 12% with J_{sc} 20 mA/cm^2, V_{oc} 1 V and FF of 60%, to consider minor defects within the perovskite and transport layers.

Two main factors have already been discussed that may limit the performance of the solar cell. The first is that the substrate temperature during the thermal evaporation of the gold electrodes were too high resulting in poor performance, due to the low thermal stability of the doped Spiro-Ometad and Perovskite under vacuum. Secondly, possible band misalignment between TiO$_2$ and Perovskite could have caused the large hysteresis and low current stability.

It is possible that the root of the problem may lie with the perovskite layer itself. Fig. 4.17 compares this work to other reports of CVD perovskite solar cells that exhibit an s-curve behaviour. The most similar work has been done by Leyden et al. in 2014 forming perovskite from PbCl$_2$[97] The ETL was a 65 nm compact Tio$_2$ via spray pyrolysis on FTO and the HTL was Spiro-Ometad spin-coated using the standard solution. Gold electrodes were thermally evaporated at a pressure of 10^{-6} mbar at a rate of 0.1 Å/s. The perovskite was formed by first depositing a 100nm layer of PbCl$_2$ via PVD. The samples and MAI powder were placed in separate zones in a tube furnace which is pumped to 1 mbar pressure with a constant N$_2$ flow with an unspecified flow rate. The source and samples are heated to 185°C and 130°C respectively over 30 minutes, then the deposition lasts a further hour until the samples are allowed to cool to room temperature. The samples were also annealed in air or N$_2$ at 120°C providing an average PCE of 10.8% and 6.1% respectively. Based on XRD analyse no PbI$_2$ was detected in the perovskite. However,

the $PbCl_2$ completely converted to PbI_2 when the substrate temperature was 160°C during MAI exposure.The solar cells also exhibit large hysteresis of 37.9% and a decrease in J_{sc} from 19 to 12 mA/cm^2 when the scan rate was decreased from 450 to 66 mV/s.[97] From fig. 4.17 the IV-curve (blue) does show a lower than ideal V_{oc} and a slight s-curve indicating a small barrier in the flow of charge carriers.

The other curves are from two different papers from the same research group, where only the perovskite deposition method was changed. The ETL was a spin-coated TiO_2 layer on FTO. The HTL was Spiro-Ometad spin-coated at 4000 RPM (standard solution) in air (45% RH) with thermally evaporated silver as the electrode. Both methods required the spin-coating of PbI_2 onto TiO_2 as the base for the perovskite conversion.

In the first method MAI powder was placed in a tube furnace, with the samples placed directly above facing downwards. The tube was pumped down to an unspecified pressure (probably between 0.01 and 1 mbar). and heated to 145°C with a conversion duration of 2 hours. The samples were then removed, washed with IPA and annealed in air at 145°C for a further 30 minutes. Fig. 4.17 indicates the large improvement due to annealing in air, with shorter annealing times resulting in lower PCE. XRD and XPS confirmed that PbI_2 formed on the surface during the annealing which created a heterojunction between $MAPbI_2$ and a thin surface layer of PbI_2, producing the s-curve near the V_{oc}, but also reducing recombination at the HTL.[132]

The second method used a mixture of MAI and NH_4Cl with a weight ratio of 3:1 as the source in the same set-up. However, the tube was heated to 120° for 50 minutes, then the samples were removed and annealed in air for 30 minutes at 100°. This resulted in an improved PCE from the first method with the elimination of the s-curve, with no detectable PbI_2. When the same conversion was performed at 110° a large amount of $PbCl_2$ was detected from XRD, resulting in a reduced J_{sc} and s-curve.

Most researchers do not provide all the necessary information to duplicate results, making optimization of CVD more difficult than spin-coating methods. The CVD conversion process requires the delicate balance of all parameters to ensure the correct amount of source material is intercalated to form a defect free perovskite layer. The appropriate post treatment also forms an integral part in producing stable high efficiency solar cells. For example Li et al. (2020) used co-evaporation to form 20% efficient $MAPbI_3$ solar cells. However, a treatment with 20 mM of 1:1 molar ratio of potassium acetate and MAI in IPA and post annealing at 100°C for 30 minutes, were required to prevent close to 50% reduction in PCE within 12 hours.[126]. IPA can dissolve any unreacted MAI or MACl avoiding instability due to over-saturation and thermal annealing at 100°C in air can reduce defect within the structure with the addition of oxygen that can passivate iodide vacancies reducing dangling bonds.[133]
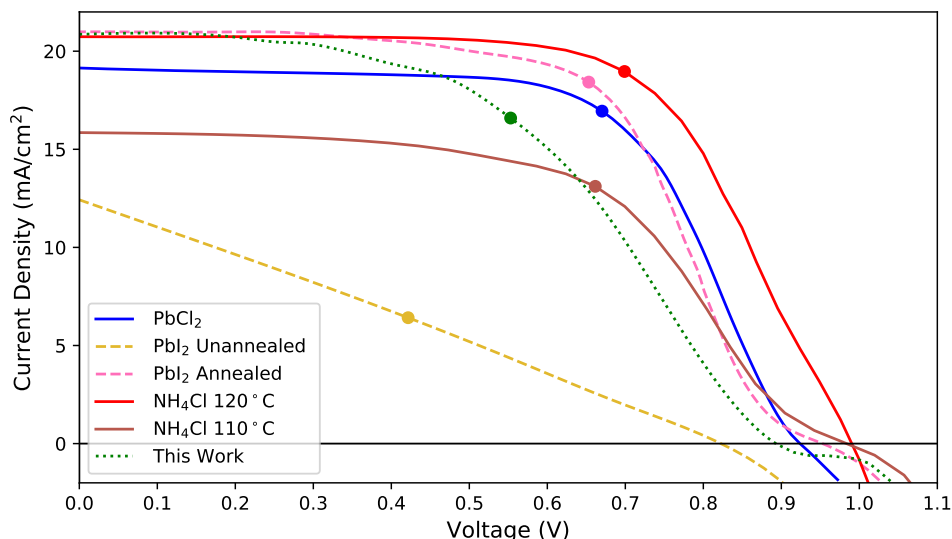
Figure 4.17: CVD Comparison

Silver was used as an electrode, to prevent heating of the samples during the metal deposition and to avoid using expensive gold. A solar cell in the n-i-p architecture requires an ohmic contact between the p-type Spiro-Ometad and metal to prevent a potential barrier from forming at the interface. An ohmic contact requires that the workfunction of the metal be greater than the Fermi energy of the p-type semiconductor, $\Phi_M > \Phi_S$.[134]

In a study by Lee et al. (2019) gold and silver were compared as electrodes, with silver requiring an ageing period in order to create the necessary ohmic connection with doped Spiro-Ometad. Samples with gold electrodes did not require aging as seen in fig. 4.18.[111] The solar cells were fabricated in a clean room with 5% RH. The ETL was a spin-coated compact layer of TiO_2, treated with $TiCl_4$ and a mesoporous layer of TiO_2. The $MAPbI_3$ perovskite was spin-coated using a one-step method with a mixed solvent of DMF and DMSO (7.33:1) with diethyl ether as an anti-solvent. Samples were annealed for 20 minutes at 130°C. The Spiro-Ometad was spin-coated from a 72 mg.ml^{-1} solution with a dopant molar ratio of 1.33:4.45:1 (Spiro:tBP:LiTFSI) and the electrodes were thermally evaporated. Solar cells with silver directly after metal deposition had a pronounced s-curve shape in the IV measurements with a much lower PCE than gold. The optimum ageing varied between different samples with at least 12 hours required to achieve a comparable PCE to gold cells. The study also documented that one cell increased from a PCE of 0.3% to 15.5% after ageing.[111]

The effect of ageing was studied by UPS by reducing the thickness of the metals to 3 nm in order to study change at the metal Spiro-Ometad interface. The Fermi energy of Spiro-Ometad was 4.9 eV, 0.3 eV above the VBM. As deposited silver had a workfunction of 4.65 eV, which after ageing increased to 5.22 eV, thus creating the required ohmic connection. The as deposited gold had a workfunction of 5.07 eV, which increased to 5.1 eV after ageing. Angle resolved XPS (AR-XPS) revealed that, LiTFSI migrated towards the silver interface leading to the formation of Ag-TFSI which caused the noticeable increase in workfunction.

Typically the LiTFSI to Spiro-Ometad molar ratio in solution is 0.5:1 in this study an increased ratio of 0.75:1 was used and the Fermi energy of a p-type semiconductor will increase with higher dopant concentration.[134] Using the typical LiTFSI ratio a Fermi energy of 4.35 eV for doped Spiro-Ometad was obtained by Wang et al (2020). However, Wang also determined that the amount of dopants in the Spiro-Ometad layer can also vary depending on the deposition method. [120] Since the VBM of Spiro-Ometad is typically 5.1 eV the Fermi energy can vary between

5.1 and 3.5 eV (VBM + E$_g$/2) depending on the dopant concentration. Therefore, since most researchers use gold as an electrode the problem of a non-ohmic interface is not a major concern and even when silver is used the band alignment through ageing might not be required depending on the Fermi energy of Spiro-Ometad.

The solar cells in this thesis did not show any increase in performance over time. However, the silver samples had a noticeable lower V$_{OC}$ compared to the gold indicating a energy band misalignment between the silver electrode and Spiro-Ometad HTL.
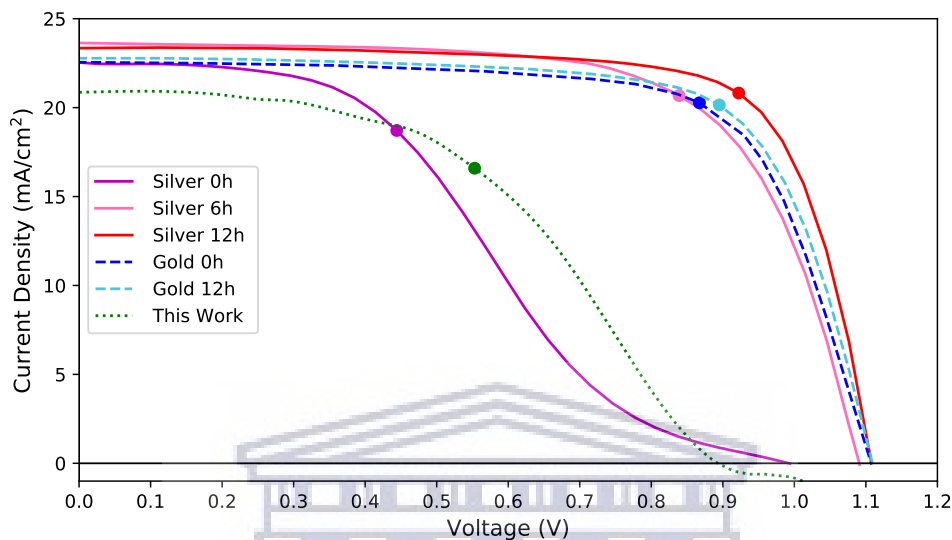
Figure 4.18: Electrode Comparison

The impact on performance due to the deposition of silver using magnetron sputtering (MS) and thermal evaporation (TE) was study by Lei et al. (2018) as seen in fig. 4.19.[135]. A 50 nm MS deposited TiO$_2$ layer on FTO was used as the ETL with a TiCl$_4$ treatment. The spin-coating was done in a dry room < 1% RH. The MAPbI3 perovskite was spin-coated in a one-step method with DMF as solvent and CB as anti-solvent. 150nm Spiro-Ometad was spin-coated at 4000 RPM for 30 seconds with a solution concentration of 72.3 mg.ml^{-1} with a dopant molar ratio of 1.85:4.67:1 (Spiro:tBP:LiTFSI). 120nm silver was deposited by MS at a pressure of 4x10^{-2} mbar and TE was done using a deposition rate of 1Å /s at an unspecified pressure. [135]

The MS samples had the lowest PCE with cross-section SEM indicating that silver particle penetrated through the Spiro-Ometad layer up to a depth slightly above the perovskite surface. The thickness of Spiro-Ometad was increased to 400nm with a 180 mg.ml^{-1} concentration resulting in silver penetrating 200nm into the Spiro-Ometad Layer as measured by EDS depth profiling. The IV measurement demonstrates nearly the same shaped curve with a small reduction in PCE. However, the dopant ratio was not provided for the adjusted concentration.[135] Another study utilized MS successfully by depositing several metals including gold and silver onto 250nm Spiro-Ometad and achieved PCE of 16.5% and 16.4% for the respective metals.[136]

During the second study the substrate temperature was controlled by a chiller at 5°C and 20°C for TE with a large reduction in PCE from 12.29% to 5.66% at the elevated temperature. The TE samples did not have any silver penetrating through the Spiro-Ometad layer.[135]

A significant improvement was observed in the study by Lei. However, the time interval was not specified, it had simply been stated that the measurements was repeated several times with an increase in PCE with each successive measurement. The most probable cause is that increased

substrate temperature can evaporate the volatile tBP resulting in voids in the Spiro-Ometed layer resulting in recombination traps.[137][138] The study indicates that keeping a low substrate temperature during TE is vital for a high PCE.

Unfortunately, most studies in literature do not provide a substrate temperature during TE, the only other mention of reduction in substrate temperature recommends that samples do not exceed 60°C without elaborating on the degree to which performance is impacted.[118] However, during the deposition of silver for this thesis, the substrates did exceed 20°C and without the use of a chiller it would be impossible to reduce the substrate temperature. Even if a lower chamber pressure could be obtained to reduce the necessary temperature of the source boat, the chamber is at room temperature.
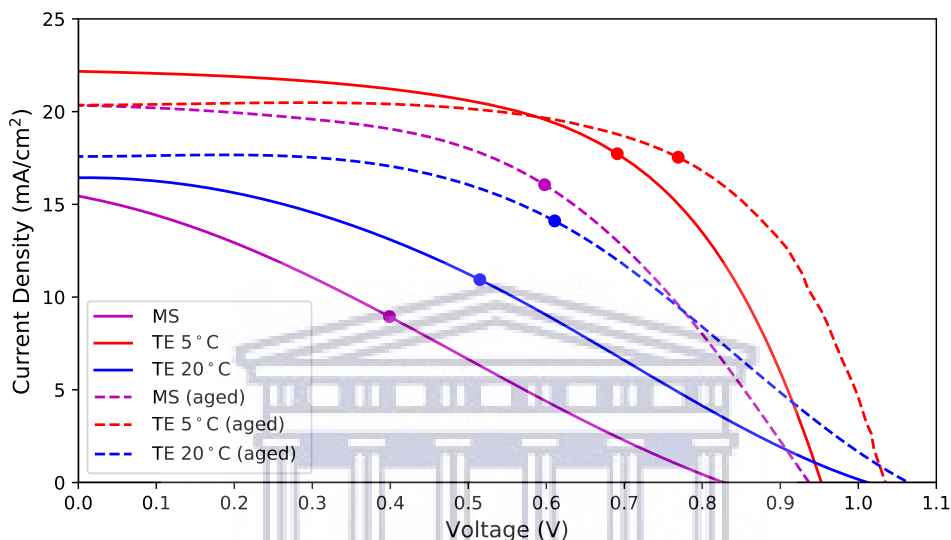
Figure 4.19: Silver Deposition Comparison

Table 4.6: Efficiency Progression Performance

Label	J_{sc} (mA/cm^2)	V_{oc} (V)	FF (%)	PCE (%)	Ref.
PbCl$_2$	19.14	0.924	64.2	11.36	[97]
PbI$_2$ Unannealed	12.50	0.825	26.0	2.68	[132]
PbI$_2$ Annealed	21.00	0.952	61.0	12.20	[132]
NH$_4$Cl 120°C	20.61	0.983	65.8	13.33	[139]
NH$_4$Cl 110°C	15.85	0.984	55.6	8.67	[139]
Gold 0h	22.57	1.106	70.9	17.70	[111]
Gold 12h	22.79	1.110	71.2	18.02	[111]
Silver 0h	22.50	0.988	37.9	8.43	[111]
Silver 6h	22.04	1.092	67.5	17.43	[111]
Silver 12h	23.36	1.110	74.3	19.26	[111]
MS	11.61	0.825	28.1	2.69	[135]
MS (aged)	15.26	0.937	50.7	7.25	[135]
TE 20°C	16.55	1.012	33.8	5.66	[135]
TE 20°C (aged)	17.51	1.060	46.6	8.64	[135]
TE 5°C	22.14	0.953	58.2	12.29	[135]
TE 5°C (aged)	20.34	1.034	64.7	13.6	[135]
This Work	20.85	0.895	49.33	9.21	

4.5 Summary

MAPbI$_3$ perovskite via sequential CVD has successfully been incorporated into solar cells with the highest achieved PCE of 9.21% However, this could only be achieved for reverse scans at a rate of 1000 mV/s. It has been observed that a decrease in scan rate resulted in decreased current density, thus a lower PCE. Degradation was also accelerated with prolonged bias at the maximum point with cells unable to maintain a stable PCE. Cells were prone to degrade rapidly with unencapsulated cells degrading to less then 10% of its initial PCE after 24 hours and encapsulated cells having a slower rate of degradation, with 12% of the initial PCE maintained after 3 days.

A major weak point came from the spin-coating of the doped Spiro-Ometad and the thermal evaporation of the silver electrode. The general trend was that the thinner the Spiro-Ometad layer was the lower the PCE and the faster the cells would degrade. Despite the fact that deposition of gold electrodes resulted in substrate temperatures exceeding 60°C , the same dynamically spin-coated at 2000 RPM Spiro-Ometad solution resulted in significantly more stable devices and higher PCE with a much greater V$_{OC}$ of 976mV compared to 620mV with silver. Only by increasing the thickness by having a more concentrated solution and statically spin-coating, were more stable devices achieved with higher PCE than gold. However, the average V$_{OC}$ was lower and had a larger deviation between cells.

The general instability of all the cells could have been the result of defects within the perovskite, which could be reduced by adjustments to the conversion parameters and a suitable post treatment. No significant improvement was observed by annealing samples in air at 100°C for 10 minutes. However, further analysis would be required.
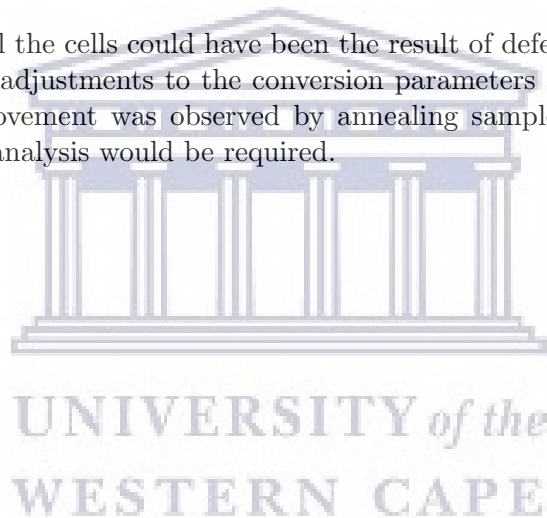
Chapter 5

Conclusion and Outlook

The use of CVD with a 5.1 cm diameter quartz tube was successfully used to deposit uniform thin films of both PbI2 and $PbCl_2$ over an area of 6 cm^2 with a thickness deviation of 5%. Thickness control was obtained by varying the amount of source material which allows for repeatable control within 5% error, without the need for a crystal thickness monitor. Both lead halides can sequentially be converted to perovskite by exposure to MAI vapour with a maximum conversion area of 40 cm^2 which results in a thickness expansion by a factor of 2 and 3 for PbI_2 and $PbCl_2$ respectively.

XRD revealed good crystallinity with crystal sizes in excess of 50nm, with PbI_2 having a highly ordered structure indicating crystal growth predominately parallel to the substrate from its high intense diffraction peaks of the $(00l)$ planes. XRD revealed complete conversion with no PbI_2 or $PbCl_2$ however even with over saturated samples that were verified with RBS, XRD could not detect MAI. The perovskite thin films were stable for several months exposed to relative humidity greater than 60%, however when exposed to sunlight in a humid environment the samples degrade to PbI_2 within 24 hours. When perovskite is encapsulated the samples can be exposed to sunlight without degradation.

The perovskite solar cells produced a maximum PCE of 9.2%, however there was a large deviation in performance with samples with the same architecture providing an average PCE of 6 ± 2%. The cells also exhibit large hysteresis and were unable to maintain a steady PCE under a constant load with a significant decrease in current density.

Several possible causes for reduced performance and stability have been identified (chapter 4.5) which primary derives from energy band misalignment and the quality of the layers which depend on the deposition method and humidity level. The main focus was on the optimization of the perovskite, however variations in solar cell architecture excluding the perovskite layer can greatly impact the performance of the solar cell. Therefore it is not possible to accurately verify the extent of optimization of the CVD perovskite. A major flaw was to rely on the most commonly used architecture (FTO/TiO$_2$/PSK/Spiro-Ometad/Gold) with the weakest link being Spiro-Ometad. The laboratories used in this study have a high humidity (60-80% RH) which leads to a poor quality layer, since the hygroscopic LiTFSI and volatile tBP are required as dopants.

Making use of a glovebox would improve repeatability and quality of spin-coating Spiro-Ometad, however a better alternative would be to use a completely different architecture. A proposed alternative is the inverted p-i-n architecture with the use of a low cost moisture resistant inorganic HTL. Two non-toxic compounds CuO_X and CuI are possible candidates due to simplistic deposition methods, low annealing temperatures and high hole mobility, thus not requiring any dopants. CuO_X can be spin-coated from Cu(acac)$_2$ dissolved in 1,2-dichlorobenzene and annealed

at 80°C for 20 minutes in air with the highest PCE of 19%.[140] CuI can be spin-coated by simply dissolving in ACN, with the highest recorded PCE of 17.5%.[141]. CuI can also be thermally evaporated, since no oxidation is required. There are still few publications in the field of perovskite solar cells using these compounds since it hasn't produced record efficiencies, however due to simplistic depositions and high tolerance to humidity it would provide the necessary foundation to further optimize the CVD perovskite. Another advantage of inverted solar cells is that gold is not required since ideally a lower work function metal like aluminium is used as an electrode and since the potential across the cell is reversed, negative iodide ions from the perovskite is less likely to migrate towards the metal electrode forming metal iodide.[142]

Both PTAA and NiO_X in an inverted solar cell has obtained efficiencies exceeding 22%.[143] [144] PTAA is an expensive organic HTL however can be used undoped with simple spin-coating of 2 mg·ml^{-1} in toluene. Undoped Spiro-Ometad could also be used in an inverted structure, however has a lower thermal stability than PTAA, with a glass transition temperature at 125°C .[145] NiO_X has the ideal VMB of 5.4eV however due to low hole mobility requires dopants to improve PCE above 18%. It also requires more complex solution processing and spin-coating with several different solutions have been used in literature. NiO_x especially nanoparticle are toxic and spin-coating can be sensitive to moisture.[146]

The major problem with the inverted architecture is the reliance on fullerene based ETLs (C60, PCBM) that are expensive to produce, however due to high conductivity does not require any dopants and molecules can be chemically modified to for example reduce moisture sensitivity of the solar cells. The ETL layer can easily be deposited most often with either spin-coated 20 mg·ml^{-1} PCBM in chlorobenzene or a thermally evaporated C60 layer.[147]

The main concern with the optimization of the CVD perovskite is that the characterization techniques used in this study had not been sufficient to determine the quality of the perovskite for solar cell application, especially since the perovskite was vacuum sealed before characterization, to prevent any degradation. Since there had not been a suitable replacement for the CVD perovskite a definitive evaluation of the architecture had not been possible. Improvements have been made on the one-step spin-coated perovskite with the use of DMSO and a flow of nitrogen during spin-coating over the samples to reduce moisture. The quality of the films have not yet been analysed, since the deposition has poor reproducibility. Chlorobenzene and toluene was used as anti-solvents, however it has been studied that ethyl acetate can significantly improve spin-coating at 75% RH.[44]

After constructing several solar cells, the CVD conversion process was reinvestigated. Initial tests concluded that the full conversion of perovskite could not take place at 130°C however by reducing the flow rate from 100 to 50 SCCM, the lead chloride could be exposed with a higher concentration of MAI vapour for a longer duration. The typical three times increase in thickness was obtained as well as the typical UV-Vis spectrum. The increased substrate temperature could allow deeper migration of MAI to alleviate any defects as well as prevent any over saturation of unconverted MAI within the perovskite structure that can lead to instability.

Bibliography

[1] Tao S., Schmidt I., Brocks G., Jiang J., Tranca I., Meerholz K., and Olthof S. Absolute energy level positions in tin- and lead-based halide perovskites. *Nature Communications*, 10(1):1–10, 2019. doi: 10.1038/s41467-019-10468-7.

[2] Fraunhofer ISE. Photovoltaics Report, 2020. URL `https://www.ise.fraunhofer.de/en/publications/studies/photovoltaics-report.html`.

[3] Ocean Optics. *USB4000 Fiber Optic Spectrometer Installation and Operation Manual*. 2006.

[4] Hansen J., Sato M., Hearty P., Ruedy R., Kelley M., and Masson-delmotte V. Ice Melt, Sea Level Rise and Superstorms: Evidence from Paleoclimate Data, Climate Modeling, and Modern Observations that 2°C Global Warming is Dangerous. *Atmospheric Chemistry & Physics Discussions*, 15(14), 2015. doi: 10.5194/acpd-15-20059-2015.

[5] M. Omar. *ELEMENTARY SOLID STATE PHYSICS : Principles and Applications*. Addison-Wesley, 4th edition, 1994. ISBN 9780201607338.

[6] Colinge J. and Colinge C. *Physics of Semiconductor Devices*. Springer Science and Business Media, 2007. ISBN 0306476223.

[7] Jung E., Jeon N., Park E., Moon C., Shin T., and Seo J. Efficient, stable and scalable perovskite solar cells using poly(3-hexylthiophene). *Nature*, 567(7749):511–515, 2019. doi: 10.1038/s41586-019-1036-3.

[8] Shockley W. and Queisser H. Detailed Balance Limit of Efficiency of p-n Junction Solar Cells. *Journal of applied physics*, 32(3):510–519, 1961. doi: 10.1063/1.1736034.

[9] Green M., Dunlop E., Kopidakis N., Hao X., and Yoshita M. Solar cell efficiency tables (version 57). *Progress in Photovoltaics: Research and Applications*, 2020. doi: 10.1002/pip. 3371.

[10] Ru S. Tabulated values of the Shockley – Queisser limit for single junction solar cells. *Solar Energy*, 130:139–147, 2016. doi: 10.1016/j.solener.2016.02.015.

[11] Kang D. and Park N. On the Current – Voltage Hysteresis in Perovskite Solar Cells : Dependence on Perovskite Composition and Methods to Remove Hysteresis. *Advanced Materials*, 31(34):1805214, 2019. doi: 10.1002/adma.201805214.

[12] Habisreutinger S., Noel N., and Snaith H. Hysteresis Index : A Figure without Merit for Quantifying Hysteresis in Perovskite Solar. *ACS Energy Letters*, 3(10):2472–2476, 2018. doi: 10.1021/acsenergylett.8b01627.

[13] Cimaroli A., Yu Y., Wang C., Liao W., Guan L., Grice C., Zhao D., and Yan Y. Tracking the maximum power point of hysteretic perovskite solar cells using a predictive algorithm. *Journal of Materials Chemistry C*, 5(39), 2017. doi: 10.1039/C7TC03482B.

[14] Rakocevic L., Ernst F., Yimga N., Vashishtha S., Aernouts T., Heumueller T., Brabec C., Gehlhaar R., and Poortmans J. Reliable Performance Comparison of Perovskite Solar Cells Using Optimized Maximum Power Point Tracking. *Solar Rrl*, 3(2):1800287, 2019. doi: 10.1002/solr.201800287.

[15] Goldschmidt V. Die Gesetze der Krystallochemie. *Naturwissenschaften*, 14(21):477–485, 1926. doi: 10.1007/BF01507527.

[16] Li C., Chi K., Soh K., and Wu P. Formability of ABO_3 perovskites. *Journal of alloys and compounds*, 372(1-2):40–48, 2004. doi: 10.1016/j.jallcom.2003.10.017.

[17] Johnsson M. and Lemmens P. *Crystallography and Chemistry of Perovskites*. Wiley-Interscience, 1st edition, 2007. ISBN 9780470022177.

[18] Kieslich G., Sun S., and Cheetham A. Solid-state principles applied to organic – inorganic perovskites : new tricks for an old dog. *Chemical Science*, 5(12):4712–4715, 2014. doi: 10.1039/C4SC02211D.

[19] Becker M., Klüner T., and Wark M. for solar cell application : first-principles determination of tolerance factors. *Dalton Transactions*, 46(11):3500–3509, 2017. doi: 10.1039/c6dt04796c.

[20] Shannon R. Revised effective ionic radii and systematic studies of interatomic distances in halides and chalcogenides. *Acta Crystallographica*, A32(5):751–767, 1976. doi: 10.1107/S0567739476001551.

[21] Travis W., Glover E., Bronstein H., Scanlon D., and Palgrave R. Chemical Science On the application of the tolerance factor to inorganic and hybrid halide perovskites : a revised system. *Chemical Science*, 7(7):4548–4556, 2016. doi: 10.1039/c5sc04845a.

[22] Masi S., Fabián A., Reyes G., and Mora-seró I. Stabilization of Black Perovskite Phase in FAPbI3 and CsPbI3. *ACS Energy Letters*, 5(6), 2020. doi: 10.1021/acsenergylett.0c00801.

[23] Zhang J. and Yu H. Multifunctional dopamine-assisted preparation of efficient and stable perovskite solar cells Multifunctional dopamine-assisted preparation of efficient and stable perovskite solar cells. *Journal of Energy Chemistry*, 54:291–300, 2020. doi: 10.1016/j.jechem.2020.05.061.

[24] Kim J., Lee S., Lee J., and Hong K. The Role of Intrinsic Defects in Methylammonium Lead Iodide. *The journal of physical chemistry letters*, 5(8):1312–1317, 2014. doi: 10.1021/jz500370k.

[25] Cui P., Wei D., Ji J., Huang H., Jia E., Dou S., Wang T., Wang W., and Li M. Planar p–n homojunction perovskite solar cells with efficiency exceeding 21.3%. *Nature Energy*, 4(2):150–159, 2019. doi: 10.1038/s41560-018-0324-8.

[26] Hanwell M., Curtis D., Lonie D., Vandermeersch T., Zurek E., and Hutchison G. Avogadro : An advanced semantic chemical editor , visualization , and analysis platform. *ournal of cheminformatics*, 4(1):17, 2012. doi: 10.1186/1758-2946-4-17.

[27] Kojima A., Teshima K., Miyasaka T., and Shirai Y. Novel Photoelectrochemical Cell with Mesoscopic Electrodes Sensitized by Lead-Halide Compounds. *The Electrochemical Society, Meeting Abstract*, 7, 2006. doi: 10.1149/ma2007-02/8/352.

[28] Kim H., Lee C., Im J., Lee K., Moehl T., Marchioro A., Moon S., Humphry-Baker R., Yum J., Moser J., Gratzel M., and Park N. Lead Iodide Perovskite Sensitized All-Solid-State Submicron Thin Film Mesoscopic Solar Cell with Efficiency Exceeding 9%. *Scientific reports*, 2(591), 2012. doi: 10.1038/srep00591.

[29] Min H., Kim M., Lee S., Kim H., Kim G., Choi K., Lee J., and Seok S. Efficient, stable solar cells by using inherent bandgap of a -phase formamidinium lead iodide. *Science*, 366 (6466):749–753, 2019. doi: 10.1126/science.aay7044.

[30] Kojima A., Teshima K., Miyasaka T., and Shirai Y. Organometal Halide Perovskites as Visible-Light Sensitizers for Photovoltaic. *Journal of the American Chemical Society*, 131 (17):6050–6051, 2009. doi: 10.1021/ja809598r.

[31] Im J., Lee C., Lee J., Park S., and Park N. 6.5% Efficient Perovskite Quantum-dot-sensitized Solar Cell. *Nanoscale*, 3(10):4088–4093, 2011. doi: 10.1039/c1nr10867k.

[32] Lee M., Teuscher J., Miyasaka T., Murakami T., and Snaith H. Efficient Hybrid Solar Cells Based on Meso-Superstructured Organometal Halide Perovskites. *Science*, 338(6107): 643–648, 2012. doi: 10.1126/science.1228604.

[33] Burshka J., Pellet N., Moon S., Humphry-Baker R., Gao P., Nazeeruddin M., and Gratzel M. Sequential deposition as a route to high-performance perovskite-sensitized solar cells. *Nature*, 499(7458):316–319, 2013. doi: 10.1038/nature12340.

[34] Liu M., Johnston M., and Snaith H. Efficient planar heterojunction perovskite solar cells by vapour deposition. *Nature*, 501(7467):395–398, 2013. doi: 10.1038/nature12509.

[35] Jeon N., Noh J., Kim Y., Yang W., Ryu S., and Seok S. Solvent engineering for high-performance inorganic–organic hybrid perovskite solar cells. *Nature materials*, 13(9):897–903, 2014. doi: 10.1038/NMAT4014.

[36] Zhou H., Chen Q., Li G., Luo S., Song T., Duan H., Hong Z., You J., Liu Y., and Yang Y. Interface engineering of highly efficient perovskite solar cells. *Science*, 345(6196):542–546, 2014. doi: 10.1126/science.1254050.

[37] Yang W., Noh J., Jeon N., Kim Y., Ryu S., Seo J., and Yang W. High-performance photovoltaic perovskite layers fabricated through intramolecular exchange. *Science*, 348 (6240):1234–1238, 2015. doi: 10.1126/science.aaa8765.

[38] Saliba M., Matsui T., Seo J., Domanki K., Correo-Baena J., Nazeeruddin M., Tress W., Abate A., Hagfeldt A., and Gratzel M. Cesium-containing triple cation perovskite solar cells: improved stability, reproducibility and high efficiency. *Energy & Environmental Science*, 9 (6):1989–1997, 2016. doi: 10.1039/c5ee03874j.

[39] Shin S., Yeom E., Yang W., Hur S., Kim M., Im J., Seo J., Noh J., and Seok S. Colloidally prepared La-doped BaSnO 3 electrodes for efficient, photostable perovskite solar cells. *Science*, 356(6334):167–171, 2017. doi: 10.1126/science.aam6620.

[40] Yang W., Park B., Jeon N., Kim Y., Lee D., Shin S., Seo J., Kim E., Noh J., and Seok S. Iodide management in formamidinium-lead-halide-based perovskite layers for efficient solar cells. *Science*, 356(6345):1376–1379, 2017. doi: 10.1126/science.aan2301.

[41] Jeon N., Na H., Jung E., Yang T., Lee Y., Kim G., Shin H., Seok S., Lee J., and Seo J. A fluorene-terminated hole-transporting material for highly efficient and stable perovskite solar cells. *Nature Energy*, 3(8):682–689, 2018. doi: 10.1038/s41560-018-0200-6.

92

[42] Jiang Q., Zhao Y., Zhang X., Yang X., Chen Y., Chu Z., Ye Q., Li X., Yin Z., and You J. Surface passivation of perovskite film for efficient solar cells. *Nature Photonics*, 13(7): 460–466, 2019. doi: 10.1038/s41566-019-0398-2.

[43] Li J., Yang R., Que L., Wang Y., Wang F., Wu J., and Li S. Optimization of anti-solvent engineering toward high performance perovskite solar cells. *Journal of Materials Research*, 34(14):2416–2424, 2019. doi: 10.1557/jmr.2019.122.

[44] Troughton J., Hooper K., and Watson T. Humidity resistant fabrication of CH3NH3PbI3 perovskite solar cells and modules. *Nano Energy*, 39(6):60–68, 2017. doi: 10.1016/j.nanoen.2017.06.039.

[45] Best Research-Cell Efficiencies National Renewable Energy Laboratory (NREL), 2020. URL `https://www.nrel.gov/pv/assets/pdfs/best-research-cell-efficiencies.20200104.pdf`.

[46] Wieghold S., Peters M., and Buonassisi T. Environmental Science Revisiting thin silicon for photovoltaics : a technoeconomic perspective. *Energy and Environmental Science*, 13 (1):12–23, 2020. doi: 10.1039/c9ee02452b.

[47] GlobalData. China's JinkoSolar preserves its leading global solar PV module shipment rank in 2019, 2020. URL `https://www.globaldata.com/chinas-jinkosolar-preserves-its-leading-global-solar-pv-module-shipment-rank-in-2019`.

[48] Solar Frontier. Product Catalogue, 2021. URL `https://www.solar-frontier.com/eng/solutions/products/index.html`.

[49] First Solar. Product Catalogue, 2021. URL `https://www.firstsolar.com/Modules/Series-6`.

[50] Publicover B. Oxford PV orders 100 MW production line from Meyer Burger, 2019. URL `https://www.pv-magazine.com/2019/08/08/oxford-pv-orders-100-mw-production-line-from-meyer-burger/`.

[51] Fuhs M. Long read: PV Perovskites Hit the Home Stretch, 2019. URL `https://www.pv-magazine-australia.com/2019/10/05/long-read-pv-perovskites-hit-the-home-stretch/`.

[52] Buyi Y. and Jizhong Y. Perovskite thin film low-pressure chemical deposition equipment and uses thereof, 2019. Hangzhou Microquanta Semiconductor Co Ltd,US Patent: US10319534B2.

[53] Ho-baillie A., Chang N., Wing A., Ho-baillie Y., Vak D., Gao M., Green M, and Egan R. Manufacturing cost and market potential analysis of demonstrated roll-to- roll perovskite photovoltaic cell processes Solar Energy Materials and Solar Cells Manufacturing cost and market potential analysis of demonstrated roll-to- roll perovskite photovol. *Solar Energy Materials and Solar Cells*, 174(9):314–324, 2018. doi: 10.1016/j.solmat.2017.08.038.

[54] Aggarwal V. Solar Panel Warranties: What You Need to Know, 2021. URL `https://news.energysage.com/shopping-solar-panels-pay-attention-to-solar-panels-warranty`.

[55] Boyd C., Cheacharoen R., Leijtens T., and Mcgehee M. Understanding Degradation Mechanisms and Improving Stability of Perovskite Photovoltaics. *Chemical reviews*, 119(5): 3418–3451, 2018. doi: 10.1021/acs.chemrev.8b00336.

[56] Ava T., Mamun A., and Marsillac S. A Review : Thermal Stability of Methylammonium Lead Halide Based Perovskite Solar Cells. *Applied Sciences*, 9(1), 2019. doi: 10.3390/app9010188.

[57] Aftab A. and Ahmad I. A review of stability and progress in tin halide perovskite solar cell. *Solar Energy*, 216:26–47, 2021. doi: 10.1016/j.solener.2020.12.065.

[58] Babayigit A., Thanh D., Ethirajan A., Manca J., and Muller M. Assessing the toxicity of Pb- and Sn-based perovskite solar cells in model organism Danio rerio. *Scientific reports*, 6 (1), 2016. doi: 10.1038/srep18721.

[59] Park N., Grätzel M., Miyasaka T., Zhu K., and Emery K. Towards Stable and Commercially Available Perovskite Solar Cells. *Nature Energy*, 1(11), 2016. doi: 10.1038/nenergy.2016.152.

[60] Tsai C., Wu H., Chang S., Huang C., and Wang C. Role of Tin Chloride in Tin-Rich Mixed-Halide Perovskites Applied as Mesoscopic Solar Cells with a Carbon Counter Electrode. *ACS Energy Letters*, 1(6):1086–1093, 2016. doi: 10.1021/acsenergylett.6b00514.

[61] Fraunhofer-Gesellschaft. Energy Charts, 2020. URL https://energy-charts.info/charts/installed_power/chart.htm?l=en&c=DE.

[62] PV-Magazine. Germany eliminates 52 GW cap for solar incentives, 2020. URL https://www.pv-magazine.com/2020/05/19/germany-eliminates-52-gw-cap-for-solar-incentives.

[63] Fraunhofer-Gesellschaft. Energy Charts, 2020. URL https://energy-charts.info/charts/energy/chart.htm?l=en&c=DE&interval=year&year=-1.

[64] Mongird K., Viswanathan V., Balducci P., Alam J., Fotedar V., Koritarov V., and Hadjerioua B. Energy Storage Technology and Cost Characterization Report No. PNNL-28866. *Pacific Northwest National Lab.(PNNL)*, 2019.

[65] REDIS. Production and Operating Capacity – The Renewable Energy Data and Information Service, 2021. URL http://redis.energy.gov.za/power-production.

[66] Mehrjerdi H. and Rakhshani E. Vehicle-to-grid technology for cost reduction and uncertainty management integrated with solar power. *Journal of Cleaner Production*, 229:463–469, 2019. doi: 10.1016/j.jclepro.2019.05.023.

[67] Sedin D. and Rowlen K. Influence of tip size on AFM roughness measurements. *Applied surface science*, 182(1):40–48, 2001. doi: 10.1016/S0169-4332(01)00432-9.

[68] Griffiths, D. J. *Introduction to electrodynamics*. Pearson, Boston, 4th edition, 2014. ISBN 9780321856562.

[69] Viezbicke B., Patel S., Davis B., and Iii D. Evaluation of the Tauc method for optical absorption edge determination : ZnO thin fi lms as a model system. *physica status solidi (b)*, 252(8):1700–1710, 2015. doi: 10.1002/pssb.201552007.

[70] Look D., Leach J., and Road M. On the accurate determination of absorption coefficient from reflectance and transmittance measurements : application to Fe-doped GaN. *Journal of Vacuum Science and Technology B*, 34(4), 2016. doi: 10.1116/1.4954211.

[71] Makula P., Pacia M., and Macyk W. How To Correctly Determine the Band Gap Energy of Modified Semiconductor Photocatalysts Based on UV-Vis Spectra. *The Journal of Physical Chemistry Letters*, 9(23):6814–6817, 2018. doi: 10.1021/acs.jpclett.8b02892.

[72] Tauc J., Grigorovici R., and Vancu A. Optical Properties and Electronic Structure of Amorphous Germanium. *physica status solidi (b)*, 15(2):627–637, 1966. doi: 10.1002/pssb. 19660150224.

[73] Stenzel O. *The Physics of Thin Film Optical Spectra: An Introduction*. Springer, 2nd edition, 2016. ISBN 9783319216010.

[74] Lee Y. and Lim W. Shoelace Formula: Connecting the Area of a Polygon and the Vector Cross Product. *The Mathematics Teacher*, 110(8):631–636, 2017. doi: 10.5951/mathteacher. 110.8.0631.

[75] T. E. Oliphant. *A guide to NumPy*. Trelgol, USA, 2014.

[76] Cullity B.D. *Elements of X-Ray Diffraction*. Addison-Wesley Longman, Inc., 2nd edition, 1978.

[77] Hahn T. *International Tables for Crystallography, Volume A*. Springer, 5th edition, 2005. ISBN 0792365909.

[78] Schaeffer R. and Monica A. Powder X-ray diffraction of oriented and intercalated lead iodide. *Powder Diffraction*, 16(1):16–19, 2001. doi: 10.1154/1.1332077.

[79] Momma K. and Izumi F. VESTA 3 for three-dimensional visualization of crystal , volumetric and morphology data. *Journal of applied crystallography*, 44(6):1272–1276, 2011. doi: 10. 1107/S0021889811038970.

[80] Murray-Rust P. Crystallography Open Database (COD), 2020. URL http://www. crystallography.net/cod/.

[81] Toby B. and Von Dreele R. GSAS-II : The Genesis of a Modern Open-Source All-Purpose Crystallography GSAS-II : the genesis of a modern open-source all purpose crystallography software package. *Journal of Applied Crystallography*, 46(2):544–549, 2013. doi: 10.1107/ S0021889813003531.

[82] Argonne National Laboratory. GSAS-II Help, 2021. URL https://subversion.xray.aps. anl.gov/pyGSAS/trunk/help/gsasII.html.

[83] Wolfram MathWorld. Gaussian Function, 2020. URL https://mathworld.wolfram.com/ GaussianFunction.html.

[84] Duck B., Jung Y., Settens C., Niroui F., Macdonald J., Burghammer M., Friend R., and S. Stranks. Lattice strain causes non-radiative losses in halide perovskites. *Energy and Environmental Science*, 12(2):596–606, 2019. doi: 10.1039/c8ee02751j.

[85] NIST. Signal to Noise Ratio, 2020. URL https://www.itl.nist.gov/div898/software/ dataplot/refman2/auxillar/snr.htm.

[86] Nastasi M., Mayer J. W., and Wang Y. *Ion Beam Analysis*. Taylor & Francis Group, 1st edition, 2014. ISBN 9781439846391.

[87] Mayer M. SIMNRA, a simulation program for the analysis of NRA, RBS and ERDA. *AIP Conference Proceedings*, 475(1):541–544, 1999. doi: 10.1063/1.59188.

[88] Rosman K. and Taylor P. Isotopic compositions of the elements 1997 (Technical Report). *Pure and Applied Chemistry*, 70(1):217–235, 1998. doi: 10.1351/pac199870010217.

[89] Inc. Keithley Instruments. *Series 2400 SourceMeter User's Manual*. Cleveland, Ohio, U.S.A, 2011.

[90] H. O. Pierson. *Handbook of Chemical Vapor Deposition (CVD)*. William Andrew, Norwich, New York, 2nd edition, 2000. ISBN 0815514328.

[91] Ono L., Leyden M., Wang S., and Qi Y. Organometal halide perovskite thin films and solar cells by vapor deposition. *Journal of Materials Chemistry A*, 4(18), 2016. doi: 10.1039/c5ta08963h.

[92] Terpstra P. and Westenbrink H. On the crystal structure of lead-iodide. *Proceedings of the Koninklijke Nederlandse Academie van Wetenschappen*, 29:431–442, 1920.

[93] Wyckoff R. *Crystal Structures*. Interscience, New York, 2nd edition, 1963.

[94] Yamamuro O., Matsuo T., Suga H., David W., Ibberson R., and Leadbetter A. Neutron Diffraction and Calorimetric Studies of Methylammonium Iodide*. *Acta Crystallographica Section B: Structural Science*, 48(3):329–336, 1992. doi: 10.1107/S0108768192000260.

[95] Zhao Z., Cao H., Li J., Zhu H., Yang L., and Yin S. Strategies to obtain stoichiometric perovskite by sequential vapor deposition learned by modeling the diffusion-dominated formation of perovskite films. *Applied Physics Express*, 11(10):105501, 2018. doi: 10.7567/APEX.11.105501.

[96] Azam M., Yue S., Liu K., Sun Y., Liu J., Ren K., Wang Z., Qu S., and Wang Z. Insight into the Influence of Cl Incorporation into Lead-Halide Perovskite Materials : A Review. *Journal of Nanoscience and Nanotechnology*, 18(11):7335–7348, 2018. doi: 10.1166/jnn.2018.16041.

[97] Leyden M., Ono L., Raga S., Kato Y., and Wang S. High performance perovskite solar cells by hybrid chemical vapor deposition. *Journal of Materials Chemistry A*, 2(44):18742–18745, 2014. doi: 10.1039/c4ta04385e.

[98] Luo P., Zhou S., Xia W., Cheng J., Xu C., and Lu Y. Chemical Vapor Deposition of Perovskites for Photovoltaic Application. *Advanced Materials Interfaces*, 4(8):1600970, 2017. doi: 10.1002/admi.201600970.

[99] Imler G., Li X., and Xu B. Solid state transformation of the crystalline monohydrate (CH3NH3) PbI3(H2O) to the (CH3NH3)PbI3 perovskite. *Chemical Communications*, 51 (56):11290–11292, 2015. doi: 10.1039/C5CC03741G.

[100] Kim B., Han Y., and Kim J. Growth mechanism of CH3NH3I in a vacuum processed perovskite. *Nanoscale Advances*, 2(9):3906–3911, 2020. doi: 10.1039/d0na00466a.

[101] Moser T., Artuk K., Jiang Y., Feurer T., and Gilshtein E. Revealing the perovskite formation kinetics during chemical vapour deposition. *Journal of Materials Chemistry A*, 8(24): 21973–21982, 2020. doi: 10.1039/d0ta04501b.

[102] Fox M. *Optital Properties of Solids*. Oxford University Press, 2nd edition, 2010. ISBN 978-0199573370.

[103] Colella S., Mosconi E., Fedeli P., Listorti A., Gazza F., Orlandi F., Ferro P., Besagni T., Rizzo A., Calestani G., Gigli G., Angelis F., and Mosca R. MAPbI3-xClx Mixed Halide Perovskite for Hybrid Solar Cells : The Role of Chloride as Dopant on the Transport and Structural Properties. *Chemistry of Materials*, 25(22):4613–4618, 2013. doi: 10.1021/cm402919x.

[104] Silva A., Veissid N., An C., Pepe I., and Oliveira N. Optical determination of the direct bandgap energy of lead iodide crystals Optical determination of the direct bandgap energy of lead iodide crystals. *Applied physics letters*, 69(13):1930–1932, 1996. doi: 10.1063/1.117625.

[105] Frisenda R., Island J., Lado J., Giovanelli E., Gant P., Bange S., Lupton J., Schüller C., Molina-mendoz A., Foerster M., Korn T., Niño M., Lara D., Pé E., Fernandéz-rossier J., and Castellanos-gomez A. Characterization of highly crystalline lead iodide nanosheets prepared by room-temperature solution processing. *Nanotechnology*, 28(45):455703, 2017. doi: 10.1088/1361-6528/aa8e5c.

[106] Sobolev V., Kalugin A., Vostrikov I., and Sobolev V. Electronic Structure and Optical Properties of Lead Chloride. *Journal of Surface Investigation. X-ray, Synchrotron and Neutron Techniques*, 3(1):56–65, 2009. doi: 10.1134/S1027451009010091.

[107] Ju D., Zhao T., Dang Y., and Zhang G. Gas induced conversion of hybrid perovskite single crystal to single crystal for great enhancement of their photoelectric properties. *A Journal of Materials Chemistry A*, 5(41):21919–21925, 2017. doi: 10.1039/C7TA07413A.

[108] Xu X., Shi J., Wu H., Yang Y., Xiao J., Luo Y., Li D., Meng Q., Xu X., Shi J., Wu H., Yang Y., Xiao J., and Luo Y. The influence of different mask aperture on the open-circuit voltage measurement of perovskite solar cells. *Journal of Renewable and Sustainable Energy*, 7(4): 043104, 2015. doi: 10.1063/1.4926481.

[109] Shi D., Adinolfi V., Comin R., Yuan M., Alarousu E., and Buin A. Low trap-state density and long carrier diffusion in organolead trihalide perovskite single crystals. *Science*, 347 (6221), 2015. doi: 10.1126/science.aaa2725.

[110] Sima C., Grigoriu C., and Antohe S. Comparison of the dye-sensitized solar cells performances based on transparent conductive ITO and FTO. *Thin Solid Films*, 519(2):595–597, 2010. doi: 10.1016/j.tsf.2010.07.002.

[111] Lee D., Kim M., Wang S., Kim B., Shirley M., and Jung H. Effect of Metal Electrodes on Aging-Induced Performance Recovery in Perovskite Solar Cells. *ACS Applied Materials & Interfaces*, 11(51):48497–48504, 2019. doi: 10.1021/acsami.9b14619.

[112] Qin J., Zhang Z., Shi W., Liu Y., Gao H., and Mao Y. The optimum titanium precursor of fabricating TiO 2 compact layer for perovskite solar cells. *Nanoscale research letters*, 12 (1):620, 2017. doi: 10.1186/s11671-017-2418-9.

[113] Qourzal S. and Assabbane A. Synthesis of TiO 2 via hydrolysis of titanium tetraisopropoxide and its photocatalytic activity on a suspended mixture with activated carbon in the degradation of 2-naphthol. *Photochemistry and Photobiology A: Chemistry*, 163(3):317–321, 2004. doi: 10.1016/j.jphotochem.2003.12.013.

[114] Smatt J., Sand S., Vivo P., Ojanper A., Ghufran S., Kaunisto K., Ihalainen P., Talha M., Lund P., Lemmetyinen H., and Osterbacka R. Influence of TiO2 compact layer precursor on the performance of perovskite solar cells. *Organic Electronics*, 41:287–293, 2017. doi: 10.1016/j.orgel.2016.11.017.

[115] Bansal S., Pandya D., Kashyap S., Bansal S., Pandya D., and Kashyap S. Electron transport and defect structure in highly conducting reactively sputtered ultrathin tin oxide films Electron transport and defect structure in highly conducting reactively sputtered ultrathin tin oxide films. *Applied Physics Letters*, 104(8):082108, 2014. doi: 10.1063/1.4866869.

[116] Matsui T., Tress W., Saliba M., Abate A., Gra M., and Hagfeldt A. Environmental Science cells by solution-processed tin oxide. *Energy & Environmental Science*, 9:3128–3134, 2016. doi: 10.1039/C6EE02390H.

[117] Ganchev M., Katerski A., Stankova S., Eensalu J., Terziyska P., Gergova R., Dikov H., and Popkirov G. Tin dioxide thin films deposited by sol – gel technique Tin Dioxide Thin Films Deposited by Sol – Gel Technique. *In AIP Conference Proceedings*, 2075(1):140001, 2019. doi: 10.1063/1.5091316.

[118] Saliba M., Wol C., Stolterfoht M., Phung N., Albrecht S., Neher D., and Abate A. How to Make over 20% Efficient Perovskite Solar Cells in Regular (n-i-p) and Inverted (p-i-n) Architectures. *Chemistry of Materials*, 30(13):4193–4201, 2018. doi: 10.1021/acs.chemmater. 8b00136.

[119] Liao K., Li C., Xie L., Yuan Y., Wang S., and Cao Z. Hot - Casting Large - Grain Perovskite Film for Efficient Solar Cells : Film Formation and Device Performance. *Nano-Micro Letters*, 12(1):1–22, 2020. ISSN 2150-5551. doi: 10.1007/s40820-020-00494-2.

[120] Wang S., Cabreros A., Yang Y., Fenning D., Wang S., Cabreros A., Yang Y., Hall A., Valenzuela S., Luo Y., Kim M., and file = :home/stephen/Desktop/papers/M-Sc/HTL/Spiro/[20]dynamic_vs_static.pdf:pdf journal = Cell Reports Physical Science mendeley-groups = Ch4 number = 7 pages = 100103 publisher = Elsevier Inc. title = Impacts of the Hole Transport Layer Deposition Process on Buried Interfaces in Perovskite Solar Cells Impacts of the Hole Transport Layer Deposition Process on Buried Interfaces in Perovskite Solar Cells volume = 1 year = 2020 ., Fjeldberg and D., Fenning, doi = 10.1016/j.xcrp.2020.100103.

[121] Marinova N., Tress W., Humphry-baker R., Dar M., Bojinov V., Zakeeruddin S., Nazeeruddin M., and Gra M. Light Harvesting and Charge Perovskite Solar Cells Studied by Hole Transport Layer Thickness Variation. *ACS nano*, 9(4):4200–4209, 2015. doi: 10.1021/acsnano.5b00447.

[122] Liu G., Xi X., Chen R., Chen L., Chen G., Liu G., Xi X., Chen R., Chen L., and Chen G. Oxygen aging time : A dominant step for Spiro-OMeTAD in perovskite solar cells. *Journal of Renewable and Sustainable Energy*, 10(4):043702, 2018. doi: 10.1063/1.5031167.

[123] Xi H., Tang S., Chang J., Chen D., Lin Z., Zhong P., Wang H., and Zhang C. Performance Enhancement of Planar Heterojunction Perovskite Solar Cells through Tuning the Doping Properties of Hole-Transporting Materials. *ACS omega*, 2(1):326–336, 2017. doi: 10.1021/acsomega.6b00465.

[124] Tan B., Raga S., Chesman A., Fürer S., Zheng F., Mcmeekin D., Jiang L., Mao W., Lin X., Wen X., Lu J., Cheng Y., and Bach U. Litfsi-free spiro-ometad-based perovskite solar cells with power conversion efficiencies exceeding 19 %. 1901519:1–10, 2019. doi: 10.1002/aenm.201901519.

[125] Zou J., Wu J., Sun W., Zhang M., Wang X., Yuan P., Zhu Q., Yin J., Liu X., and Yang Y. Solvent engineering of LiTFSI towards high efficiency planar perovskite solar cells. *Solar Energy*, 194(October):321–328, 2019. doi: 10.1016/j.solener.2019.10.067.

[126] Li J., Wang H., Yu X., Li J., Wang H., Chin X., Dewi H., Vergeer K., and Goh T. Highly Efficient Thermally Co-evaporated Perovskite Solar Cells and Mini-modules. *Joule*, 4(5): 1–19, 2020. doi: 10.1016/j.joule.2020.03.005.

[127] Luo W., Wu C., Wang D., Zhang Z., Qi X., Guo X., Qu B., Xiao L., and Chen Z. Dopant-free Spiro-OMeTAD as hole transporting layer for stable and efficient perovskite solar cells. *Organic Electronics*, 74(6):7–12, 2019. doi: 10.1016/j.orgel.2019.06.039.

[128] Chen B., Yang M., Priya S., and Zhu K. Origin of J-V Hysteresis in Perovskite Solar Cells. *The journal of physical chemistry letters*, 7(5):905–917, 2016. doi: 10.1021/acs. jpclett.6b00215.

[129] Pablo J., Baena C., Steier L., Tress W., Saliba M., Neutzner S., Matsui T., Giordano F., Jacobsson T., Ram A., Kandada S., Zakeeruddin S., Petrozza A., and Hagfeldt A. Highly efficient planar perovskite solar cells through band alignment engineering. *Energy & Environmental Science*, 8(10):2928–2934, 2015. doi: 10.1039/c5ee02608c.

[130] Heo J. and Im S. Highly reproducible, efficient hysteresis-less ch$_3$nh$_3$pbi$_{3-x}$cl$_x$ planar hybrid solar cells without requiring heat-treatment. *Nanoscale*, 8(5):2554–2560, 2015. doi: 10.1039/ C5NR08458J.

[131] Jang J., Choe G., and Yim S. Effective Control of Chlorine Contents in MAPbI3$_{3-x}$Cl$_x$ Perovskite Solar Cells Using a Single-Source Vapor Deposition and Anion- Exchange Technique. *ACS Applied Materials & Interfaces*, 11(22):20073–20081, 2019. ISSN 1944-8244. doi: 10.1021/acsami.9b05101.

[132] Luo P., Liu Z., Xia W., Yuan C., Cheng J., and Lu. A simple in situ tubular chemical vapor deposition processing of large-scale efficient perovskite solar cells and the research on their novel roll-over phenomenon in J–V curves. *Journal of Materials Chemistry A*, 3(23): 12443–12451, 2015. doi: 10.1039/C5TA02306H.

[133] Ng A., Ren Z., Shen Q., Cheung S., Gokkaya H., So S., Djuris A., Wan Y., Wu X., and Surya C. Crystal Engineering for Low Defect Density and High E ffi ciency Hybrid Chemical Vapor Deposition Grown Perovskite Solar Cells. *ACS applied materials & interfaces*, 8(48): 32805–32814, 2016. doi: 10.1021/acsami.6b07513.

[134] Hummel R. E. *Electronic Properties of Materials*. Springer, New York, 3rd edition, 2001. ISBN 038775144X.

[135] Lei L., Zhang S., Yang S., Li X., and Yu Y. Influence of hole transport material / metal contact interface on perovskite solar cells. *Nanotechnology*, 29(25):255201, 2018. doi: 10. 1088/1361-6528/aab795.

[136] Behrouznejad F., Shahbazi S., Taghavinia N., Wu H., and Diau E. A study on utilizing different metals as the back contact of CH3NH3PbI3 perovskite solar cells. *Journal of Materials Chemistry A: Materials for energy and sustainability*, 4(35):13488–13498, 2016. doi: 10.1039/C6TA05938D.

[137] Cho Y., Ohkita H., Li Y., Bing J., and Zheng J. The Effect of 4- tert -Butylpyridine Removal on Efficiency and Thermal Stability in Perovskite Solar Cells. *J. Photopolym. Sci. Technol.*, 32(5):715–720, 2019. doi: 10.2494/photopolymer.32.715.

[138] Liu Y., Hu Y., Zhang X., Zeng P., Li F., Wang B., Yang Q., and Liu M. Nano Energy Inhibited aggregation of lithium salt in spiro-OMeTAD toward highly efficient perovskite solar cells. *Nano Energy*, 70(1):104483, 2020. doi: 10.1016/j.nanoen.2020.104483.

[139] Liu Z., Xia W., Zhou S., Cheng J., Sun L., Xu C., and Lu Y. Acceleration effect of chlorine in the gas-phase growth process of CH3NH3PbI3(Cl) films for efficient perovskite solar cells. *Journal of Materials Chemistry C*, 4(26):6336–6344, 2016. doi: 10.1039/C6TC01781A.

[140] Rao H., Ye S., Sun W., Yan W., Li Y., Peng H., Liu Z., Bian Z., Li Y., and Huang C. A 19.0% efficiency achieved in CuOx-based inverted CH3NH3PbI3xClx solar cells by an effective Cl doping method. *Nano Energy*, 27:51–57, 2016. doi: 10.1016/j.nanoen.2016.06.044.

[141] Cao J., Wu B., Peng J., Feng X., Li C., and Tang Y. Copper-copper iodide hybrid nanostructure as hole transport material for efficient and stable inverted perovskite solar cells. *Science China Chemistry*, 62(3):363–369, 2019. doi: 10.1007/s11426-018-9386-5.

[142] Kato Y., Ono L., Lee M., Wang S., Raga S., and Qi Y. Silver Iodide Formation in Methyl Ammonium Lead Iodide Perovskite Solar Cells with Silver Top Electrodes. *Advanced Materials Interfaces*, 2(13):1500195, 2015. doi: 10.1002/admi.201500195.

[143] Zheng X., Hou Y., Bao C., Yin J., Yuan F., Huang Z., Song K., Liu J., Troughton J., Gasparini N., Zhou C., Lin Y., Xue D., Chen B., Johnston A., Wei N., and Hedhili M. Managing grains and interfaces via ligand anchoring enables 22.3%-efficiency inverted perovskite solar cells. *Nature Energy*, 5(2):131–140, 2020. doi: 10.1038/s41560-019-0538-4.

[144] Ru P., Bi E., Zhang Y., Wang Y., Kong W., and Sha Y. High Electron Affinity Enables Fast Hole Extraction for Efficient Flexible Inverted Perovskite Solar Cells. *Advanced Energy Materials*, 10(12):1903487, 2020. doi: 10.1002/aenm.201903487.

[145] Bailie C., Unger E., Zakeeruddin S., Gra M., and Mcgehee M. Melt-infiltration of spiro-OMeTAD and thermal instability of solid-state dye-sensitized solar cells. *Physical Chemistry Chemical Physics*, 16(10):4864–4870, 2014. doi: 10.1039/c4cp00116h.

[146] Girolamo D., Giacomo D., Matteocci F., Marrani A., and Abate A. Chemical Science Progress , highlights and perspectives on NiO in perovskite photovoltaics. *Chemical Science*, 11(30):7746–7759, 2020. doi: 10.1039/d0sc02859b.

[147] Castro E., Echegoyen L., Murillo J., and Fernandez-delgado O. Progress in fullerene-based hybrid perovskite solar cells. *Journal of Materials Chemistry C*, 6(11):2635–2651, 2018. doi: 10.1039/C7TC04302C.

[148] Kim Y., Hoon S., and Jung M. Structural refinement of SnO$_2$ thin film prepared by plasma-enhanced chemical vapor deposition. *Materials Letters*, 57(22):3653–3659, 2003. doi: 10.1016/S0167-577X(03)00143-5.

Appendix A

UV-VIS

A.1 PCBM

The thermal stability of PCBM was tested by heating two samples one at 100°C and the other at 140°C for 30 minutes at pressure of 4mbar and a N_2 flow rate of 500 SCCM. The samples were spin-coated on ITO from a 20 mg·ml^{-1} PCBM in chlorobenzene solution. The samples were dynamically spin-coated at 1000 RPM for 30 seconds, providing a uniform layer of 32 nm with a 3 nm roughness as measured by a profilometer. Both samples after testing did not have any change in thickness or appearance at the centre. The outer edge had an increased roughness with the 100°C sample having an approximate 5 mm degraded edge with a roughness of 8 nm and the 140°C sample having a larger degraded edge with a roughness of 10 nm. The effect of the degradation can be seen in the decrease in transmission of light due to increase in surface roughness as seen in fig. A.1.
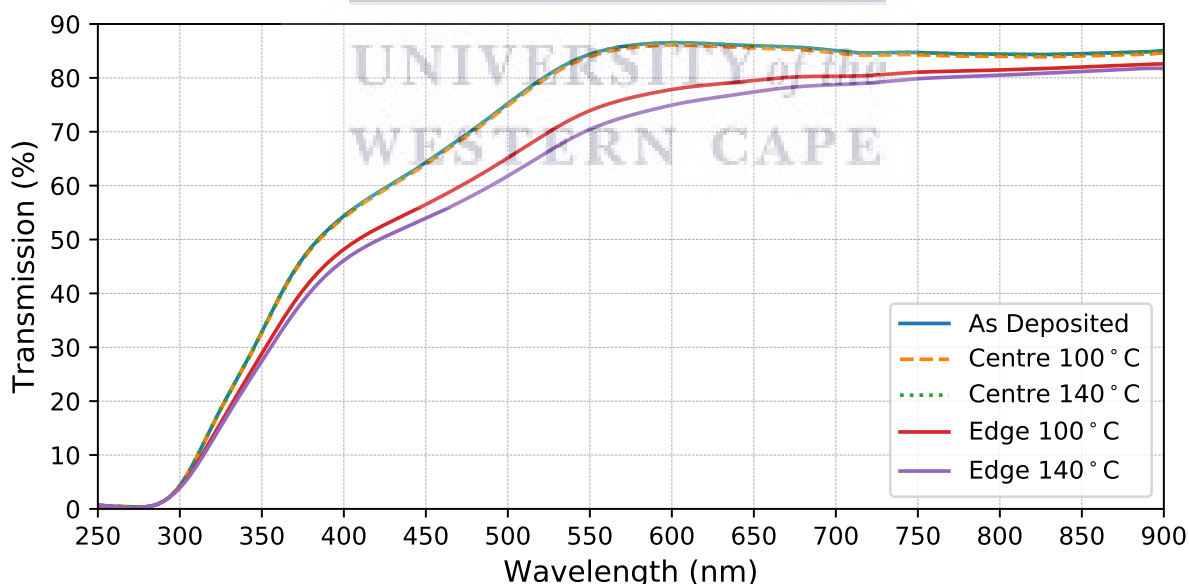
Figure A.1: UV-Vis of Stability Tested PCBM

Appendix B

XRD Analysis

Listed below is the identified peaks of each analysed compound. Due to preferred orientations certain diffraction peaks with intensities below the detection limit were excluded.

B.1   PbI$_2$

Table B.1: XRD PbI2 Rietveld

h	k	l	d	2θ	I(%)	FWHM
0	0	1	6.971	12.71	100	0.09023
0	0	2	3.486	25.56	5.977	0.08598
0	0	3	2.324	38.74	46.74	0.09993
0	0	4	1.743	52.48	47.53	0.1167

Scherrer crystal size 86 ± 8 nm

Rietveld crystal size 165 nm

Lattice constant c = 6.971 Å

Sample displacement -38 μm

B.2   PbCl₂

Table B.2: XRD PbCl₂

h	k	l	d	2θ	I(%)	FWHM
2	0	0	4.518	19.66	8.185	0.128
1	0	1	4.049	21.96	25.05	0.129
2	1	0	3.885	22.89	37.39	0.129
0	2	0	3.805	23.38	40.31	0.129
1	1	1	3.574	24.91	100	0.129
2	1	1	2.949	30.31	2.695	0.130
0	2	1	2.913	30.68	9.108	0.130
2	2	0	2.911	30.71	6.554	0.130
1	2	1	2.773	32.28	52.46	0.131
3	0	1	2.508	35.8	25.84	0.132
0	0	2	2.264	39.8	23.82	0.133
4	0	0	2.259	39.9	5.636	0.133
2	3	0	2.212	40.78	15.84	0.133
1	3	1	2.15	42.01	23.7	0.134
3	2	1	2.094	43.19	23.92	0.134
2	1	2	1.956	46.4	17.82	0.135
4	1	1	1.954	46.46	0.102	0.135
0	2	2	1.946	46.66	9.849	0.135
4	2	0	1.942	46.74	4.206	0.135
0	4	0	1.903	47.78	8.392	0.136
5	1	1	1.639	56.08	8.291	0.140
2	4	1	1.635	56.22	0.591	0.140
5	2	0	1.632	56.33	0.211	0.140
4	0	2	1.599	57.61	5.285	0.141
2	3	2	1.582	58.28	17.68	0.141
4	1	2	1.565	58.99	3.959	0.142
1	1	3	1.461	63.64	6.453	0.144
0	4	2	1.457	63.86	6.821	0.145
1	5	1	1.425	65.47	12.35	0.146
6	2	0	1.4	66.76	3.498	0.147
5	3	1	1.4	66.79	8.89	0.147

Scherrer crystal size 63.9 ± 0.6 nm

Rietveld crystal size 85 nm

Lattice constants a = 9.036, b = 7.611, c = 4.529 Å

Density 5.93 g/cm³

Sample displacement -38 μm

B.3   MAI

Table B.3: XRD MAI (Powder)

h	k	l	d	2θ	I(%)	FWHM
0	0	2	4.512	19.67	100	0.1031
1	0	1	4.457	19.92	16.07	0.1029
1	1	0	3.624	24.55	37.49	0.0994
1	0	2	3.387	26.3	23.87	0.0982
0	0	3	3.008	29.69	76.62	0.0997
1	1	2	2.826	31.65	25.59	0.1006
1	0	3	2.594	34.56	6.321	0.1020
2	0	0	2.563	34.99	4.242	0.1022
1	1	3	2.315	38.89	24.69	0.1043
2	0	2	2.228	40.45	4.142	0.1052
2	1	1	2.222	40.58	23.45	0.1053
1	0	4	2.065	43.82	36.68	0.1072
2	1	2	2.044	44.3	10.86	0.1075
2	0	3	1.951	46.52	14.78	0.1089
2	2	0	1.812	50.32	9.745	0.1114
0	0	5	1.805	50.54	30.16	0.1115
3	1	0	1.621	56.76	5.39	0.1161
1	1	5	1.616	56.96	30.38	0.1163
2	1	4	1.608	57.26	17.18	0.1165
2	2	3	1.552	59.51	7.83	0.1183
0	0	6	1.504	61.63	5.318	0.1201
2	0	5	1.476	62.94	6.46	0.1212
1	0	6	1.443	64.53	12.45	0.1226

Scherrer crystal size 79 $\pm$ 2 nm

Rietveld crystal size 144 nm

Lattice constants a = 5.126, c = 9.024 Å

Density = 2.23 g/cm^3

Sample displacement -23 μm

B.4   MAPbI₃

Table B.4: XRD PSK

h	k	l	d	2θ	I(%)	FWHM
0	0	2	6.30	14.07	62.66	0.0919
1	1	0	6.279	14.12	100	0.0919
2	0	0	4.44	20.01	10.04	0.0870
2	1	1	3.788	23.49	14.2	0.0831
2	0	2	3.629	24.53	17.92	0.0818
0	0	4	3.15	28.33	39.85	0.0831
2	2	0	3.14	28.43	77.88	0.0832
1	1	4	2.815	31.78	12.61	0.0847
3	1	0	2.808	31.86	48.81	0.0847
3	1	2	2.565	34.98	17.31	0.0862
2	2	4	2.224	40.56	41.48	0.0891
4	0	0	2.22	40.63	16.43	0.0892
4	1	1	2.123	42.57	6.49	0.0903
3	1	4	2.096	43.14	13.2	0.0906
4	0	2	2.094	43.19	6.406	0.0906
4	2	0	1.986	45.67	4.503	0.0921
4	1	3	1.916	47.42	6.482	0.0931
4	0	4	1.815	50.26	14.62	0.095
2	2	6	1.745	52.4	4.912	0.0963
5	1	0	1.742	52.52	4.102	0.0964
4	2	4	1.68	54.61	6.794	0.0978
0	0	8	1.575	58.58	3.302	0.1007
4	4	0	1.57	58.79	5.615	0.1009
1	1	8	1.528	60.58	3.547	0.1022
5	1	4	1.524	60.74	5.194	0.1023
5	3	0	1.523	60.79	11.14	0.1024
5	3	2	1.48	62.73	3.485	0.1039
6	0	0	1.48	62.74	1.351	0.104
6	1	1	1.45	64.19	3.066	0.1051

Scherrer crystal size 93 ± 3 nm

Rietveld crystal size 188 nm

Lattice constants a = 8.880, c = 12.599 Å

Density = 4.15 g/cm³

Sample displacement -46 μm

B.5 MAPbI$_{3-x}$Cl$_x$

Table B.5: XRD PSK

h	k	l	d	2θ	I(%)	FWHM
0	0	2	6.282	14.12	59.19	0.112
1	1	0	6.273	14.13	100	0.112
2	0	0	4.436	20.03	26.79	0.11
2	1	1	3.784	23.52	34.38	0.117
2	0	2	3.624	24.57	26.07	0.113
0	0	4	3.141	28.42	37.88	0.115
2	2	0	3.137	28.46	77.48	0.115
1	1	4	2.809	31.86	11.46	0.117
3	1	0	2.806	31.9	8.863	0.117
3	1	2	2.562	35.02	19.31	0.119
2	2	4	2.22	40.64	19.17	0.122
4	0	0	2.218	40.67	47.4	0.122
4	1	1	2.121	42.62	6.335	0.123
3	1	4	2.092	43.23	12.53	0.124
4	0	2	2.091	43.25	32.24	0.124
4	2	0	1.984	45.72	7.563	0.125
4	1	3	1.914	47.49	7.48	0.127
4	0	4	1.812	50.34	21.59	0.129
2	2	6	1.742	52.52	1.635	0.131
5	1	0	1.74	52.58	5.271	0.131
4	2	4	1.677	54.7	12.62	0.132
0	0	8	1.57	58.77	2.986	0.136
4	4	0	1.568	58.85	5.567	0.136
1	1	8	1.523	60.77	0.877	0.138
5	1	4	1.522	60.83	9.25	0.138
5	3	0	1.522	60.85	61.74	0.138
5	3	2	1.479	62.81	3.914	0.140
6	0	0	1.479	62.81	4.009	0.140
6	1	1	1.449	64.26	3.134	0.141

Scherrer crystal size 69 ± 2 nm

Rietveld crystal size 121 nm

Lattice constants a = 8.872, c = 12.564 Å

Density = 4.16 g/cm^3

Sample displacement -52 μm

B.6   SnO$_2$

Table B.6: XRD SnO$_2$

h	k	l	d	2θ	I(%)	FWHM
1	1	0	3.3473	26.61	100	1.252
1	0	1	2.6442	33.87	84.337	1.176
2	0	0	2.3837	37.71	24.096	0.948
1	1	1	2.3334	38.55	19.277	0.937
2	1	1	1.764	51.78	77.108	1.330
2	2	0	1.6775	54.67	23.494	1.166
0	0	2	1.5873	58.06	21.687	0.970
3	1	0	1.4951	62.02	21.687	1.208
1	1	2	1.4414	64.60	24.096	1.511
3	0	1	1.4148	65.97	24.096	1.466

Average crystal size based on the Scherrer eq. 7 ± 1. Tetragonal crystal structure with space group P42/mnm [148] lattice constants of a = 4.739Å , c = 3.186Å , volume 71.56 Å and density of 6.99 g/cm^3.
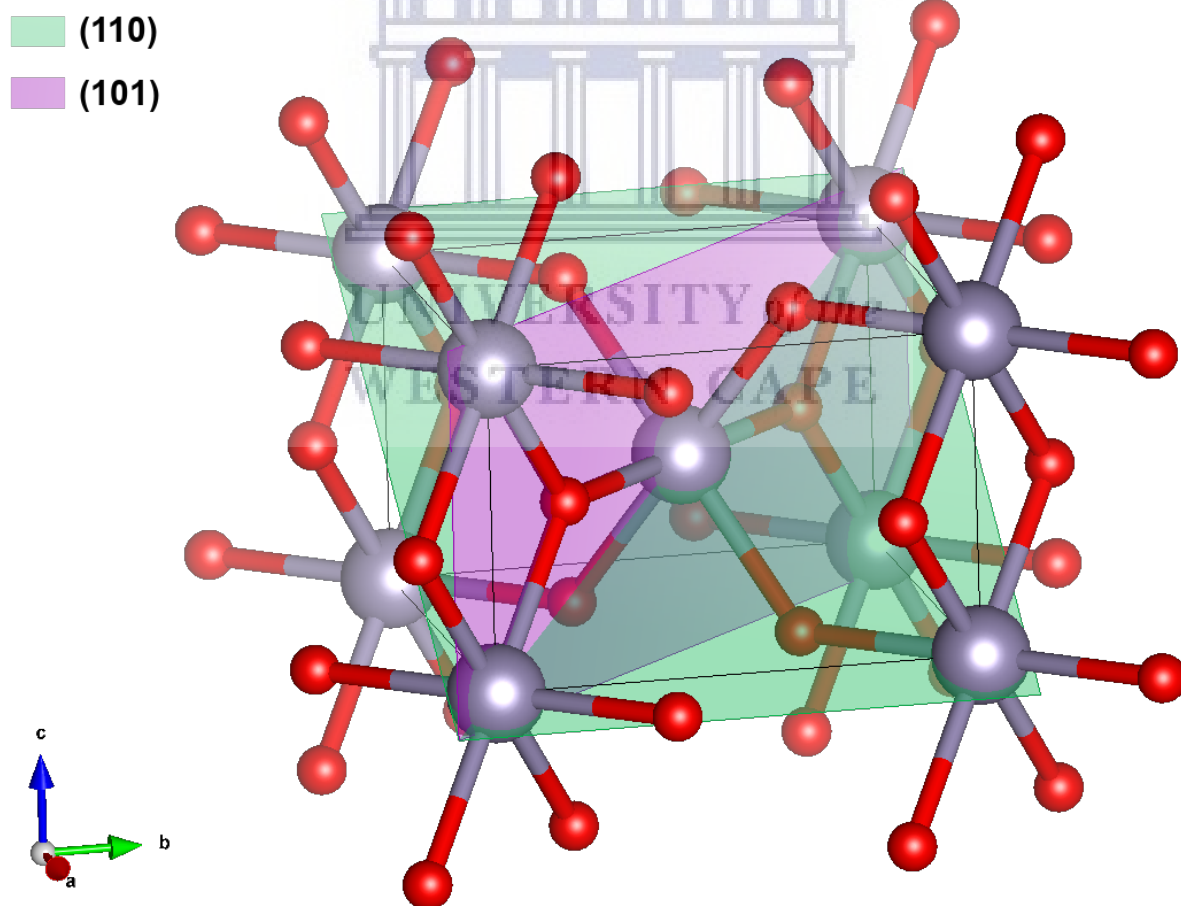
Figure B.1: Unit Cell of SnO$_2$

Appendix C

SEM Analysis
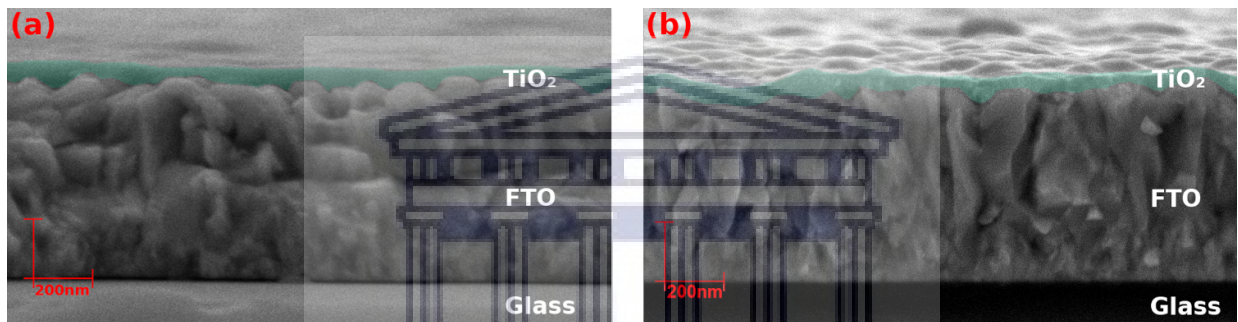
C.1 TiO$_2$ Thickness

Figure C.1: Cross-section SEM of TiO$_2$ on FTO

The thickness of two samples of TiO$_2$ spin-coated onto FTO. Sample (a) had a FTO thickness of 677 ± 16 nm and TiO$_2$ thickness of 53 ± 16 nm with a surface roughness of 9.2 nm. Sample (b) had a FTO thickness of 658 ± 23 nm and TiO$_2$ thickness of 58 ± 21 nm with a surface roughness of 17.8 nm.

Appendix D

Source Code

D.1   Grain Size

```python
import numpy as np, matplotlib.pyplot as plt, os
from PIL import Image
import scipy.spatial.distance as d
import scipy.optimize as opt

dir = '/home/stephen/Desktop/Exp/Stephen Klue/15 July 2020/low_temp'
file = '0.18#perovskite_04.png'
file = os.path.join(dir,file)
img = Image.open(file)
data = np.asarray(img)
if len(data[0][0]) == 4:
    data = np.delete(data,3,axis=2)

# scale [pixels per nanometer] (value in file name)
scale = float(file.split('/')[-1].split('#')[0])


def get_points(data,colour):
    d1 = np.where(np.all(data == colour, axis=-1))
    return np.asarray([d1[1],d1[0]]).T/scale


grains = get_points(data,(0,0,255))
gaps = get_points(data,(0,255,0))
boundaries = get_points(data,(255,0,0))

grain_dist = np.zeros((len(grains),len(boundaries),1))
grain_angle = np.zeros((len(grains),len(boundaries)))

gap_dist = np.zeros((len(gaps),len(boundaries),1))
gap_angle = np.zeros((len(gaps),len(boundaries)))

v = grains[0:1] - boundaries
theta = np.arctan(v[:,1]/v[:,0])
for i in range(len(grains)):
    grain_dist[i] = d.cdist(boundaries, grains[i:i+1])
    v = boundaries- grains[i:i+1]
    grain_angle[i] = np.arctan2(v[:,1],v[:,0])
```

```python
39         neg = np.where(grain_angle[i]<0)
40         grain_angle[i][neg] += 2*np.pi
41
42 v2 = gaps[0:1] - boundaries
43 theta = np.arctan(v[:,1]/v[:,0])
44
45 for i in range(len(gaps)):
46     gap_dist[i] = d.cdist(boundaries, gaps[i:i+1])
47     v = boundaries - gaps[i:i+1]
48     gap_angle[i] = np.arctan2(v[:,1],v[:,0])
49     neg = np.where(gap_angle[i]<0)
50     gap_angle[i][neg] += 2*np.pi
51
52
53 def get_grains(n,grain_dist,grain_angle):
54     dt = 2*np.pi/n
55     thetas = np.arange(0, 2*np.pi, dt)
56     grains = []
57
58     for i in range(len(grain_dist)):
59         grain = []
60         # print(grain_angle[i],len(grain_angle[i]))
61         for t in thetas:
62             ind = np.where(np.logical_and(grain_angle[i] >= t,
                                          grain_angle[i]<= t+dt))[
                                          0]
63             if len(ind) > 0:
64                 dist = grain_dist[i][ind]
65                 mn = np.amin(dist)
66                 mn_i = np.where(dist==mn)[0][0]
67                 grain.append(boundaries[ind[mn_i]])
68         grains.append(np.asarray(grain))
69
70     return np.asarray(grains)
71
72
73 gaps2 = get_grains(15,gap_dist,gap_angle)
74 grains2 = get_grains(40,grain_dist,grain_angle)
75
76
77 def plot_grains_gaps():
78     plt.scatter(boundaries[:,0],boundaries[:,1],c='r')
79     plt.scatter(grains[:,0],grains[:,1],c='b')
80     plt.scatter(gaps[:,0],gaps[:,1],c='g')
81     ax = plt.gca()
82     ax.invert_yaxis()
83
84     def plotg(g,g2):
85         for j in range(len(g2)):
86             plt.scatter(g2[j][:, 0], g2[j][:, 1])
87             plt.annotate(str(j + 1), g[j])
88
89     plotg(grains,grains2)
90     plotg(gaps,gaps2)
91
92     plt.legend()
93     plt.show()
94
```

```
95
96  plot_grains_gaps()
97
98  #Shoelace Formula
99  def poly_area(x,y):
100     return 0.5 * (np.dot(x[:-1], y[1:]) + x[-1]*y[0] - np.dot(y[:-1], x[1
                                                :]) - y[-1]*x[0])
101
102
103 def get_size(grains2):
104     size = np.zeros(len(grains2))
105     area = np.zeros(len(grains2))
106
107     for i in range(len(grains2)):
108         a = poly_area(grains2[i][:,0],grains2[i][:,1])
109         area[i] = a
110         D = np.sqrt(a/np.pi)*2
111         size[i] = D
112         print(i+1,'{:.3g}'.format(D))
113     print('Mean = {:.1f} +- {:.2g} nm'.format(np.average(size),np.std(
                                                size,ddof=1)))
114     return size,np.sum(area)
115
116
117 print('---Grains---')
118 size_grains,a1 = get_size(grains2)
119 print('---Voids---')
120 size_gaps, a2 = get_size(gaps2)
121 all = np.append(size_gaps,size_grains)
122 print('Voids {:.3f}%'.format(100*a2/(a2+a1)))
123
124
125 def gauss(x,mu,sig,i):
126     return i*np.exp(-(x-mu)**2/(2*sig**2))
127
128
129 def res(p,x,y):
130     return y - gauss(x,*p)
131
132
133 def fit(x,y,mu0,sig0,i0):
134     x0 = [mu0, sig0, i0]
135     b_min = [mu0*0.5,sig0*0.4,i0*0.7]
136     b_max = [mu0*1.5,sig0*1.6,i0*1.3]
137
138     ans = opt.least_squares(res, x0, bounds=(b_min, b_max), args=(x, y),
139                         xtol=1e-15, ftol=1e-15, gtol=1e-15, jac='3-
                                                point',
                                                verbose=
                                                2)
140     var = ans.x
141     return var
142
143
144 def gauss_plot(grains, bins=10,region=(0,1000)):
145     hist = np.histogram(grains, bins=bins)
146     plt.hist(grains, hist[1], rwidth=0.98)
147     # print(hist,hist[0]/len(grains))
```
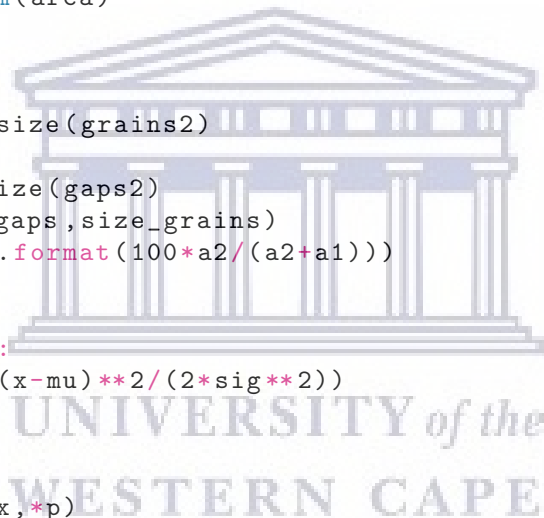
```
148    x = (hist[1][1:]+hist[1][:-1])/2
149    var = fit(x,hist[0],np.mean(grains),np.std(grains,ddof=1),np.max(hist
                                                         [0]))
150    print('---Gaussian---')
151    print('Mean = {:.1f} +- {:.2g} nm'.format(var[0], var[1]))
152    x2 = np.linspace(region[0],region[1],1000)
153    plt.plot(x2,gauss(x2,var[0],var[1],var[2]),c='r',lw=3)
154    plt.vlines(var[0],0,gauss(var[0],var[0],var[1],var[2]),linewidth=2,
                                                         color='k')
155    plt.vlines(var[0]+var[1],0,gauss(var[0]+var[1],var[0],var[1],var[2]),
                                           linestyle='--',linewidth=2,color
                                           ='k')
156    plt.vlines(var[0]-var[1],0,gauss(var[0]-var[1],var[0],var[1],var[2]),
                                           linestyle='--',linewidth=2,color
                                           ='k')
157    plt.xlabel('Grain Size ($\mu$m)',fontsize=24,c='r')
158    plt.ylabel('Number of Grains',fontsize=12)
159    plt.xlim(region[0],region[1])
160    ax = plt.gca()
161    fig = plt.gcf()
162    fig.set_size_inches(7, 5)
163    plt.tight_layout()
164    plt.show()
165
166 gauss_plot(size_grains)
```

D.2   Voltage Sweep

```
1  import visa
2  import numpy as np
3  import time
4
5
6  def volt_sweep(start,stop,points,compliance,nplc,delay,wire4):
7      """
8          Sends VISA commands to an SMU to sweep voltage
9          over a range of desired data points
10
11         Parameters
12         ----------
13         start : number
14             Start of interval.
15         stop : number
16             End of interval.  The interval does include this value
17         points : integer
18             Number of data points in the voltage sweep
19         compliance: number
20             The maximum current that the SMU will allow
21         nplc: number
22             Number of power lines per cycle, value between 0.01 and 10
23         delay: number
24             The time in milliseconds that the voltage dwells
25             before a measurement is performed.
26         wire4: 'on' or 'off'
27             Set the SMU to perform a 4 wire voltage sweep
28
```

```python
29          Returns
30          -------
31          [voltage numpy array], [current numpy array], True/False
32
33          voltage : numpy array
34              Array of voltages with length of points
35              if measurement is not made a array of zeros is returned
36              (unit in volts)
37          current :  numpy array
38              Array of current with length of points
39              if measurement is not made a array of zeros is returned
40              (unit in amps)
41          successful : boolean
42              indicates whether a succesfull measurement had been performed
43      """
44      rm = visa.ResourceManager()
45      print('resources', rm.list_resources())
46      cont = False
47      if 'GPIB0::24::INSTR' in rm.list_resources():
48          cont = True
49          k = rm.open_resource('GPIB0::24::INSTR')
50          k.timeout = 100000
51
52          s = time.time()
53          k.write('*RST')
54          k.write(':outp:smod norm')
55          k.write('syst:azer:stat off')
56          k.write(':sour:func volt')
57          k.write('sour:volt:rang:auto on')
58          k.write(':form:elem volt,curr')
59          k.write(':sens:func:conc on')
60          k.write(':sens:func:on "volt"')
61          k.write(':syst:rsen {}'.format(wire4)) #4-wire
62          k.write(':sens:curr:prot {}'.format(compliance))
63          k.write(':sens:curr:nplc {}'.format(nplc))
64          k.write(':sens:curr:rang:auto on')
65          k.write(':sens:aver:coun 1.000')
66          k.write(':sens:aver:stat off')
67          k.write(':outp:stat on')
68          k.write(':syst:time:res')
69          k.write(':outp:stat on')
70          k.write('OUTP ON')
71          k.write('INIT')
72
73          v_list = np.linspace(start, stop, points)
74          v = np.zeros(points)
75          c = np.zeros(points)
76
77          for j,i in enumerate(v_list):
78              k.write(':sour:volt:lev {}'.format(i))
79      time.sleep(delay/1000)
80              values = (k.query_ascii_values(':read?'))
81              v[j] = values[0]
82              c[j] = values[1]
83
84
85          k.write(':OUTP OFF') # disconnect communication with SMU
86          c = np.array(c)
```

```
87          v = np.array(v)
88          print('Complete in {:.2f} sec.'.format(time.time() - s))
89          return v,c,cont
90      else:
91          return np.zeros(points),np.zeros(points),False
```